

Calibration and Characterization of a 7-pixel TRISTAN Detector with an LED

Master's Thesis

Markus Kandler

03695629

Course of studies:

Nuclear, Particle, and Astrophysics

at

Technical University of Munich

First Reviewer: Prof. Dr. Susanne Mertens

Second Reviewer: Dr. Raimund Strauß

Supervisor: Dr. Frank Edzards

M.Sc. Korbinian Urban

M.Sc. Christian Forstner

02.05.2024

Contents

1	Introduction	1
2	Neutrino Physics	3
2.1	Neutrino Discovery	3
2.2	Neutrino Mixing and Oscillations	5
2.3	Neutrino Mass	6
2.4	Sterile Neutrinos	9
3	The KATRIN Experiment	11
3.1	Experimental Setup	11
3.2	Sterile Neutrino Search with the KATRIN Experiment	15
4	The TRISTAN Detector System	19
4.1	Introduction to Semiconductor Materials	19
4.2	Semiconductor Detectors	21
4.3	Silicon Drift Detectors	22
4.4	Readout Electronics	28
5	Detector Calibration with an LED	33
5.1	Experimental Setup	33
5.2	Measurement Overview	36
5.3	LED Selection	39
5.4	Observed Energy Spectrum	41
5.5	Energy Calibration with ^{55}Fe	43
5.6	Count Rate Analysis	45
5.7	Energy Resolution	47
5.8	Comparison to Poissonian Nature	50
5.9	Noise Analysis	52
5.10	Rise Time Analysis	55
5.11	Energy Stability	57
5.12	Conclusions	59
6	Detector Operating Parameter Optimization	60
6.1	Experimental Setup	60
6.2	Optimization of the Beam Spot Width	62
6.3	Measurement Overview	65
6.4	Detector Characteristics	67
6.5	Analysis Procedure	69
6.6	Results of the IGR Scans	71

7	Conclusions	76
A	Appendix	78
	List of Figures	82
	List of Tables	84
	Acronyms	85
	References	87

1. Introduction

Sterile neutrinos are a natural extension of the [Standard Model \(SM\)](#) of particle physics. With a mass on the keV-scale, they are a suitable dark matter candidate and could potentially explain one of the most intriguing open questions in physics. The sterile mass eigenstate mixes with one of the active neutrinos and is the key to searching for sterile neutrinos.

The current goal of the Karlsruhe Tritium Neutrino (KATRIN) experiment is the determination of the effective electron antineutrino mass by measuring tritium β -decay. After the neutrino mass measurement has been completed at the end of 2025, the KATRIN beamline will be upgraded to enable a search for sterile neutrinos in the keV mass range. To this end, a novel detector and readout system is currently being developed in the scope of the TRISTAN project [1]. In the currently ongoing neutrino mass measurements, only the region around the endpoint of the energy spectrum is probed. For the keV-scale neutrino search, however, the measurement range needs to be extended to the entire energy range of the decay. The imprint of a sterile neutrino in the energy spectrum is a spectral distortion, including a kink-like signature. To cope with the high electron rates of 10^8 cps, that the current detector system cannot handle, the TRISTAN detector is being developed. It is based on the [Silicon Drift Detector \(SDD\)](#) technology with an integrated [n-channel Junction Field Effect Transistor \(nJFET\)](#) to distribute the high rate across many and reduce noise. This allows a targeted energy resolution of 300 eV at 20 keV for count rates of up to 100 keps.

To enable a precise keV-sterile neutrino search, an accurate energy calibration of the detector system is imperative. Typically, radioactive sources such as ^{55}Fe or ^{241}Am are used to calibrate [SDDs](#). However, implementing these sources in certain experimental environments can be challenging. A promising alternative approach is the calibration of the detector system with a [Light-Emitting Diode \(LED\)](#). In the scope of this thesis, the feasibility of calibrating the energy scale using an [LED](#) has been investigated. In comparison to the conventional energy calibration with radioactive sources, this method has the advantage that it can be easily integrated into the experimental setup and turned on or off at any time. To characterize the calibration method, a 7-pixel prototype TRISTAN detector was illuminated with different [LEDs](#). [LEDs](#) with different properties (pulse width, light intensity, and stability) have been studied, and a suitable candidate has been selected for further studies. Subsequently, fundamental detector properties such as the energy resolution, rise time, and electronic noise were examined. Finally, it was investigated how the calibration process can be realized and compared to the theoretical prediction.

The second main goal of this thesis was the optimization of one of the operating parameters of the detector. More specifically, dedicated measurements were carried out to optimize one of the detector bias voltages, the so-called **Inner Guard Ring (IGR)** voltage. The **IGR** is a small electrode in the region of the pixel center, which separates the collecting anode from the integrated **nJFET**. It sits at a negative potential and prevents the electrons from drifting to the **nJFET**, which would result in a charge loss. The main focus of this work was to optimize the **IGR** voltage by investigating the charge collection properties of a 7-pixel detector in the region of the pixel center. To this end, an experimental setup was designed to systematically scan the detector with a focused **LED** beam.

This thesis is structured as follows: In chapter 2, a brief introduction to neutrino physics is given. Subsequently, chapter 3 explains the KATRIN experiment and introduces the TRISTAN project. Chapter 4 gives an overview of semiconductors and then discusses the operating principle of an **SDD**. Moreover, the details of the TRISTAN detector and the readout electronics will be discussed. The investigations in which an **LED** is used to calibrate the energy scale are detailed in chapter 5. Chapter 6 focuses on optimizing the **IGR** voltage.

2. Neutrino Physics

The [Standard Model \(SM\)](#) of particle physics is currently the leading model in particle physics. It contains quarks and leptons, distinguishing between integer and half-integer spin particles [2]. Bosons serve as exchange particles for all four fundamental interaction forces, while fermions constitute the particles that make up all matter. Quarks interact through the strong force, playing a crucial role in forming the nuclei of atoms. Leptons, a subcategory of fermions, are further divided into two main types: The first are charged leptons, like electrons, which are electrically charged and participate, for example, in electromagnetic interactions. The second are neutral leptons, like neutrinos, which are neutral and interact via the weak interaction. Both charged fermions and neutrinos come in three distinct flavors: electron e , muon μ , and tau τ . While every fermion has a right- and left-handed counterpart, neutrinos take a unique role in the [SM](#) because only left-handed and right-handed antineutrinos are observed. In the [SM](#), neutrinos are assumed to be massless, but neutrino oscillation experiments show that they have a small, yet non-zero mass [3, 4].

To better understand the properties of neutrinos and their role in the [SM](#), their discovery is discussed in section 2.1. The observations of oscillation experiments and the resulting formalism of neutrino flavor oscillations are described in section 2.2. Section 2.3 provides an overview of currently ongoing neutrino mass determination efforts. Finally, section 2.4 introduces sterile neutrinos.

2.1. Neutrino Discovery

The origin of the initial postulation of the neutrino traces back to the following β^- -decay. To conserve the energy in this decay, another particle was postulated so that the 2-body decay becomes a 3-body decay. n is a neutron, p a proton, e^- an electron, and $\bar{\nu}_e$ an electron antineutrino:

$$n \rightarrow p + e^- + \bar{\nu}_e. \tag{1}$$

In 1930, W. Pauli postulated in an open letter to the "Radioactive Group" the existence of an electrically neutral particle emitted alongside the electron during β -decay [5]. He justified by stating that the observed continuous electron energy spectrum can be explained by the fact that the remaining energy is given to the neutrino, transforming the decay process into a 3-body decay. This particle possesses a spin of 1/2 and adheres to the Pauli exclusion principle.

Twenty-three years later, the neutrino was experimentally detected by C. Cowan [6].

The experimental setup includes cadmium in a liquid scintillator. He uses the high antineutrino flux of a fission reactor to capture them via the inverse β -decay:

$$\bar{\nu}_e + p \rightarrow e^+ + n, \quad (2)$$

where e^+ is the positron, the antiparticle of the electron. The antineutrino $\bar{\nu}_e$ interaction creates two distinguished signals in the detector. First, the positron e^+ annihilates with an electron, creating fluorescence light. Then, after thermalization, the neutron n is captured on a cadmium atom, emitting a second scintillation signal. Due to a signal with a fixed time constant of 200 ms, the unique pulse pair signal confirms the detection of the electron antineutrino $\bar{\nu}_e$.

In 1962, L. Lederman, M. Schwartz, and J. Steinberger discovered the second neutrino, the muon antineutrino $\bar{\nu}_\mu$. In their experiment, a 15 GeV proton beam hits a beryllium target, producing pions which decay into muons μ^- and muon-neutrinos ν_μ [7]. A thick steel shielding ensures that only neutrinos enter a spark chamber, separated into many parts through aluminum plates. Then, the following inverse β -decay takes place:

$$\bar{\nu}_\mu + p \rightarrow \mu^+ + n. \quad (3)$$

Two decay channels are possible: the electron antineutrino $\bar{\nu}_e$ generates an electron e^- , and the muon antineutrino $\bar{\nu}_\mu$ generates a muon μ . The muon leaves a trace as it passes through many aluminum plates. In contrast, electrons are stopped on the first aluminum plate. The difference in the detected signals indicates the presence of a second neutrino flavor.

The discovery of the tauon in 1995 [8] raised the question of the existence of a tau neutrino, which was experimentally confirmed in 2001 by the Direct Observation of Nu Tau (DONUT) experiment at Fermilab [9]. The particles generated in the accelerator can be selectively filtered using magnetic fields and shielding techniques, leaving only the tau neutrino. The tau neutrino beam interacts with the target material, producing a tauon. The tau decays within a distance of 2 mm, leaving charged particles that leave a track in the detector, resulting in the famous kink signal.

As a result, all three neutrino flavors, corresponding to the lepton flavors e , μ , and τ , were discovered. Furthermore, contrary to all other fermions, neutrinos have only left-handed chirality, while antineutrinos are only right-handed, confirmed through the Goldhaber experiment [10]. Hence, they are also massless. With the tau neutrino, the last lepton particle was found and completed the leptons in the SM (see fig. 2.1).

**Three generations
of matter (fermions) spin 1/2**

	I	II	III
Mass →	2.4 MeV	1.27 GeV	171.2 GeV
Charge →	2/3	2/3	2/3
Name →	Left <i>u</i> Right Up	Left <i>c</i> Right Charm	Left <i>t</i> Right Top
Quarks	4.8 MeV -1/3 Left <i>d</i> Right Down	104 MeV -1/3 Left <i>s</i> Right Strange	4.2 GeV -1/3 Left <i>b</i> Right Bottom
	0 eV 0 ν_e Left Electron neutrino Right	0 eV 0 ν_μ Left Muon neutrino Right	0 eV 0 ν_τ Left Tau neutrino Right
	0.511 MeV -1 Left <i>e</i> Right Electron	105.7 MeV -1 Left μ Right Muon	1.777 GeV -1 Left τ Right Tau
Leptons			

Figure 2.1: Fermions of the SM. The quarks are shown in violet, whereas the leptons are colored in green. [11]

2.2. Neutrino Mixing and Oscillations

In the 1960s, the so-called ‘Solar Neutrino Problem’ posed entirely new questions in neutrino physics [12]. In the Homestake experiment by Raymond Davis Jr., the neutrino flux generated by solar fusion was measured based on the following inverse β -decay:

$$\nu_e + {}^{37}\text{Cl} \rightarrow {}^{37}\text{Ar} + e^-. \quad (4)$$

Interestingly, the measured solar neutrino flux, mainly electron anti-neutrinos, was less than the predicted flux by a factor of 3. About 30 years later, the Sudbury Neutrino Observatory (SNO) measures all three neutrino flavors [3]. The combination of charge current interactions, sensitive for electron neutrinos, and neutral current interactions, sensitive for the other flavors, enables the measurement of all three neutrinos. The total rate agrees with the theoretical prediction by measuring all three neutrino flavors. The observations could be independently confirmed by the Super-Kamiokande experiment [4]. This introduces the phenomenon of neutrino flavor oscillations.

Neutrino oscillations describe the property where neutrinos of one flavor trans-

form into a different kind at a certain distance. The three flavor eigenstates (ν_e, ν_μ, ν_τ) are, in fact, superpositions of the three mass eigenstates (ν_1, ν_2, ν_3) [13]. This mixing can be described by the [Pontecorvo-Maki-Nakagawa-Sakata \(PMNS\)](#) matrix U_{PMNS} as follows:

$$\underbrace{\begin{pmatrix} \nu_e \\ \nu_\mu \\ \nu_\tau \end{pmatrix}}_{\text{Flavor eigenstates}} = \underbrace{\begin{pmatrix} U_{e1} & U_{e2} & U_{e3} \\ U_{\mu1} & U_{\mu2} & U_{\mu3} \\ U_{\tau1} & U_{\tau2} & U_{\tau3} \end{pmatrix}}_{\text{PMNS matrix}} \underbrace{\begin{pmatrix} \nu_1 \\ \nu_2 \\ \nu_3 \end{pmatrix}}_{\text{Mass eigenstates}} \quad (5)$$

The PMNS matrix can be reduced into three mixing angles ($\theta_{12}, \theta_{13}, \theta_{23}$), describing the mixing amplitudes U , and in the complex Dirac phase δ , which can cause CP-violation. Assuming only two flavor eigenstates α and β for simplification, the probability for a flavor change for a neutrino with an energy E and after a traveled distance L is given by:

$$P_{\alpha \rightarrow \beta} = \sin^2(2\Theta) \cdot \sin^2\left(\frac{\Delta m^2}{4} \cdot \frac{L}{E}\right), \quad (6)$$

where Θ is the mixing angle and Δm^2 the mass squared difference. For neutrino oscillations to be possible, the mass difference Δm has to be non-zero. In the case of 3 neutrino flavors, at least two neutrinos must be massive to describe the observations of Neutrino oscillations. Many other experiments confirmed neutrino oscillation [14, 15, 16]. Since oscillation experiments are only sensitive to the mass difference Δm^2 , they do not provide any information about the absolute mass of neutrinos [14]. This matter will be more detailed in the following section 2.3.

2.3. Neutrino Mass

Neutrinos are the only fermions in the [SM](#) whose absolute masses are unknown. From the experimental point of view, the neutrino mass determination is very challenging since their masses are at least five orders of magnitude smaller than the mass of the electron, see fig. 2.2.

Currently, three different methods are pursued to determine the mass of the neutrino: 1) cosmological observations, 2) neutrinoless double beta decay, and 3) direct neutrino mass measurements using the kinematics of single β -decay. In the following, each method will be discussed briefly.

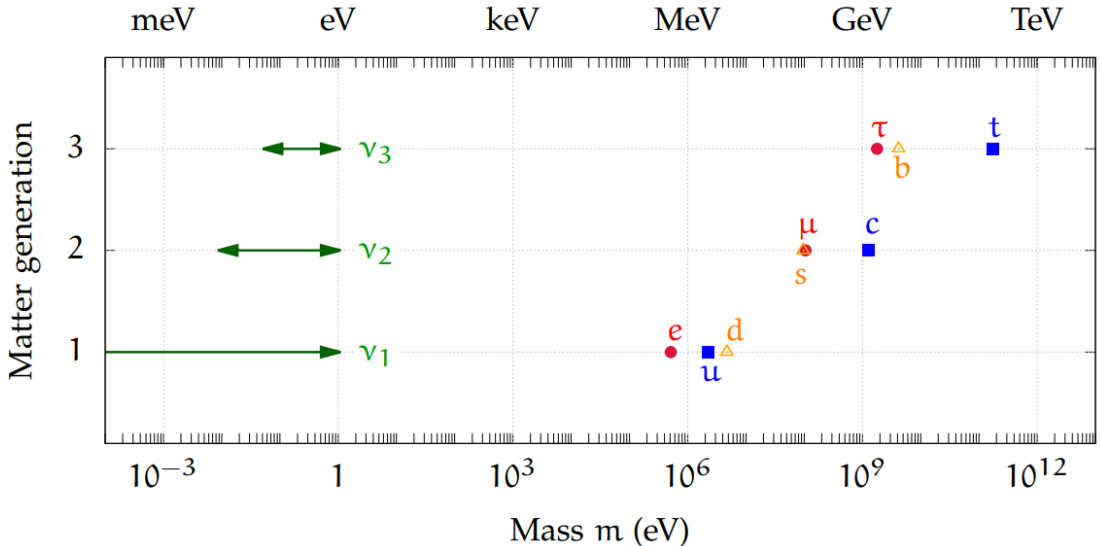


Figure 2.2: Masses of all fermions. The normal mass ordering of neutrinos ($m_1 \ll m_2 < m_3$) is assumed [17].

Cosmology

The most abundant massive particles in our universe are neutrinos with about 336 per cm^3 [18]. Even though they are very light, they can significantly impact the formation of structures, for example, by washing out small-scale structures. By observing the universe's structure via the cosmic microwave background, galaxy surveys, and the Lyman- α forest, limits on the sum m_ν of the neutrino masses can be derived. The latest constraint, as reported by the Planck collaboration, is [19]:

$$m_\nu = \sum_i m_i < 0.12 \text{ eV (95 \% C.L.)}. \quad (7)$$

Due to the high model dependency, this limit is very sensitive to the assumptions used [19].

Neutrinoless double β -decay

In some isotopes, such as ^{48}Ca , ^{76}Ge , and ^{82}Se , single β -decay is energetically forbidden or highly suppressed. Instead, these isotopes exclusively undergo two-neutrino double β -decay ($2\nu\beta\beta$) [20]. In this process, two neutrons simultaneously decay into two protons, two electrons, two neutrinos, and two antineutrinos. It is important to distinguish between ordinary double β -decay ($2\nu\beta\beta$), in which two neutrinos are emitted, and neutrinoless double β -decay ($0\nu\beta\beta$) which would violate lepton number conservation. The latter process has never been observed. This process is only possible if neutrinos are Majorana particles, i.e. their own antiparticles. The mass is observable in ($0\nu\beta\beta$), the so-called effective Majorana mass. It is a coherent sum of the neutrino mass eigenstates weighted by the neutrino mixing matrix elements U_{ei}^2 . In experiments the half-life $T_{1/2}^{0\nu}$ is measured and is related as

in the following:

$$\langle m_{\beta\beta} \rangle = \left| \sum_i U_{ei}^2 m_i \right|. \quad (8)$$

The experimental signature of the hypothetical $0\nu\beta\beta$ decay is a mono-energetic peak at the endpoint of the corresponding $2\nu\beta\beta$ decay, corresponding to the decay's Q-value. The KamLAND-Zen experiment currently holds the most stringent limit on the decay half-life with a value of $T_{1/2}^{0\nu} > 2.3 \cdot 10^{26}$ y. This can be translated into an effective Majorana mass of $\langle m_{\beta\beta} \rangle < 36 - 156$ meV [21].

Kinematics of single β -decay

The most model-independent way of probing the neutrino mass is via the kinematics of single β -decay, see eq. (1). The imprint of the neutrino mass is most pronounced at the endpoint E_0 of the decay spectrum, see fig. 2.3. Since the electron and antineutrino share the total released energy, the maximum energy of the electron is $E_0 - m_\beta$. The KATRIN experiment measures the neutrino mass using tritium β -decay. The experiment uses an ultra-luminous tritium source (10^{11} Bq) with a half-life of $T_{1/2} = 12.3$ y and an endpoint energy of $E_0 = 18.6$ keV. The effective electron antineutrino mass is the incoherent sum of the neutrino mass eigenstates:

$$m_\beta^2 = \sum_i |U_{ei}|^2 m_i^2. \quad (9)$$

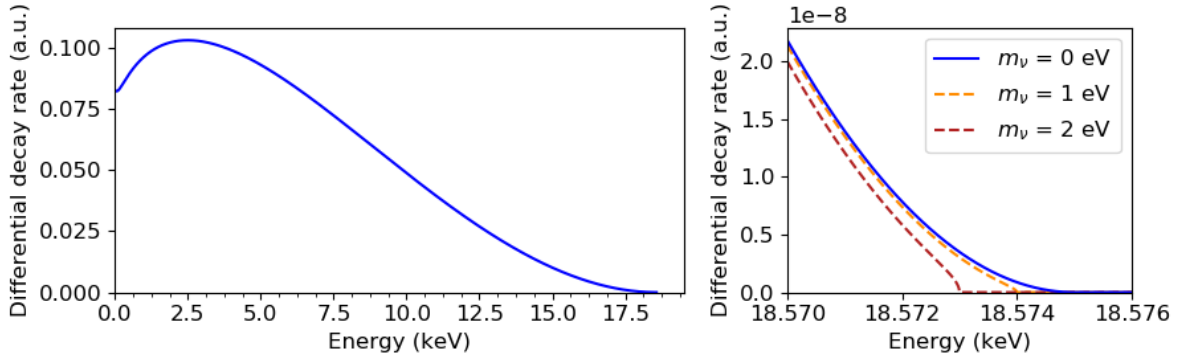


Figure 2.3: The tritium β -decay spectrum is shown on the left. The figure on the right-hand side shows a closeup of the endpoint region. The imprint of the neutrino mass is a spectral distortion. Figure taken from [22].

Recently, the KATRIN collaboration published the world-leading limit on direct neutrino mass measurements with a value of $m_\beta < 0.8$ eV (90% C.L.) [23, 24, 25]. A detailed description of the KATRIN experiment is given in section 3.

2.4. Sterile Neutrinos

Neutrinos are the only particles in the [SM](#) that solely appear with left-handed chirality. One option for a minimal extension to the [SM](#) is the introduction of right-handed neutrinos. In the following, referred to as sterile neutrinos, they are defined with a new mass eigenstate ν_4 that is right-handed. Since the weak interaction only couples to left-handed neutrinos, right-handed neutrinos can only be measured through their mixing with the active neutrinos. In the case of one additional sterile neutrino, the [PMNS](#) matrix is extended as follows:

$$\begin{pmatrix} \nu_e \\ \nu_\mu \\ \nu_\tau \\ \nu_s \end{pmatrix} = \begin{pmatrix} U_{e1} & U_{e2} & U_{e3} & U_{e4} \\ U_{\mu1} & U_{\mu2} & U_{\mu3} & U_{\mu4} \\ U_{\tau1} & U_{\tau2} & U_{\tau3} & U_{\tau4} \\ U_{s1} & U_s & U_{s3} & U_{s4} \end{pmatrix} \begin{pmatrix} \nu_1 \\ \nu_2 \\ \nu_3 \\ \nu_4 \end{pmatrix}, \quad (10)$$

where U_{ij} quantifies the mixing of each flavor. The mass of the sterile neutrino can be arbitrarily large, i.e. it can range from the eV up to the GeV scale. The different mass scales of a sterile neutrino could help to resolve unanswered questions in neutrino physics and cosmology. The following sections will discuss three sterile neutrino mass scales in more detail.

GeV mass scale

The neutrino mass is very small compared to all other fermions, see [fig. 2.2](#). The so-called seesaw mechanism is one way to explain the lightness of the active neutrinos [\[26\]](#). In this mechanism, which assumes neutrinos to be Majorana particles, a Dirac mass term m_D and the Majorana neutrino mass term m_R results from the [PMNS](#) matrix:

$$m_1 \approx m_R \quad \text{and} \quad m_2 = \frac{m_D^2}{m_R}, \quad (11)$$

with m_1 and m_2 being the physical neutrino masses. This leads to a very small neutrino mass due to the high m_R .

Sterile neutrinos on the GeV mass scale present a compelling solution to another open question in physics, i.e. the baryon asymmetry in the early universe, potentially through a mechanism known as leptogenesis [\[27\]](#). However, a requirement for consistency with the observed abundances of light elements in our universe is that these sterile neutrinos must have decayed before the onset of the [Big Bang Nucleosynthesis \(BBN\)](#). Consequently, the production and exploration of GeV-scale sterile neutrinos is feasible via accelerator experiments [2.1](#).

keV mass scale

The main focus of this thesis is a sterile neutrino on the keV mass scale. In this

case, the sterile neutrino is a suitable dark matter candidate. Depending on the production mechanism, the sterile neutrino can be categorized as [Warm Dark Matter \(WDM\)](#) or [Cold Dark Matter \(CDM\)](#). A first hint for a keV sterile neutrino could provide the X-ray Multi-Mirror (XMM)-Newton. It measures X-rays from the decay of a sterile neutrino into an X-ray and active neutrino. The satellite observed a signal at an energy of 3.5 keV, which corresponds to a sterile neutrino with a mass of 7 keV [28]. Another way to search for sterile neutrinos is via the kinematics of single β -decay. It is sensitive to sterile neutrino masses up to the Q-value of the decay. Due to its ultra-luminous tritium source, the KATRIN experiment is well suited for the keV sterile neutrino search. To cope with the high count rates when probing the entire tritium β -decay spectrum, a new detector and readout system is currently being developed in the scope of the TRISTAN project. The signature of the sterile neutrino is a spectral distortion with a kink-like feature. Further details of the TRISTAN project will be discussed in chapter 3.

eV mass scale

Experiments such as the Gallium Experiment (GALLEX) [29] and the Soviet-American Gallium Experiment (SAGE) [30] are experiments in short baseline neutrino oscillation experiments and measured a too-low neutrino flux. Both experiments detected a deficit in the neutrino flux, particularly in anti-neutrinos. The Baksan Experiment on Sterile Transitions (BEST) confirms these results [31]. One possible explanation for the observed anomaly is the oscillation of the active neutrino into a sterile one. Since an eV-sterile neutrino would also distort the β -decay spectrum in the region near the endpoint, the KATRIN experiment is also sensitive to it. Current studies can already exclude a large region of the relevant phase space. More details can be found in [32].

3. The KATRIN Experiment

The Karlsruhe Tritium Neutrino (KATRIN) experiment uses the kinematics of single β -decay, as detailed discussed in section 2.3, to directly measure the neutrino mass. The effective electron antineutrino mass is determined via an analysis of the endpoint range of the tritium spectrum at 18.6 keV, see fig. 2.3. In 2016, the experiment was commissioned using calibration sources. Subsequently, the first measurements with tritium were carried out [33]. Recently, the KATRIN collaboration has published the first sub-eV limit on the effective antineutrino mass of $m_b < 0.8 \text{ eV}$ (90% C.L.) [34].

The following section will briefly describe the KATRIN experiment. In section 3.2, the TRISTAN project will be introduced. Here, the keV-scale sterile neutrino search with the KATRIN experiment will be discussed.

3.1. Experimental Setup

A schematic drawing of the KATRIN experiment is shown in fig 3.1. The experimental apparatus has a length of 70 m and a maximum height of 10 m. The beamline is subdivided into several sections that will be discussed in the following paragraphs. If not stated otherwise, the information was taken from [35].

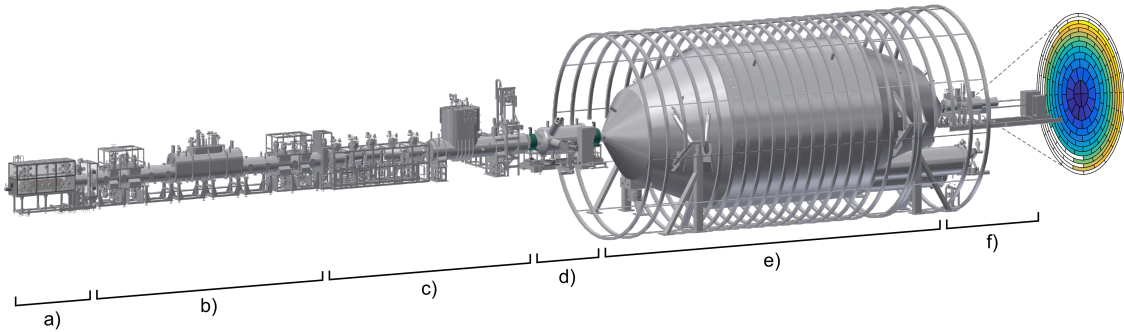


Figure 3.1: The KATRIN beamline. (a) Rear section, (b) Windowless Gaseous Tritium Source (WGTS), (c) Transport section, (d) Pre-spectrometer, (e) Main spectrometer, (f) Focal Plane Detector (FPD). Figure courtesy of the KATRIN collaboration.

Rear Section

The rear section at the beginning of the beamline contains the rear wall, some diagnostic instruments, including the [electron gun \(e-gun\)](#) and the [Beta-Induced X-ray Spectroscopy \(BIXS\)](#) system, and monitoring devices. The rear wall is a large stainless steel disk coated with gold and defines the electric potential of the tritium source relative to the spectrometer voltage. The [e-gun](#) is most important for

calibration purposes and monitoring the source activity.

Windowless Gaseous Tritium Source (WGTS)

The WGTS is the electron source of KATRIN. The short half-life of molecular tritium, which is 12.6 y, allows for a high electron rate. This is crucial to counteract the low electron rate at the end of the spectrum. The endpoint has a Q-value of 18.6 keV. Tritium decays in the following manner:



The WGTS is kept at a purity of more than 95 %. Achieving a very high and stable decay rate of 10^{11} Bq (± 0.1 %) is made possible through a closed-loop system. The tritium injection is centrally initiated and flows outward in both directions, enabling a tritium flow of 40 g per day. A strong magnetic field surrounding the source ensures the electrons flow into the transport section.

Transport Section

The transport section guides the electrons to the spectrometer, ensuring no tritium reaches this component. Therefore, the tritium flow is significantly reduced by 14 orders of magnitude, a task accomplished through the combined efforts of the Differential Pumping Section (DPS) and the Cryogenic Pumping Section (CPS). In the DPS, tritium molecules are pumped out by many Turbo Molecular Pumps (TMPs), operating at a temperature of 77 K. In the CPS section, the remaining tritium is trapped on the argon-covered tube surface, which has a temperature of 3 K and requires cleaning after 60 days. High magnetic fields are implemented in the entire transport section to guide the electrons to the spectrometer. Additionally, the individual transport elements are strategically tilted relative to each other to prevent a direct line of sight.

Spectrometer Section

The spectrometer section comprises the pre-spectrometer and the main spectrometer, serving as key components in the KATRIN beamline. Both spectrometers operate based on the MAC-E principle. The pre-spectrometer functions as a preliminary filter for the main spectrometer. The filter principle is shown in fig. 3.3.

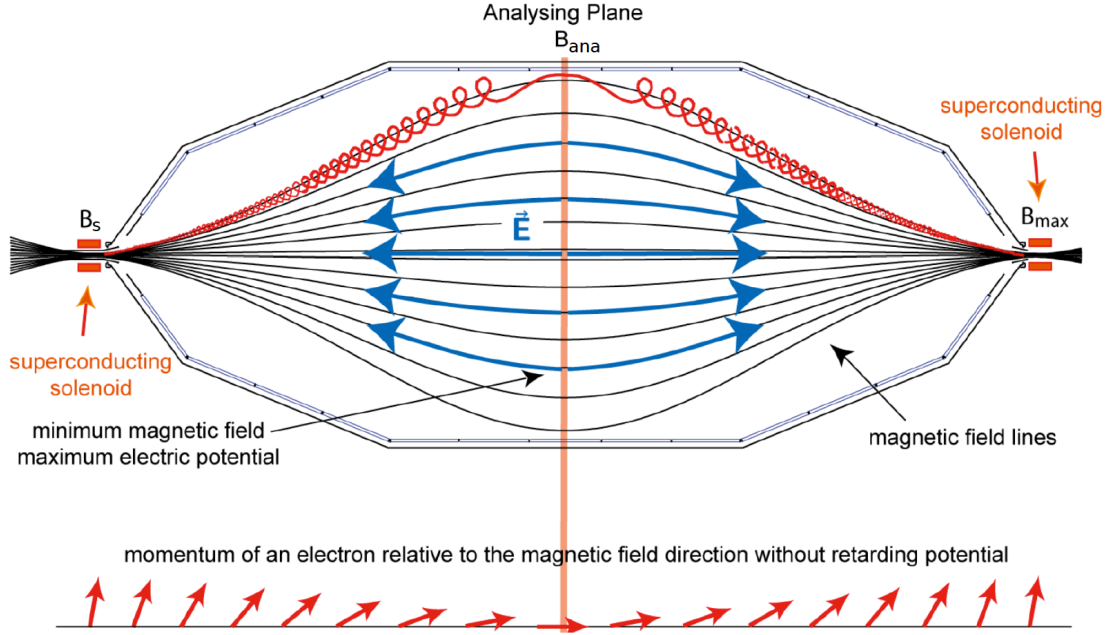


Figure 3.2: MAC-E filter principle. The electrons (red line) enters the spectrometer from the transport section (left side). Due to the magnetic fields (black lines) the transversal component of the electron energy is converted into a longitudinal one. Figure adapted from [36].

The main spectrometer has an length of 23.3 m, a diameter spanning 10 m, and a voluminous capacity of 1400 m³. By applying a negative electrical potential U , only electrons with higher energy than $U \cdot e$ (where e is the elementary charge) can pass this barrier and be subsequently detected by the [Focal Plane Detector \(FPD\)](#). Therefore, the spectrometer acts as a high-pass filter. Since the kinetic energy of an electron can be oriented vertically to the electrical potential, aligning the energy parallel to the electrical potential is necessary for the effective operation of the filter principle. Therefore, two superconducting magnets at both ends of the spectrometer generate a magnetic field. This field is strong at the sides and weak towards the center, as illustrated in fig. 3.3. In adiabatic motion, the electron's orbital magnetic moment is denoted as

$$\mu \approx \frac{E_{\perp}}{B} \quad (13)$$

and remains conserved. Consequently, as the electron progresses from the strong magnetic field B_{\max} at the entrance of the MAC-E filter to the minimal field B_{ana} in the analysis plane, the transverse momentum component transforms into a longitudinal one. Consequently, the transversal energy reaches its minimum at the analysis plane. The energy resolution ΔE of the efficiency of the transformation is related to these magnetic fields as the following:

$$\frac{\Delta E}{E} = \frac{B_{\text{ana}}}{B_{\max}}. \quad (14)$$

With magnetic fields of $B_{\text{ana}} = 3 \cdot 10^{-4} \text{ T}$ at the analysis plane and $B_{\text{max}} = 6 \text{ T}$ at the maximum, the spectrometer achieves an energy resolution of 0.93 eV . The influence of the earth's magnetic field is shielded through a system of air coils surrounding the spectrometer.

Another effect that happens in the spectrometer is the magnetic mirror effect. Due to the high difference in the magnetic fields, electrons that traveled a long distance through the source, exceeding a certain angle, will be reflected in the spectrometer. With a magnetic field strength of $B_{\text{S}} = 3.6 \text{ T}$ in the source and a maximal magnetic field of $B_{\text{max}} = 6 \text{ T}$, a maximum acceptance angle Θ_{max}

$$\Theta_{\text{max}} = \arcsin \sqrt{\frac{B_{\text{S}}}{B_{\text{max}}}} \approx 51^\circ. \quad (15)$$

can be achieved. After having passed the analysis plane, the electrons are re-accelerated and finally reach the detector. By varying the retarding potential, an integral measurement can be performed, i.e. the electrons are counted at the detector.

Focal Plane Detector (FPD)

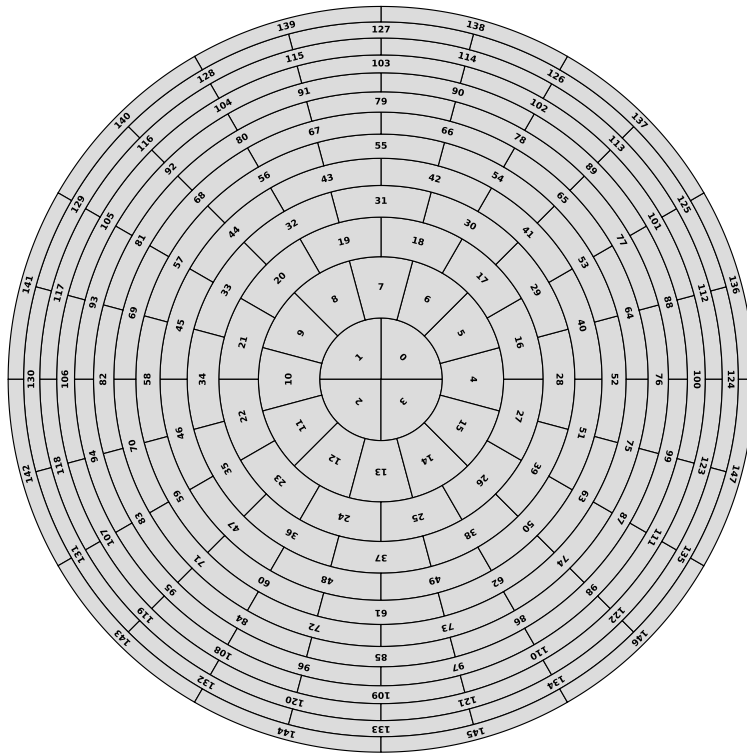


Figure 3.3: Pixel layout of the focal plane detector with a ring-wise structure of 149 pixels. Each pixel has the same area of 44 mm^2 [37]. Figure courtesy of A. Schwemmer.

The [FPD](#), shown in fig. 3.3, is located at the exit of the main spectrometer and

consists of 149 pixels. This silicon **Positive Intrinsic Negative (PIN)** detector features pixels with uniform areas arranged ring-wise to investigate radial and azimuthal effects. The detector is designed to count the filtered electrons and can accommodate rates of tens of kcps. While the energy resolution of the **FPD** is relatively poor, with $\Delta E_{\text{FWHM}} = 1.52 \text{ keV}$ at 18.6 keV , this characteristic is not crucial, because the primary function of the **FPD** is electron counting. The relevant factor is the energy resolution of the main spectrometer. A post acceleration after the spectrometer is applied to lower intrinsic detector background in the region of interest.

3.2. Sterile Neutrino Search with the KATRIN Experiment

As explained in section 2.3, for the currently ongoing neutrino mass measurements, the KATRIN experiment probes the energy spectrum of tritium β -decay in the region around the spectral endpoint. From the theoretical point of view, one could discern the shapes corresponding to the three neutrino mass eigenstates. However, due to minimal mass differences, KATRIN cannot resolve the individual mass eigenstates. In the case of a keV-sterile neutrino, a distinct spectral distortion is visible due to the higher mass, which enables its search. Due to the mixing of the active and sterile neutrinos, the β -decay is a superposition of the decay branches of the active and sterile neutrinos, with total differential decay rate $d\Gamma$ [38]:

$$\frac{d\Gamma}{dE} = \underbrace{\cos^2 \Theta_S \frac{d\Gamma(m_\beta)}{dE}}_{\text{Active neutrino part}} + \underbrace{\sin^2 \Theta_S \frac{d\Gamma(m_4)}{dE}}_{\text{Sterile neutrino part}}. \quad (16)$$

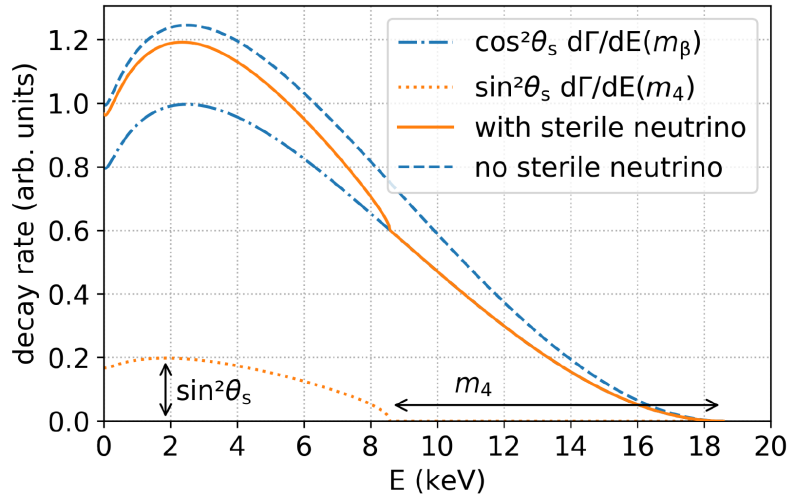


Figure 3.4: Imprint of the sterile neutrino in the electron energy spectrum of single β -decay. The blue dash-dotted line shows the decay branch of the active neutrinos. The decay branch of the sterile neutrino (dotted orange line) is characterized by the mixing amplitude $\sin^2 \theta_s$ and the mass m_4 . The total energy spectrum is the superposition of these branches. The imprint of the sterile neutrino is a spectral distortion with a kink-like signature. Source: [39].

In particular, the spectral distortion is more pronounced for high mixing amplitudes. Additionally, the mass eigenstate m_4 plays a crucial role. The endpoint of the sterile branch at the energy $E_0 - m_4$ leads to a kink-like signature, see fig. 3.4.

The existing KATRIN data allow searching for sterile sterile-to-active mixing amplitude. A first exclusion limit on the active-sterile mixing amplitude could be set with a value of $\sin^2 \Theta_s < 5 \cdot 10^{-4}$ (95% C.L.) with a sterile neutrino mass of up to 1.6 keV [40]. The aim of the TRISTAN project is to extend the mass range to the entire tritium spectrum. As already discussed above, this leads to very high count rates at the detector. Since the current KATRIN FPD is not designed to handle such high rates of 10^8 cps, the TRISTAN detector system is currently being developed. The goal is to reach a ppm-level sensitivity on the mixing angle [1].

Detector Requirements and Data Analysis

For the neutrino mass measurements, the KATRIN experiment uses the integral measurement mode. In this mode, only the electrons which passed the spectrometer are counted. For the keV-scale sterile neutrino measurements, also the differential measurement mode will be used. In this mode, the energy of the passing electron is measured. The advantage of combining the integral and differential measurement modes for a keV-sterile neutrino search is that a detailed analysis of the entire spectrum becomes possible. To this end, the retarding potential of the main spectrometer needs to be adjusted to very low values. This results in a notably high electron rate of up to 10^8 cps, which can be distributed over many pixels [1]. This distribution

also helps to reduce pile-up. The TRISTAN detector consists of many hexagonal pixels arranged next to each other to minimize the insensitive area. Each pixel has a circumscribed diameter of about 3.3 mm. Since the collaboration aims to probe mixing angles with a sensitivity at the ppm-level, a good energy resolution of $\Delta E_{\text{FWHM}} = 300 \text{ eV}$ at 20 keV is required to resolve the spectral distortion and kink-like signature. Therefore, low electronic noise levels, as well as efficient charge collection properties, are indispensable. Applying a post-acceleration voltage of up to 20 keV decreases the detector threshold and reduces entrance window effects [41].

An additional challenge is the data processing. Since no commercially available system is compatible with the KATRIN beamline's high vacuum, high voltage, and high magnetic fields, a new data processing system needs to be developed. High-performance readout electronics are required to identify pile-up events and generate real-time spectra to reduce the amount of data. This system should boast a high [Analog-to-Digital Converter \(ADC\)](#) sampling rate and possess a resolution falling within the range of 14 to 16 bits [42]. Consequently, a new [Data Acquisition \(DAQ\)](#) system is under development. More details on the [DAQ](#) system and its requirements can be found in [41, 43, 44].

Development of the TRISTAN Detector

The development of the TRISTAN detector system was performed in several stages. Initially, an extensive characterization of 7-pixel prototype detectors was performed [1]. In later development stages, the performance of detectors with 12, 47, and 166 pixels was investigated. Different experimental setups were used to characterize different physical properties such as the energy resolution, electronic noise, backscattering, and radiation damage. The final detector system will consist of several so-called detector modules placed next to each other. Each detector module consists of a multi-pixel detector with 166 pixels attached to a holding structure and connected to the readout electronics. A technical drawing of a detector module is shown in fig. 3.5

After testing the modules in the laboratory, they were implemented into the KATRIN [Monitor Spectrometer \(MOS\)](#) [45]. The advantage of the experimental setup is that it closely resembles the properties of the KATRIN beamline, providing a representative setting for evaluating the detector module's performance and capabilities. The keV-scale sterile neutrino search is scheduled to begin 2016, nine detector modules will be integrated into the KATRIN beamline, see fig. 3.6a. A potential upgrade involves expanding the detector system with three additional modules on each side, such that a total number of 21 modules with about 3500 pixels are deployed. At the current status, a detector system with nine modules only needs minimal changes to implement in the KATRIN beamline. Detailed information can be found in [45].

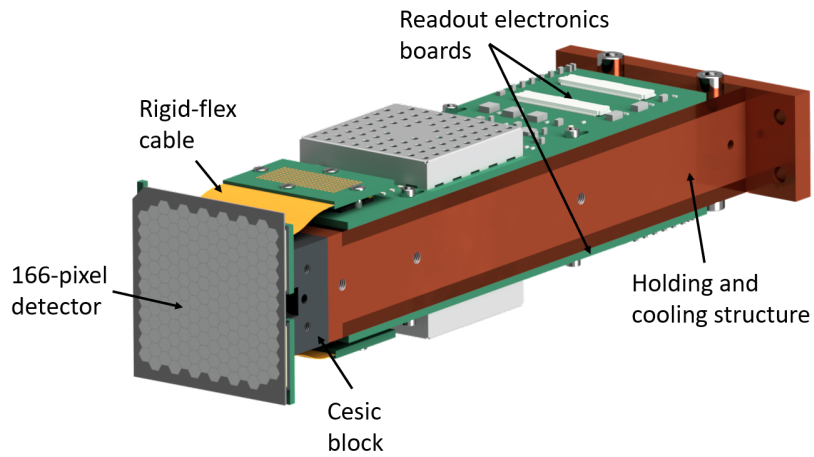
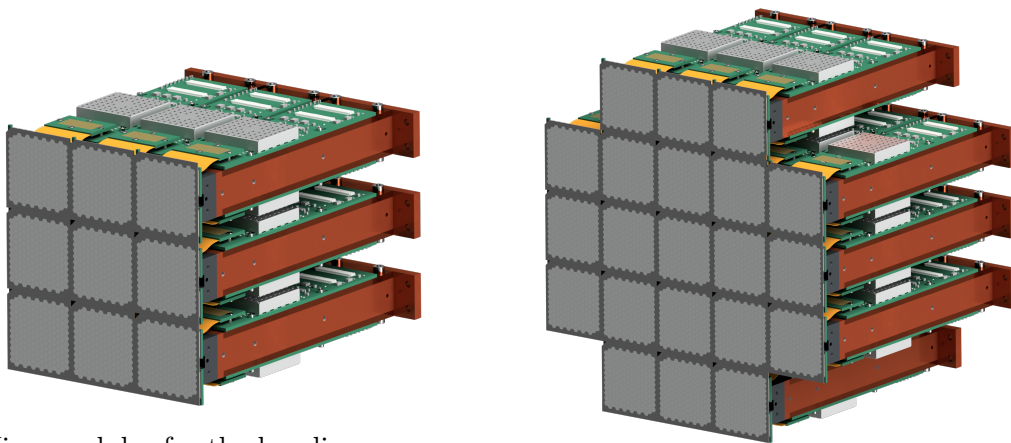


Figure 3.5: The 166-pixel detector module in the front is glued onto a block made of the material Cesium. It acts as a thermal link between the detector and the copper holding and cooling structure. The readout boards, mounted on the top and bottom surfaces of this block, are green, and the rigid-flex cable which connects the detector with the electronic boards, is yellow. Source: [45].



(a) Nine modules for the baseline design (3x3 detector modules).

(b) Potential detector upgrade (21 modules).

Figure 3.6: Technical drawing showing the final TRISTAN detector system. (a) In the baseline design, nine modules with about 1500 pixels will be installed in the detector section of the KATRIN experiment. (b) Potential upgrade of the detector system consisting of 21 modules with roughly 3500 pixels. Source: [45].

In the next chapter, the operating principle of **SDDs** as well as the readout electronics will be discussed in more detail.

4. The TRISTAN Detector System

The TRISTAN detector is based on the [Silicon Drift Detector \(SDD\)](#) technology. This technology provides several advantages, i.e. an excellent energy resolution, see section 3.2. This chapter gives an overview of the [SDD](#) technology and the operating principle of the TRISTAN detector. In section 4.1, an introduction to semiconductors is given, followed by an overview of semiconductor detectors in chapter 4.2. The [SDD](#) technology and the signal readout chain are discussed in sections 4.3 and 4.4, respectively.

4.1. Introduction to Semiconductor Materials

All elements can be categorized into conductors (metals), semiconductors, and insulators. In the band model in crystals, the permissible states for electrons are illustrated by bands. There is the valence band, the highest full occupied energy band at 0 K, and the conductive band, which is responsible for the conductivity. In conductors, electrons can move freely within the conduction band as there is no gap between the valence and conduction bands. On the other hand, the conduction band in insulators is empty due to the substantial band gap being larger than the thermal energy of the electrons. Therefore, they do not conduct electricity.

Semiconductors are particularly intriguing because their conductivity lies between metals and insulators. The conductivity of semiconductors is temperature-dependent. Due to the small band gap, electrons from the valence band can transition to the conduction band through thermal excitation. Fig. 4.1 illustrates the band structure for all three types. The conduction band is empty at a temperature of $T = 0$ K, rendering the semiconductor functionally equivalent to an insulator. As the temperature increases, the probability of electrons transitioning to the conduction band rises. Consequently, semiconductors exhibit more pronounced conductor-like behavior at higher temperatures [46, 47].

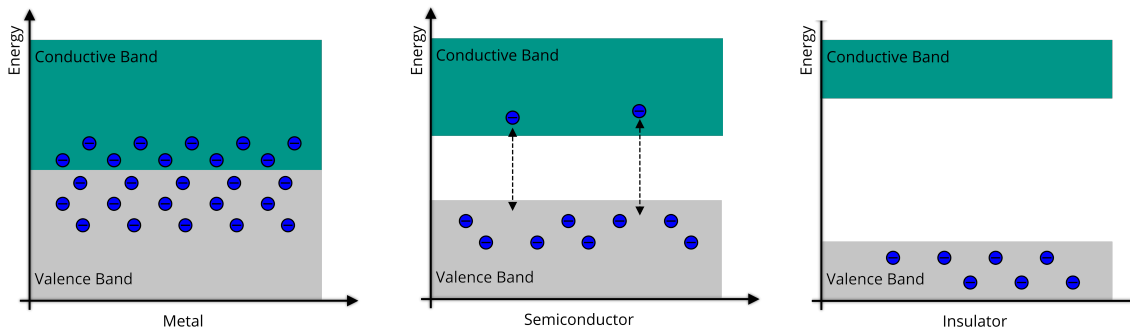


Figure 4.1: For the metals (left), there is no gap between the valence and conductive band. The electrons (illustrated in blue) can move freely as charge carriers. Insulators (right) have a very high band gap, which leads to no conductivity. Semiconductors (center) lie in between depending on temperature and their doping. Figure taken from [22].

Silicon, categorized as a type IV material in the periodic table, is one of the most utilized semiconductors. The conductivity of semiconductors, such as silicon, can be modified through a process known as doping. During this procedure, an atom within the crystal lattice is substituted with another element. Doping can be classified into electron donor (n-type) and acceptor (p-type). Donors, typically atoms from type V, contribute an additional electron and introduce an energy level proximate to the conduction band. This process yields free electrons within the conductive band even at lower temperatures. On the other hand, acceptors (typically from type III) create an energy level near the valence band. However, an additional hole is formed within the valence band in this case [47]. An illustration of these processes is provided in fig. 4.2.

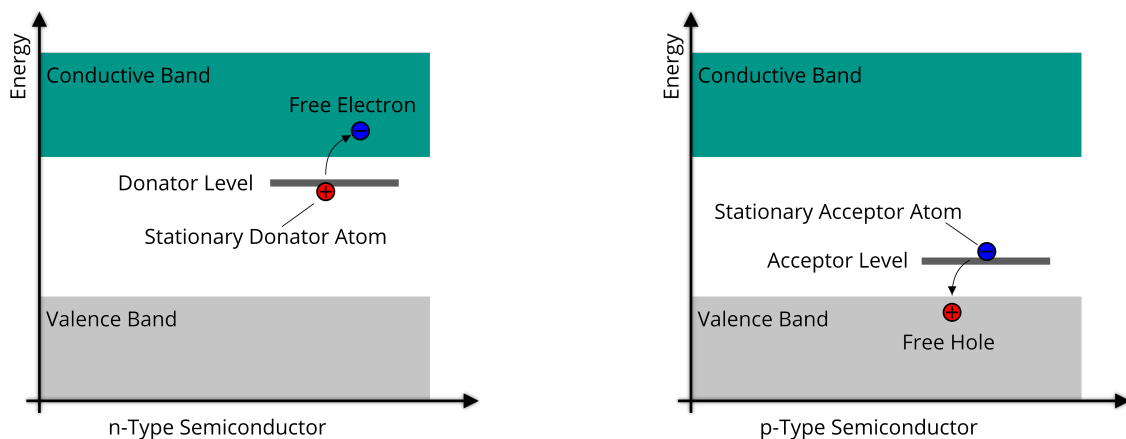


Figure 4.2: Illustration of band structure for doped semiconductors. The band structure of an n-doped semiconductor is depicted on the left-hand side. It results in an additional energy level within the forbidden gap. On the right-hand side, the band structure represents a p-doped semiconductor where one electron is deficient. This deficiency facilitates the excitation of an electron to the added acceptor level created by the doped atom, generating a free hole in the valence band. Figure taken from [22].

4.2. Semiconductor Detectors

In 1983, the concept of using semiconductors as detectors for ionizing particles was first introduced by E. Gatti and P. Rehak [48]. When a particle penetrates a material such as silicon, it generates numerous electron-hole pairs proportional to its energy. However, the number of charge carriers created is much smaller than that of free charge carriers generated through thermal excitation. Consequently, distinguishing the signal from the background noise becomes challenging [47]. One potential solution to this issue is to reduce the number of free charge carriers. However, implementing cooling near absolute zero is technically challenging. Modifying the semiconductor into a reversed-bias pn-junction is a more practical solution because it generates a depleted region without any free charge carriers.

The schematic representation of a pn-junction is illustrated in fig. 4.3. This junction comprises n-type and p-type doping regions that are interconnected. The n-type material has excess electrons, while the p-type material has excess holes. Consequently, the material self-adjusts to balance this surplus, causing electrons to flow into the p-type region and holes into the n-type region. Upon arrival, they recombine with the dopant atoms, creating oppositely charged atoms. This process establishes an electric field opposing the movement of the free charge carriers, thus hindering further diffusion. As a result, a dynamic equilibrium is achieved in the transition area. The inherent voltage associated with this equilibrium is called the diffusion voltage $U_{\text{diffusion}}$, and the region free of charge carriers is referred to as the depletion zone [46, 47].

An additional external voltage U_{bias} can be applied in the same direction as the diffusion voltage $U_{\text{diffusion}}$ to increase the depletion region. When a particle enters the detector material, a charge cloud is formed. The electric fields inside the depleted zone guide the electrons towards the n-type side, which serves as the anode for charge readout. Similarly, holes exhibit analogous behavior. This type of detector is referred to as a PIN-diode.

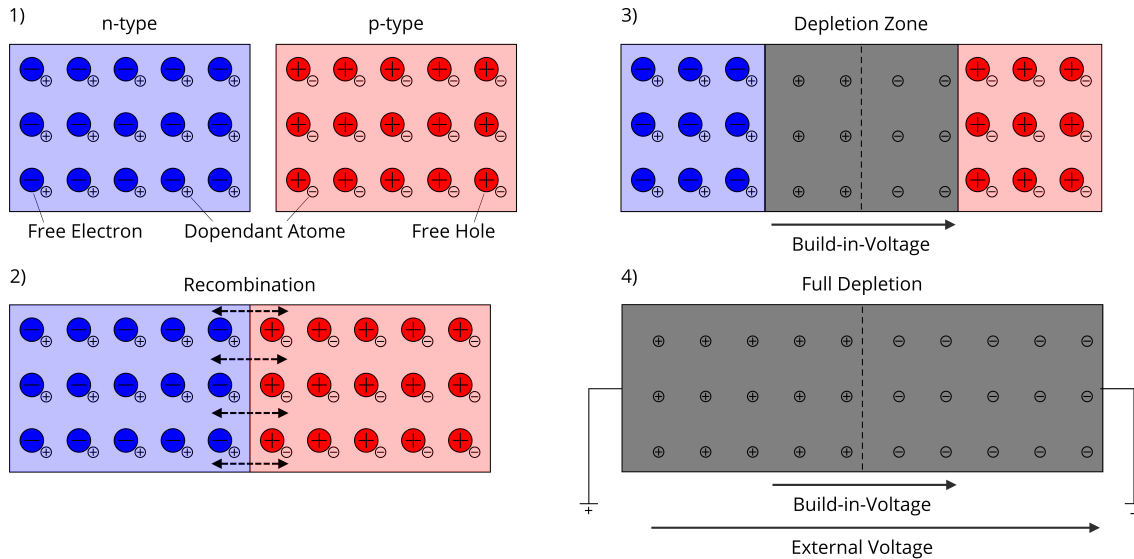


Figure 4.3: The reversed-bias pn-junction creation involves several steps. The initial depiction presents an n-doped semiconductor (blue) with excess free electrons and a p-doped semiconductor (red) with additional free holes. Picture 2) illustrates the recombination process upon connecting the two doped materials. 3) Free charge carriers recombine, forming a depleted zone (grey area) devoid of charge carriers. The diffusion current and the built-in voltage $U_{\text{diffusion}}$ establish an equilibrium. 4) By applying an external voltage, the depletion zone can be expanded by applying an additional voltage U_{bias} . Figure taken from [22].

4.3. Silicon Drift Detectors

To better understand the SDD technology and the concept of sideways depletion, fig. 4.4 illustrates the steps from a PIN-diode to a SDD. Like the reversed-bias pn-junction, the PIN-diode comprises differently doped electrodes on each detector side. The entrance window is doped with a p-type material. At the same time, the bottom side corresponds to the anode. It is doped with n-type material, creating a depletion zone between the two sides, see fig. 4.4a. In the next step, shown in fig. 4.4b, the anode is scaled down and positioned at the center. Reducing the anode size (and, therefore, its capacity) can reduce semiconductors' electronic noise. The resulting vacant space is filled with p^+ -doped material. In this configuration, potential lines guide charge carriers efficiently toward the anode near the center. In contrast, little to no charge collection is viable at the peripheries since the electric fields do not end on the detector anode. Consequently, the p^+ -doped material next to the anode is subdivided into numerous smaller segments. A graded potential, ranging from U_{RingX} to U_{Ring1} , is applied, with U_{RingX} being the strongest potential at the sides and U_{Ring1} the weakest next to the anode. This, in conjunction with a bias voltage U_{bias} applied to the entrance window, generates an electric field directing every charge within the entire detector volume toward the anode [48]. Fig. 4.4c presents an illustration wherein a color scheme visually represents the electric potential. The scheme of a SDD is shown in fig. 4.5 and the electric potential in fig. 4.6.

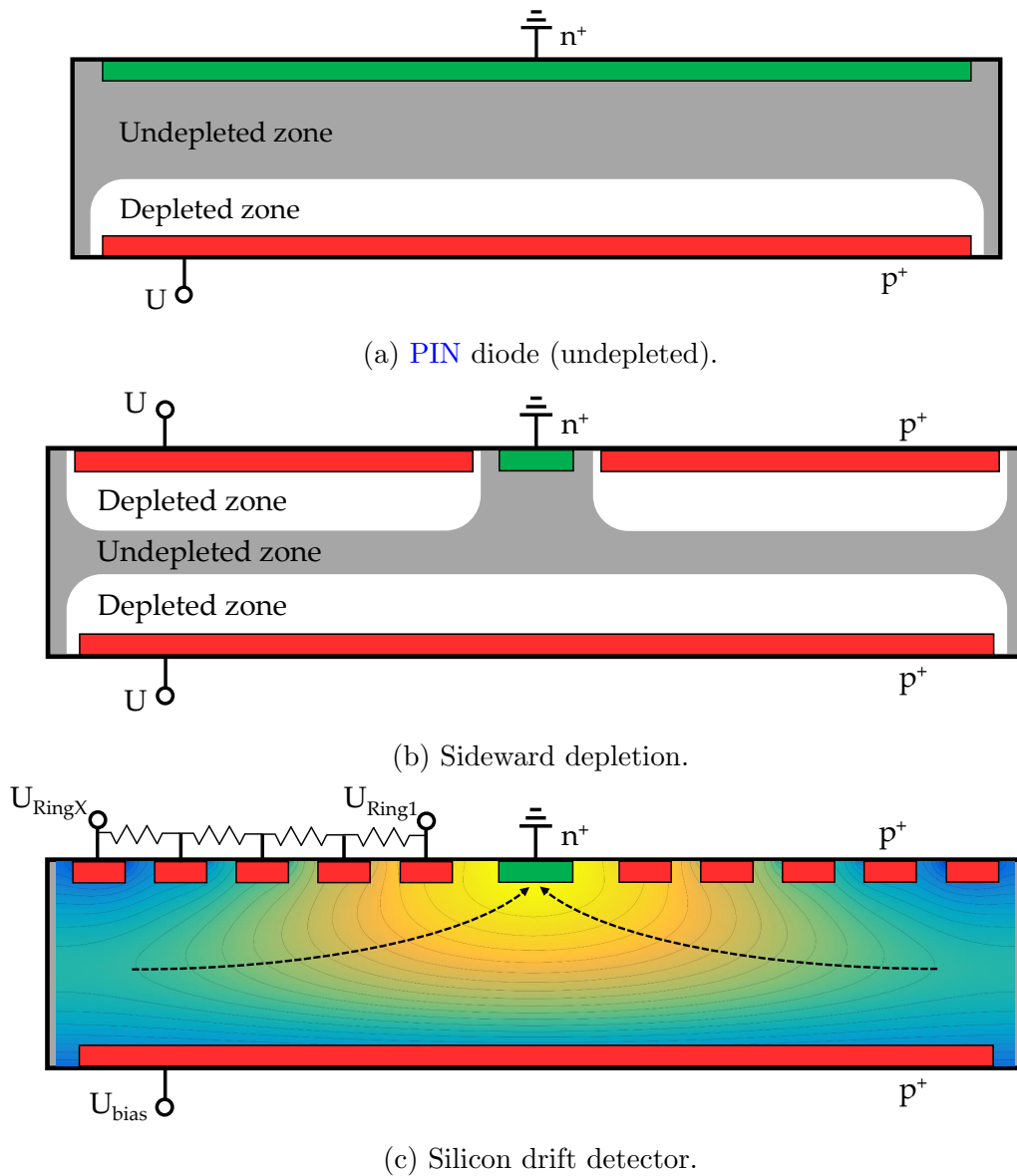


Figure 4.4: The evolution from a pn-junction or pin-detector to an SDD is depicted in steps (a) to (c). (a) In a PIN diode configuration, the p^+ and n^+ (anode) electrodes extend across the upper and lower surfaces. Achieving full depletion of the detector volume requires applying a sufficiently high bias voltage, although, in this illustration, the detector is not entirely depleted. (b) Using the concept of sideward depletion, the detector area can still be fully finished with a much smaller anode. However, since not all electric field lines end on the anode, only a fraction of all charge carriers created in the detector volume reach it, effectively decreasing the sensitive detector volume. (c) A SDD design subdivides the p^+ electrodes on the anode side into multiple drift rings. Applying voltage to these drift rings (with increasing positivity towards the anode) generates an electric field with a dominant component parallel to the surface. This field effectively guides signal electrons toward the anode. The color map represents the electric potential within the detector. Figure courtesy of F. Edzards.

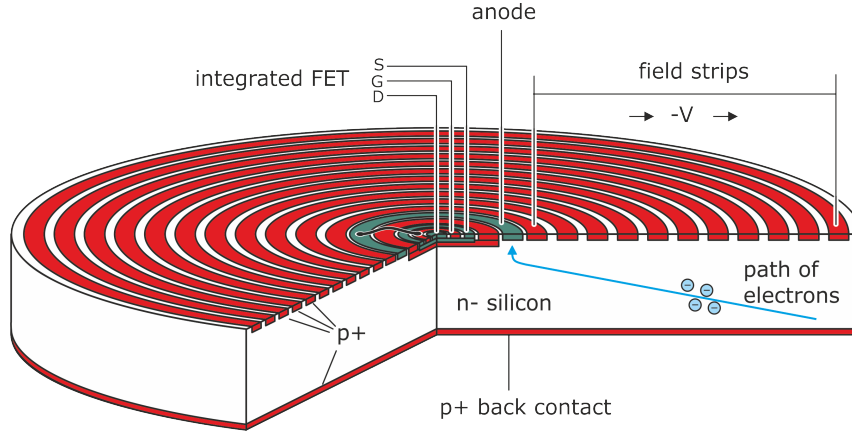


Figure 4.5: Scheme of an [SDD](#) for the TRISTAN project. The entrance window is on the bottom side. The drift rings, doped with p^+ , are shown in red. The anode, doped with n^+ , is shown in green. All electrons are guided to the anode in the center. Figure adapted from [49].

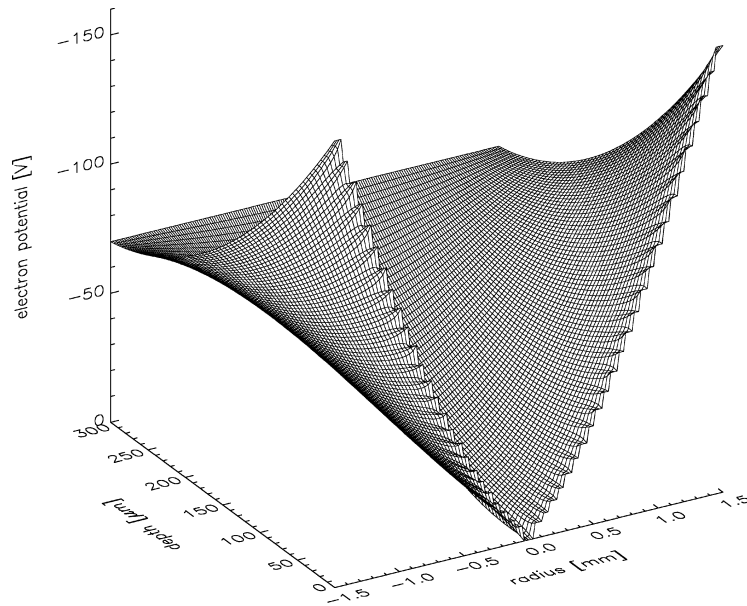


Figure 4.6: Simulation of the electrical potential of an [SDD](#). The rear flat region illustrates the applied voltage at the entrance window side to the p^+ electrode. On the radial axis, the set potential for the drift rings is visible at a zero depth. The potential reaches its minimum at the central anode. Electrons from all points within the detector are directed towards the anode. Figure taken from [49].

Characteristic of an [SDD](#) is its small anode capacity, typically on the order of 100 fF, chosen to enable a good noise performance and accommodate high rates [49]. An internal [nJFET](#) is integrated into each anode to take full advantage of the small anode capacitance. Combined with the ETTORÉ [Application-Specific Integrated Circuit \(ASIC\)](#), it is a pre-amplifier sensitive to the collected charge. An internal [nJFET](#) was preferred over an external one to eliminate bond connections. The

integrated nJFET is enclosed by an IGR implantation to prevent any charges from being lost. Applying a negative potential to the IGR shapes the fields near the anode so that the electrons can only enter the nJFET via the foreseen path through the anode. The internal nJFET also offers the advantage of closer proximity of the first amplifier stage to the signal, resulting in lower electronic noise and, consequently, improved energy resolution [50].

Charge production and energy resolution

When radiation penetrates the detector, it creates many electron-hole pairs (e-h pairs). For silicon, the energy required to create on average one e-h pair is $\varepsilon = 3.62$ eV at 300 K [51]. The number N of electron-hole pairs within the generated charge cloud is then consequently

$$N = \frac{E}{\varepsilon} \quad (17)$$

with E as the energy of the incoming particle. The number of charge carriers is proportional to the measured energy at the anode. Furthermore, the incoming particle's interaction point can be calculated by the time delay between the point in time of the interaction of the incident radiation and the generation of the signal pulse. This is called drift time [52]. The Fano factor F characterizes the correlation of fluctuations in the number of generated e-h pairs ($\langle \Delta N^2 \rangle$) [46]:

$$\langle \Delta N^2 \rangle = F \cdot N. \quad (18)$$

In silicon, the Fano factor typically is 0.115 [53]. Consequently, this yields a Fano energy resolution σ_{Fano} given by [54]:

$$\sigma_{\text{Fano}}^2 = F \cdot E \cdot \varepsilon. \quad (19)$$

The variance of the peak σ is the sum of the broadening due to Fano statistics and noise, denoted as σ_{Noise} . Detailed noise theory can be found in [55, 56, 57]:

$$\sigma = \sqrt{\sigma_{\text{Fano}}^2 + \sigma_{\text{Noise}}^2}. \quad (20)$$

Since the Fano factor can not be modified, minimizing the electronic noise is essential to optimize the detector performance. The energy resolution is often presented using the Full With Half Maximum (FWHM), behaving with the variance as follows:

$$\text{FWHM} = 2\sqrt{2 \log 2} \cdot \sigma. \quad (21)$$

Entrance Window and Partial Event Mode

As radiation traverses silicon, it generates secondary electrons and holes. Distinguishing between the behavior of these electrons and holes close to the surface and those in the bulk is crucial [58, 59]. Near the entrance window, the electric fields are not strong enough to efficiently guide the electrons to the anode. A simplified model to depict this effect is an entirely non-sensitive layer at the top of the detector, referred to as the dead layer. This layer represents an area where all generated charge carriers are directed to the interface between silicon and silicon oxide, recombining with defects and becoming undetectable. Since a silicon oxide layer is invariably present due to the natural reaction of silicon with oxide in contact with air, artificially adding a silicon oxide layer that closely mimics the natural composition is beneficial. It also protects the detector from further oxidation. A transition area also defines the region between the dead layer and the sensitive detector area. In this transitional zone, only a fraction of the generated charge carriers are guided to the anode, while the rest are lost. Notably, the lost charge ratio increases as the incoming electron's energy decreases. An overview of the charge collection efficiency is illustrated in Fig. 5. The plot is generated using the partial event model, with a detailed explanation available in [58, 59].

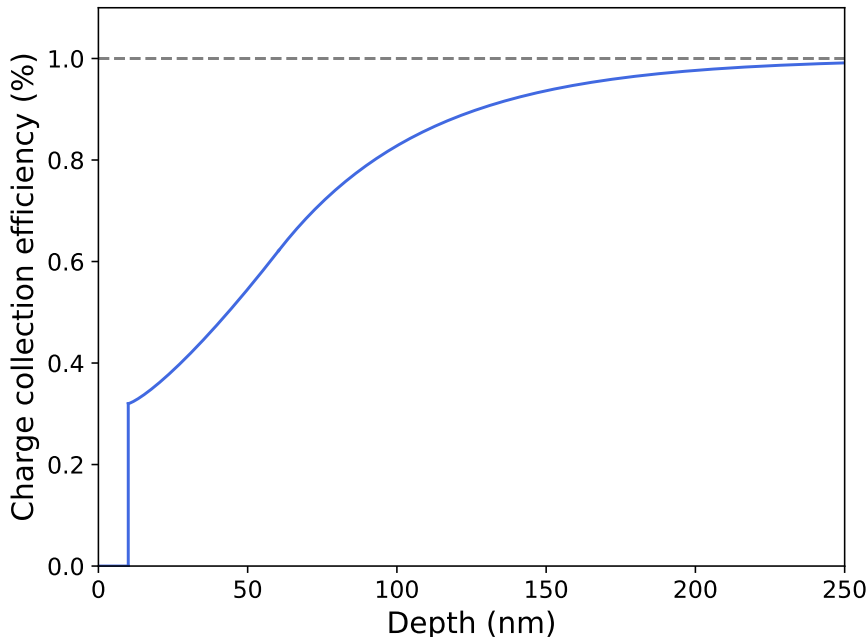


Figure 4.7: Illustration of the charge collection efficiency function. To draw the collection probability for an SDD, the measured values in [60] are used. Silicon oxide thickness $d = 10$ nm, minimal collection efficiency $S = 0.32$. Transition parameter $l = 50$ nm and $\tau = 50$ nm. Curvature parameter $c = 1.26$.

7-pixel detector

In this thesis, all measurements were performed with a TRISTAN detector comprised

of seven pixels. The **SDD** chips are constructed from a silicon wafer with a thickness of $450\ \mu\text{m}$ and feature seven hexagonally shaped pixels, each with a diameter of $3\ \text{mm}$. The hexagonal configuration ensures seamless pixel alignment, eliminating gaps between them while retaining the benefits of a near circular shape of the **SDD**. This layout of the 7-pixel is illustrated in fig. 4.8. The arrangement of the seven pixels resembles a honeycomb pattern, with the **Central** pixel designated as **CC** (Center). The surrounding pixels are labeled based on their cardinal directions: **NN** (North), **NE** (Northeast), **SE** (Southeast), **SS** (South), **SW** (Southwest), and **NW** (Northwest).

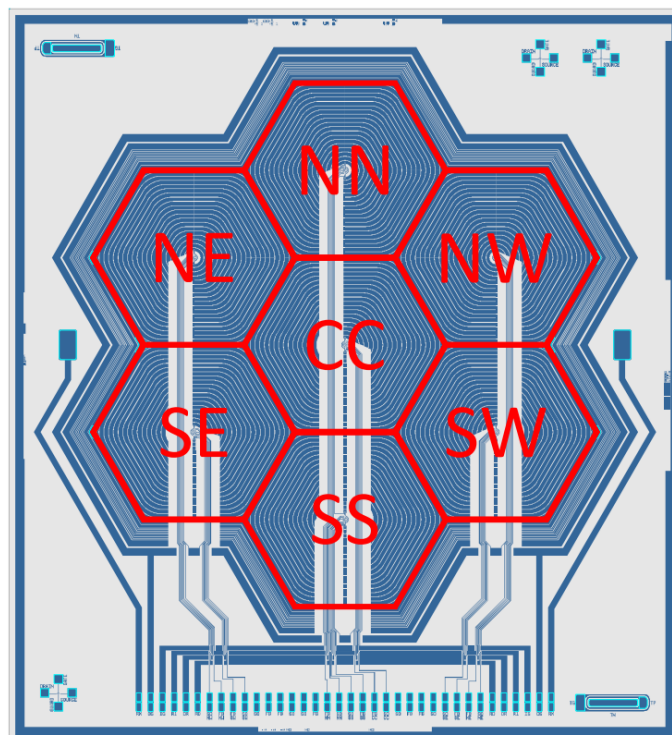


Figure 4.8: Illustration of the nomenclature of a 7-pixel detector. Figure courtesy of P. Lechner.

Overview of Important Detector Voltages

Several critical detector voltages are applied to the **SDD** to achieve optimal detector performance. These will be briefly explained in the following [61].

- **Back Contact (BC)**: It is applied to the back contact on the entrance window side to deplete the detector volume. This voltage extends the depletion zone of the detector throughout the bulk. Expected values for the **SDD** are in the range of $-120\ \text{V} \leq V_{\text{BC}} \leq -80\ \text{V}$.
- **Back Frame (BF)**: This voltage is applied to the ring surrounding the **BC** implantation of the entrance window, contributing to the definition of the electrical field for the outer borders of the pixels and shielding it from leakage

current originating from the undepleted material. Anticipated values for the TRISTAN detector fall within the range of $-130\text{ V} \leq V_{\text{BF}} \leq -90\text{ V}$.

- **Ring 1 (R1) and Ring X (RX):** The innermost drift ring **R1** and the outermost drift ring **RX** generate the potential gradient that guides the electrons to the collecting anode. For **R1**, expected values are $-15\text{ V} \leq V_{\text{R1}} \leq -5\text{ V}$, and for ring X, $-150\text{ V} \leq V_{\text{RX}} \leq -100\text{ V}$.
- **V_{SSS} and V_{D} :** These represent the supply voltages for the **nJFET**. V_{SSS} regulates the **nJFET** source currents, while the bias current V_{D} determines the voltage at the **nJFET** drain [62]. Commonly, values of $V_{\text{SSS}} = -3.9\text{ V}$ (which corresponds to a current of $I_{\text{SSS}} = 200\text{ }\mu\text{A}$ per pixel) and $V_{\text{D}} = -7.4\text{ V}$ are utilized.
- **V_{ResH} and V_{ResL} :** The TRISTAN detectors operate in a pulsed-reset mode, utilizing external electronics to initiate a reset diode. The V_{ResH} and V_{ResL} voltages determine the reverse-biasing and forward-biasing states of the diode. The anode is discharged, and the reset is initiated by applying the voltage V_{ResH} . To prevent resetting between the rectangular reset pulses, the voltage V_{ResL} is applied to the anode reset diode. Typically, values of $V_{\text{ResH}} = 4.0\text{ V}$ and $V_{\text{ResL}} = 10\text{ V}$ are employed.

4.4. Readout Electronics

The readout system consists of a detector board with the amplifier ETTORE and the XGLab bias board, providing essential supply voltages for full depletion, drift fields, and amplifiers within the detector. The **SDD** is installed on the detector board illustrated in fig. 4.9, which hosts the ETTORE **ASIC** amplifier. The XGLab biasing and control board consists of a buffer board for the signal outputs of the detector and a part that supplies the required detector voltages, illustrated in fig. 4.10. Additionally, it provides the reset pulses for the **SDD**. The installed buffer board further amplifies the detector signal by a factor of 2 and allows the shift of the signal output baseline. All data were sent to the **DAQ** system, shown in fig. 4.11. The subsequent part will elaborate on the read chain.

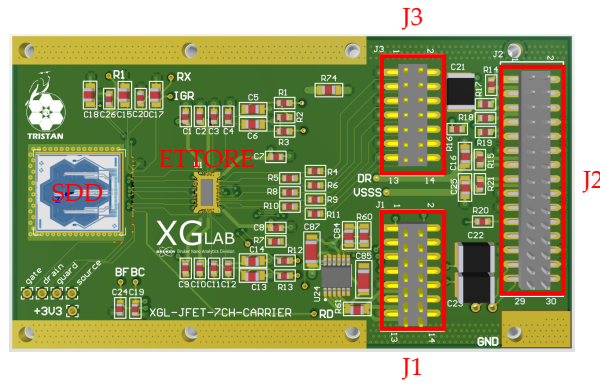
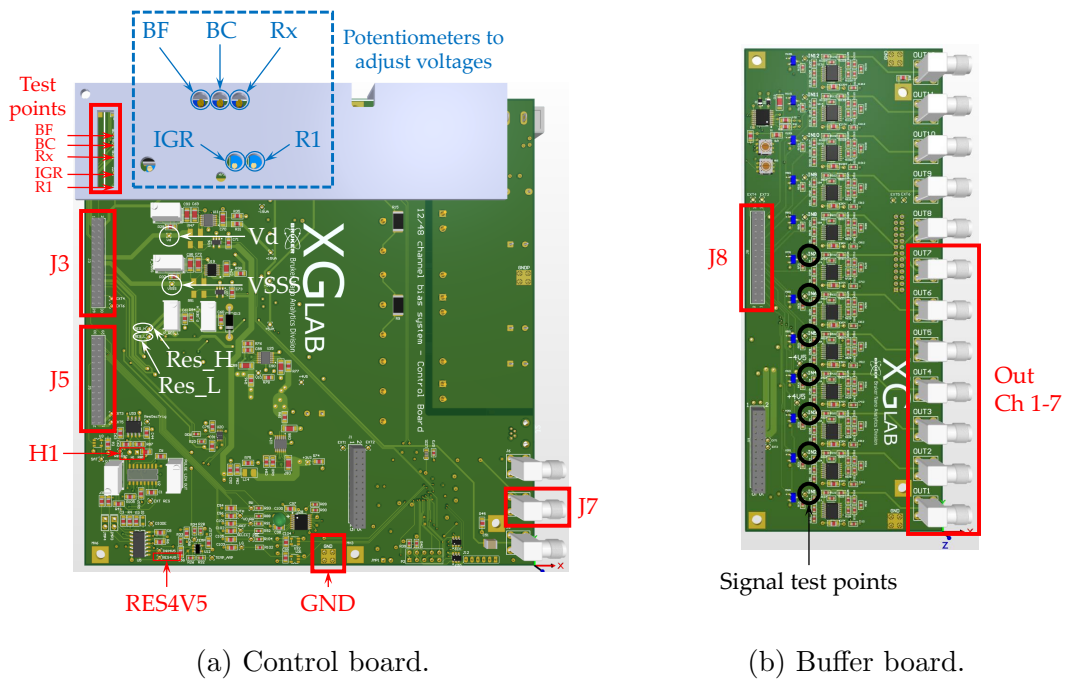


Figure 4.9: Technical drawings of the PCB. The seven hexagonal pixels are positioned on the left side, while connections J1, J2, and J3 are established on the right side, linking to the bios board. Figure taken from [61].



(a) Control board.

(b) Buffer board.

Figure 4.10: Technical drawings of the control board (a) and buffer board (b) of the detector bias system. The relevant connections and test points are indicated. J3, J5, and J8 connect the control board to the detector board, and OUT1-OUT7 connect the signal output to the DAQ system. The detector voltages can be adjusted via potentiometers (blue). Figure taken from [61].



Figure 4.11: A photograph of the DAQ system CAEN DT572. It is an 8-channel 14-bit digitizer with a sampling rate of 250 MS/s [63].

An exceptionally low signal noise is necessary to achieve the high energy resolution necessary for resolving spectrum distortions in the β -decay spectrum. Consequently, the TRISTAN detector employs a [Charge Sensitive Amplifier \(CSA\)](#) comprising a [nJFET](#), seamlessly integrated into the anode structure of each pixel. This initial amplification occurs within the [SDD](#) chip. The subsequent amplification stage involves using the ETTORÉ [ASIC](#), specifically developed for the TRISTAN detector [64]. It consists of two amplifier stages.

The first amplifier stage operates as a DC-coupled amplifier. In the negative [CSA](#) loop, the charge carriers collected at the anode charge the feedback capacitor ($C_{FB} = 25$ fF). As a result, the output of the [CSA](#) increases. Its behavior in the presence of leakage current is shown in fig. 4.13a, resulting in a linearly increasing ramp. When a particle hits the detector, a significant amount of charge is rapidly produced, leading to a step in the voltage output signal. The amplitude of this step is directly proportional to the deposited energy. To prevent saturation of the pre-amplifier, the charges collected at the feedback capacitor are drained via a reset diode, inducing a rapid waveform decrease back to its initial value. The reset can be initialized periodically or with the level-sensitive reset. In this level of sensitive-reset mode, the detector is resettled as soon as one of the pixels surpasses a predetermined voltage threshold. Fig. 4.13a illustrates a waveform in the first amplifier stage. The output of the second stage is an AC coupled signal with a time constant of $\tau \approx 15$ μ s. The signal is visible as a rapid increase of the waveform followed by an exponentially decaying tail, as illustrated in fig. 4.13b. It is crucial to note that the [ASIC](#) must be deactivated during the reset process.

A practical choice for energy reconstruction is the trapezoid filter, which is applied to the second amplifier stage following a pole-zero correction that counteracts the exponential decay, resulting in a straight stair-like waveform. The filter encompasses both a filter rise time and a flat-top time, with the flat-top between two filter rise times. The filter rise time establishes the average within the selected

time window, and the flat-top defines the separation between the two filter rise times. Subsequently, the difference between both averages is calculated, resulting in a trapezoidal shape. The event's energy can be easily determined at the top of this trapezoid. An illustration of a trapezoid filter is presented in fig. 4.14. A typical value for the filter rise time is about 2 μs and for the flat-top, about 0.192 μs .

The final component in the readout chain is the CAEN DT5725 DAQ system. This 8-channel 14-bit digitizer can capture waveforms at a sampling frequency of 250 MS/s. Additionally, it incorporates a Digital Pulse Processor (DPP) that enables Pulse Height Analysis (PHA) and Pulse Shape Discrimination (PSD). Leveraging a Field-Programmable Gate Array (FPGA) and two trapezoidal filters, the DAQ system can trigger events and reconstruct energy information. The DAQ system offers three distinct data acquisition modes: waveform, list, and spectrum mode:

- **Waveform mode:** In this acquisition mode, the entire waveform of every event with a time stamp is recorded. While this acquisition mode offers comprehensive information about the events, it requires a substantial amount of disk space to store all the waveforms.
- **List mode:** In this acquisition mode, the reconstructed energy with its timestamp is recorded. While this acquisition mode offers comprehensive information about the events, it requires a substantial amount of disk space to store all the waveforms.
- **Spectrum mode:** In this acquisition mode, the data storage requirements are minimized as only the energy spectra are retained. The reconstructed energies are organized into histograms, making it an efficient choice for experimental setups with numerous detector pixels and extended measurement durations.

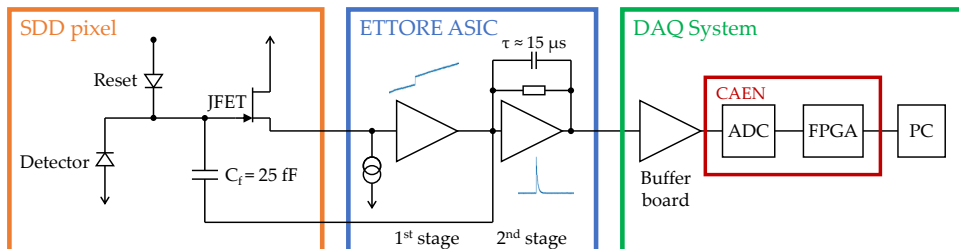


Figure 4.12: Simplified sketch of the detector readout scheme for one pixel. The first signal processing happens in the SDD and amplifies the signal (orange box). In the ETTORE ASIC (blue box), the signal is converted into the first and second stage. The DAQ and CAEN software (green box) is the last step. Figure taken from [61].

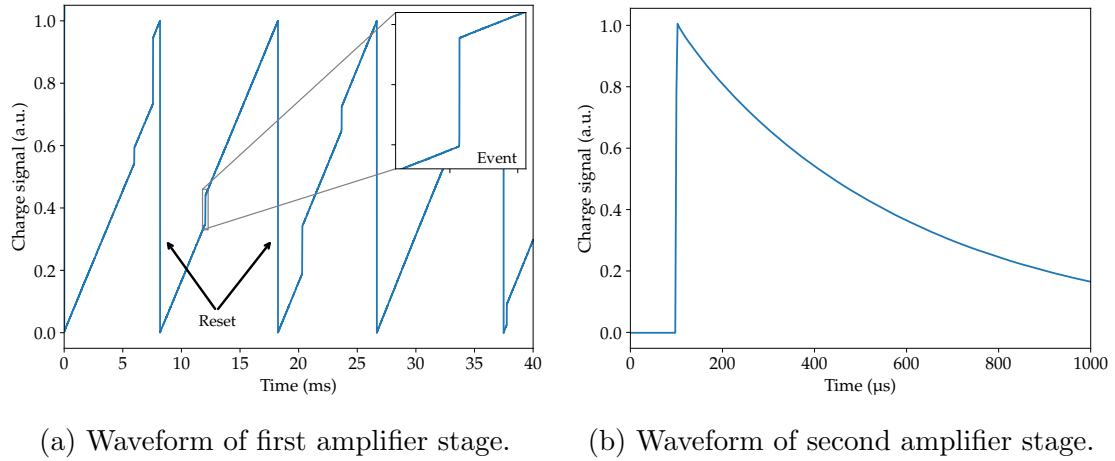


Figure 4.13: Waveform examples of the (a) first amplifier stage output and (b) second amplifier stage output. In the first stage, events can be discerned as steps in the linearly increasing ramps, as illustrated in the inset. The reset events manifest as significant steps between the ramps. In the second amplifier stage, the reset is achieved through AC coupling, producing an exponentially decaying pulse characterized by a specific time constant. Figure courtesy of F. Edzards.

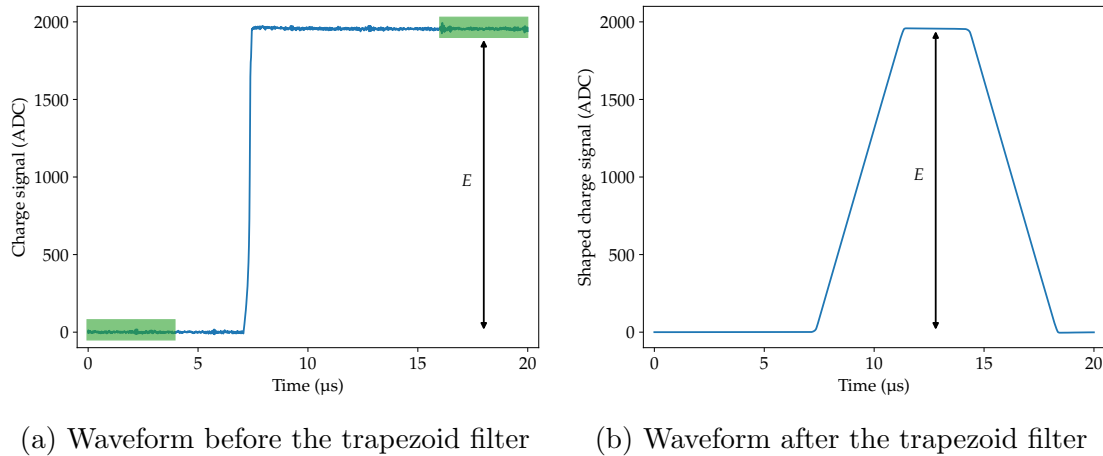


Figure 4.14: (a) The pole-zero corrected waveform is shown. The green boxes mark the average window for the filter rise time. (b) The result of a trapezoid filter is plotted. The energy can be read out at the top of the trapezoid. Figure taken from [17].

5. Detector Calibration with an LED

The calibration of the detector is critical to receive the correct energies of events. While radioactive sources offer a precise and reliable calibration method for known spectral lines, they pose challenges in implementation in specific environments or can't be turned off if necessary. On the contrary, an LED provides a simpler implementation in a setup, only being switched on when needed. An experimental setup featuring a 7-pixel TRISTAN detector and a pulsed LED was developed to assess the viability of this calibration method. Initially, a suitable LED was determined based on pulse width and resulting light amplitude and integrated into the setup. The calibration process was explored and compared with the theory after investigating detector characteristics such as energy resolution, rise time, and noise.

This chapter is structured as follows. Firstly, in section 5.1, the details of the experimental setup will be explained. Section 5.2 offers an overview of the measurements and the procedures involved. Finally, in section 5.3- 5.11, all results are presented, commencing with the LED selection, followed by an exploration of detector characteristics, and concluding with an examination of the calibration process.

5.1. Experimental Setup

The experimental setup comprises the LED, mounted on a carrier board, and a 7-pixel TRISTAN detector with corresponding readout electronics. They are placed in an aluminum box serving as a lightproof enclosure. The LED used in this setup is the laser diode ADL-65055TL [65]. It emits red light at a wavelength of $\lambda = 650$ nm, has an output power of $P = 5$ mW, and operates at a voltage of $V_{\text{op}} = 2.2$ V. Mounted on a carrier board, the LED is connected to a coaxial cable for voltage supply, incorporating a resistor of $R_{\text{LED}} = 50 \Omega$. A photograph of this setup can be seen in fig. 5.1 and a circuit diagram in fig. 5.2. This LED carrier board is positioned beneath the detector board so that the LED is aligned towards the entrance window of the 7-pixel detector housed within the aluminum box. This setup is illustrated in fig. 5.3.

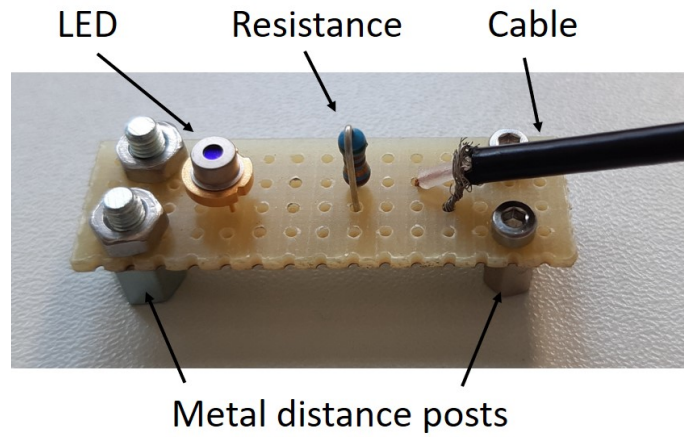


Figure 5.1: Photograph of the LED carrier board. The LED (left) is connected with a resistance (center) and a cable (right) for the voltage supply of the LED. Four metal distance posts are strategically placed at the board's edges to prevent unintentional short circuits, ensuring that components do not contact the aluminum box.

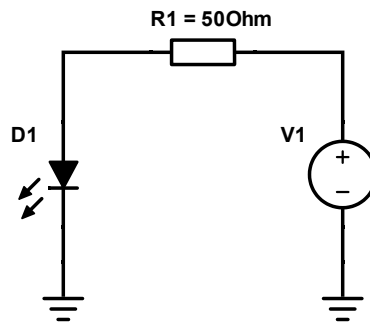


Figure 5.2: Circuit diagram of the LED carrier board. D1 described the LED, R1 is the resistance with $50\ \Omega$, and V1 is the DC power supply for the LED. Therefore, the power was varied between 2.0 V and 2.6 V

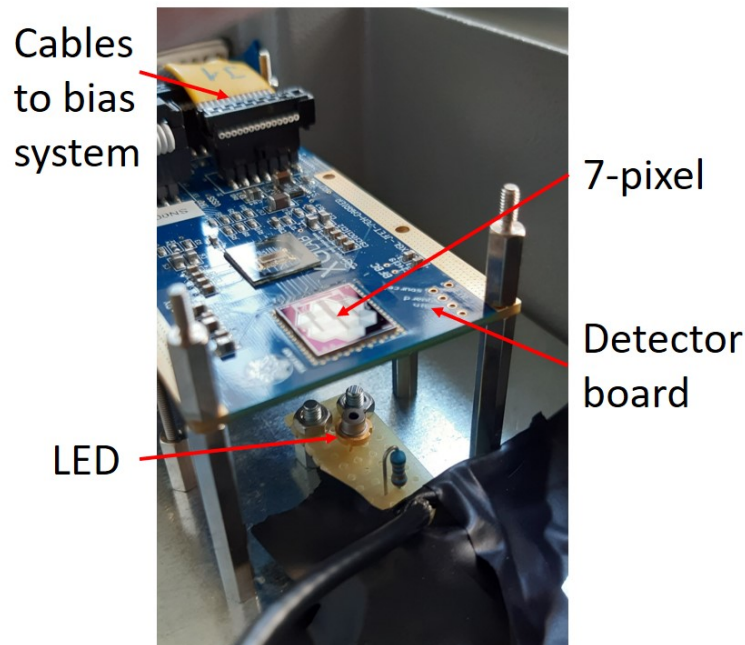


Figure 5.3: The **LED** is placed under the 7-pixel TRISTAN detector that the emitting light hits the entrance window. The cables on the top lead through a wall feed through to the bias board.

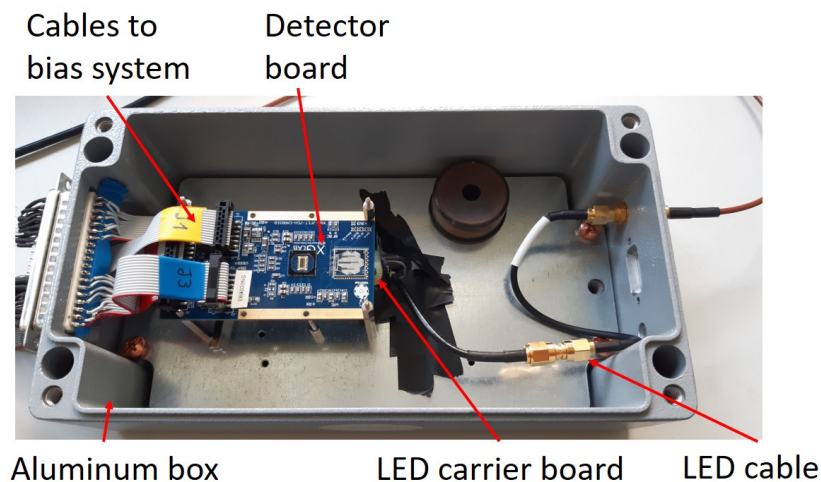


Figure 5.4: The **LED**, placed under the 7-pixel TRISTAN detector, is in a lightproof aluminum box. The cables on the left lead through a wall feed through to the bias board, and the cable for the **LED** leads to a wall feed through on the right side.

The fully assembled experimental setup is shown from a top view in fig. 5.4. On the left side, a wall feed-through is implemented for the detector cables, leading to the bias board, while on the right side, a separate wall feed-through is established for the **LED** cable. The entire box is sealed to ensure its lightproof integrity. Otherwise, light would produce many background events in the detector. The complete setup is shown in fig. 5.5. The **LED** is used in a pulsed mode for the measurements. The pulse allows individual adjustment of parameters such as frequency, operating voltage, and

pulse width.

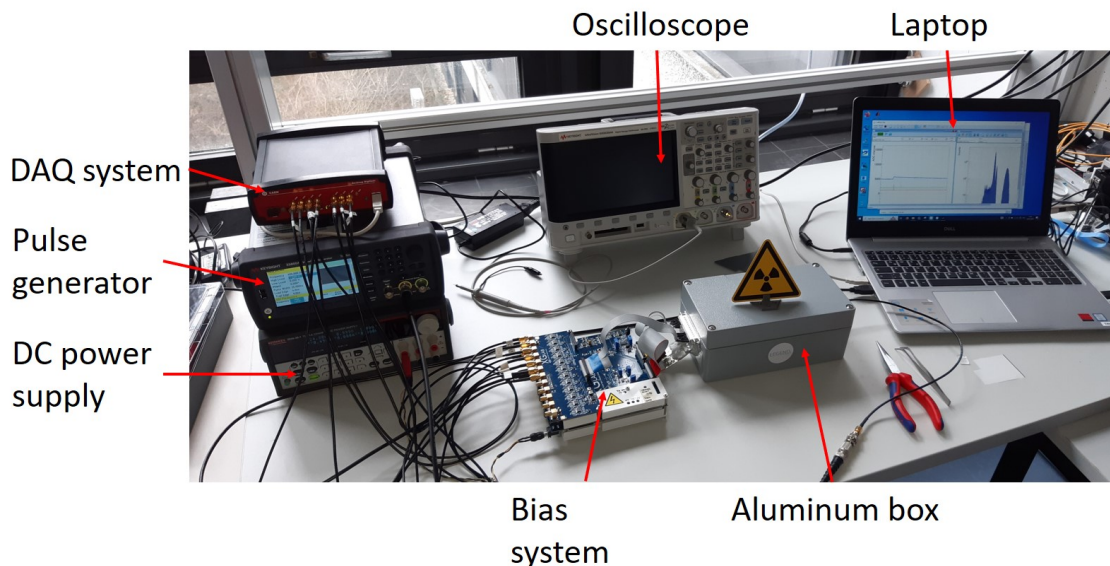


Figure 5.5: Photograph of the complete LED calibration setup. Positioned on the left, the DAQ (CAEN DT5725S) system is situated at the top, followed by the pulser (Keysight 33600A) for the LED and a DC power supply (KEITHLEY 2230G-30-3) for the detector system below. Adjacent to it are the bias system board and an aluminum box housing the 7-pixel TRISTAN detector and the LED. An oscilloscope is positioned above for setup verification. On the right side, a laptop with the CoMPASS software is used for detector control and data acquisition.

5.2. Measurement Overview

This section provides an overview of the measurement procedure. At the beginning of each measurement, the initial step involves setting all detector voltages at the designated test points on the control board. The specific values utilized for this purpose are listed in tab. 1. The operating detector parameter must be the same in each measurement, as these voltages significantly influence the overall performance of the detector. The function of each voltage is explained in section 4.3.

Table 1: Values for the operating voltages at the bias board were taken. Before every measurement, these values were set.

Probing point	Voltage (V)	Probing point	Voltage (V)
V_{SSS}	-6.5	R1	-8.0
V_D	+6.6	RX	-120.0
V_{ResH}	+4.0	BC	-100.0
V_{ResL}	-10.0	BF	-110.0
IGR	-18.5		

Before a measurement is performed, all pulse settings for the LED will be configured. A detailed overview of all the parameters used will be explained later. Finally, a ^{55}Fe source is positioned beside the LED, enabling energy calibration. So the LED and ^{55}Fe were measured parallel.

Performed measurements

The detector typically recorded pulsed events from the LED. Overall, two measurement campaigns were performed. The first campaign involved one listmode and one listwave mode measurement. In listmode, only the already-reconstructed energy and timestamp are stored, while in listwave mode, the waveform of the second stage is additionally available. This provides more information but increases the amount of data stored enormously. This measurement was performed simultaneously with the ^{55}Fe source. To gather information about the pulses generated by the pulser, a signal splitter was interposed between the LED and recorded with the DAQ. An overview of all measurement parameters for campaign 1 is provided in tab. 2.

Table 2: Overview over all measurement parameter in campaign 1 for measuring pulsed events from the LED.

	Measurement 1	Measurement 2
General settings		
Acquisition mode	Listmode	Listwave
Measure time	1 h	5 min
Measured pixels	All 7	All 7
Trigger (pulser)	Yes	Yes
LED settings		
Frequency	400 Hz	400 Hz
High level voltage	2.3 V	2.3 V
Low level voltage	0 V	0 V
Pulse width	20 ns	20 ns
Leading/Tail edge	4.0 ns	4.0 ns

The data analysis from campaign 1 revealed the need for additional measurements. It turns out that the width of the LED peak depends on the energy of the peak, which can be moved by varying the high-level voltages for the LED, leading to an energy scan with varying high-level voltages for the LED. Furthermore, a long-term measurement was essential to assess the LED's stability over an extended period. Consequently, an initial measurement was conducted to ensure proper functioning. The subsequent measurements included an energy scan with different high-level voltages, a long-term measurement in listwave mode, and a final listmode measurement to verify the constancy of the detector and calibration. The most important parameters for the DAQ are listed in tab. 4.

Table 3: Overview over all measurement parameter in campaign 2 for measuring pulsed events from the LED.

	Measurement 1	Measurement 2	Measurement 3	Measurement 4
General settings				
Acquisition mode	Listmode	Listmode	Listwave	Listmode
Measure time	10 min	10 min	12 h	10 min
Measured pixels	All 7	All 7	Ch 0	All 7
Trigger (pulser)	Yes	No	No	Yes
LED settings				
Frequency	400 Hz	400 Hz	10 Hz	400 Hz
High level voltage	2.4 V	2.0 V - 2.6 V	2.2 V	2.4 V
Low level voltage	0 V	0 V	0 V	0 V
Pulse width	20 ns	20 ns	20 ns	20 ns
Leading/Tail edge	4.0 ns	4.0 ns	4.0 ns	4.0 ns

Table 4: Overview of the most important DAQ parameters.

Parameter	Value	Parameter	Value
Trap rise time	2 μ s	Reset period	2 ms
Trap flat-top	0.192 μ s	Reset pulse width	5 μ s
Fast discr. smoothing	64 samples	Record length (wave)	9984 ns
Input rise time	96 ns	Pre-trigger (wave)	4000 ns
Trigger holdoff	192 ns		

5.3. LED Selection

Before measurements with an LED can be performed, a suitable LED is crucial. Therefore, five different LEDs have been tested in terms of light yield and signal rise time. Their physical properties can be found in tab. 5. A setup similar to the one depicted in fig. 5.1 was constructed to conduct the tests. The light of the LEDs is captured in a photodiode BPX 65 ([66]), and the electrical signal is measured and recorded with an oscilloscope.

Table 5: Overview over all **LED**s. 650 nm corresponds to an energy of 1.9 eV. "Op." stands for "operating".

	Model	Type	λ (nm)	P (mW)	Op. Voltage (V)
LED 1 [67]	ADL-65055TL	Laser diode	650	5	2.2
LED 2 [68]	CSL0701DT5	LED	605	120	2.1
LED 3 [69]	NSPB300B	LED	450	123	3.2
LED 4 [70]	NSPR310S-RP-S-T	LED	650	122	2.1
LED 5 [71]	WP7113LSECK/J3	LED	625	84	1.8

First, each **LED** was tested independently at different voltages, current, and pulse width parameters to get a general overview of its response. It turned out that the operating voltage, stated by the manufacturer, could be significantly exceeded due to the very short pulses. After each **LED** proved to be functional, a systematic measurement was then performed, where a pulse width of 20 ns and an operating voltage of 5 V were set for each **LED**. The light signal in the photodiode of this measurement can be seen in fig. 5.6. As evident in fig. 5.6, **LED** 1 stands out as the most favorable candidate, exhibiting the highest signal amplitude and rise time. Two crucial characteristics of the measurements are the ability to generate very short pulses while still producing sufficient detectable photons. **LED** 2 emerges as the second most suitable option but lags with a lower amplitude by a factor of 6 and a significantly shorter rise time. The remaining three **LED**s prove unsuitable for measurements with such a small pulse width. As a result of this, it was a simple decision to choose the **LED** 1 with the model number ADL-65055TL for all future measurements.

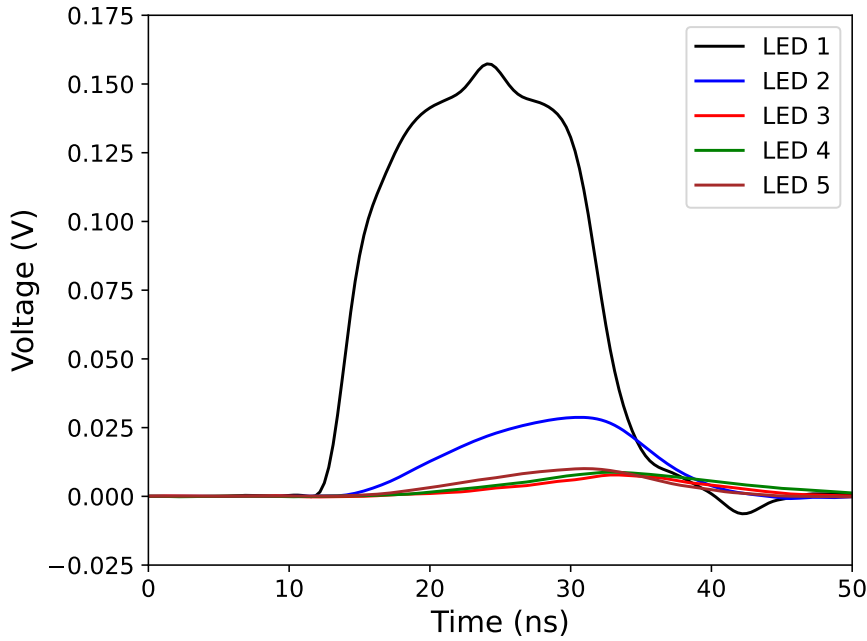


Figure 5.6: Comparison of all LEDs. The voltage on the Y axis describes the voltage measured in the photodiode, which is proportional to the intensity of the light. The measurement was performed with a pulse width of 20 ns and an operating voltage of 5 V. An explanation of the correspondence between the LEDs and their labels is shown in tab. 5. LED 1 is the most suitable candidate due to its fast rise time and high amplitude.

5.4. Observed Energy Spectrum

Utilizing the experimental setup detailed in subsection 5.1 with the selected LED 1 from the preceding section, measurements following the measurement procedures outlined in 5.2 were conducted. Firstly, an initial energy spectrum was obtained, as depicted in fig. 5.7. For simplicity, the spectrum for only one pixel (NE) is presented.

The spectral region from 600 to 1700 lsb corresponds to the ^{55}Fe source. In the energy range of 3500 to 4500 lsb, the spectrum is attributed to the pulsed LED. It exhibits a Gaussian-like shape, although a "shoulder" is noticeable at lower energies, indicating a slight energy loss in some events. The origin of this phenomenon remains unexplained and is still under investigation. The minor peak at 5000 lsb represents pile-up events from ^{55}Fe and LED events. Notably, the LED peak appears broader than the ^{55}Fe source. This discrepancy is attributed to the production of e-h pairs, a phenomenon elaborated in the following.

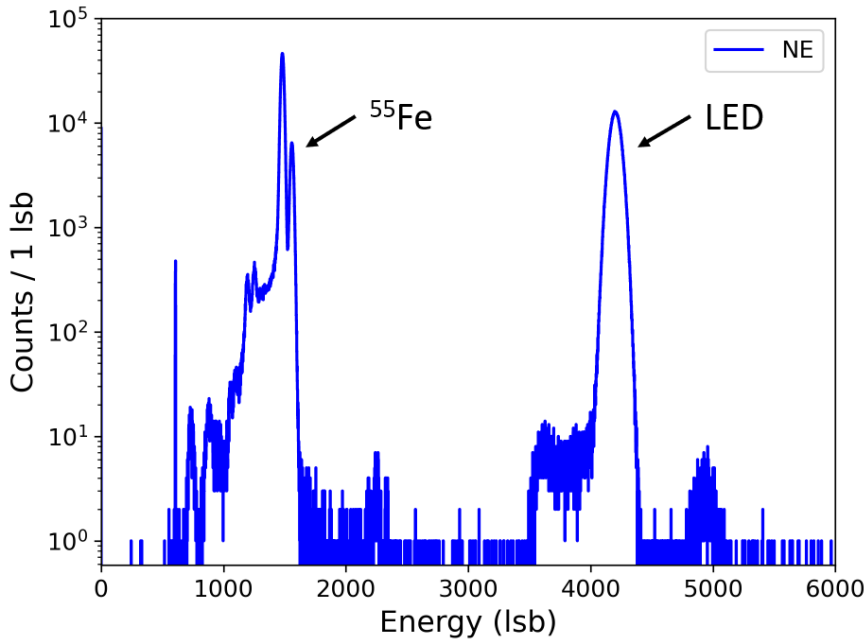


Figure 5.7: Measured energy spectrum from the listmode data from campaign 1. The left section from 800 – 1500 lsb represents the spectrum from a ^{55}Fe source, while the peak in the center from 3500 – 4500 lsb is attributed to the LED.

The fundamental difference between an X-ray and a photon emitted by a LED lies in their energy levels. X-rays typically possess energies in the keV range, while photons from LEDs operate in the eV range, considerably lower. When an X-ray interacts with a detector material, its energy is sufficiently high to generate an energetic electron via the photo effect. This electron scatters within the detector material, creating many e-h pairs on its path. As described in section 4.3, on average 3.6 eV of energy are necessary to generate one e-h pair. Here, 1.1 eV is used to overcome the band gap, and with the remaining 2.52 eV phonons, a form of heat, will be produced and can't be detected. The number of e-h pairs produced by one X-ray is given by eq. (17). As explained in section 4.3, the fluctuations in the generated e-h pairs are correlated with the Fano factor F , see eq. (18). Since this Fano factor is 0.115, the energy resolution σ_{Fano} becomes significantly smaller, see eq. (19). This process is shown in fig. 5.8a.

On the other hand, low-energy photons, like those from an LED, exhibit a different behavior. The energy of a photon E_{ph} can be calculated with the following equation:

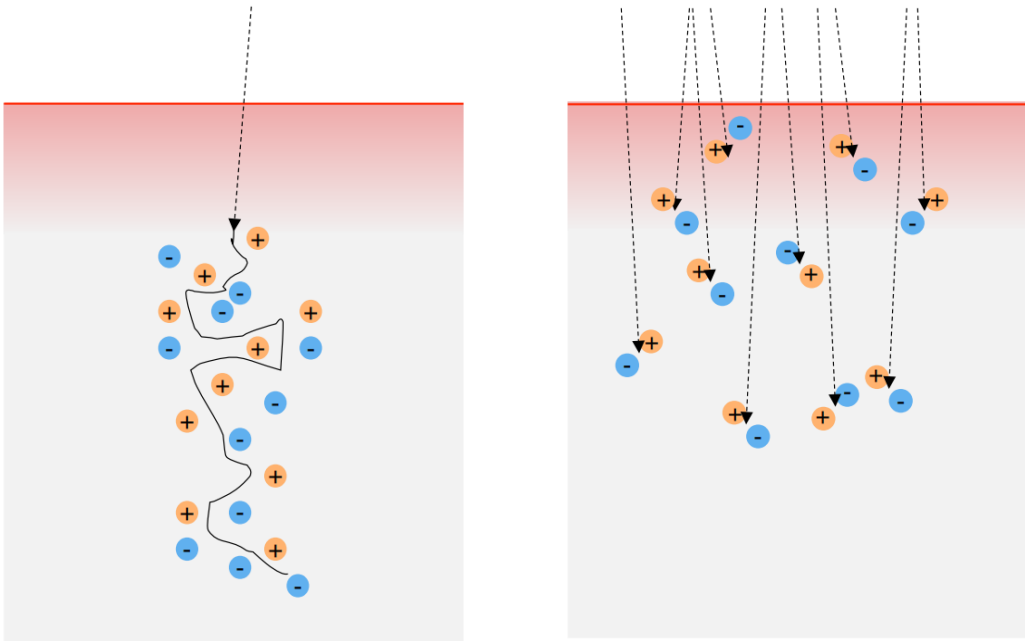
$$E_{\text{ph}} = \frac{hc}{\lambda}, \quad (22)$$

where h is the Planck constant, c the speed of light and λ the wavelength. A wavelength of 650 nm corresponds to an energy of 1.9 eV. This energy is only sufficient enough to produce exactly one e-h pair per photon. The remaining 0.8 eV

are not enough to excite a second **e-h pair** and are transferred to the detector via phonons. If the energy of a photon is smaller than the band gap, no **e-h pair** would be generated. Therefore, **SDDs** are sensitive to light with a wavelength $\lambda < 1130$ nm. So, in the case of **LED** photons, no Fano factor is involved since one photon precisely produces one e-h pair. The fluctuation in generated **e-h pairs** depends only on the fluctuation of incoming photons. Given that the number of photons produced by the **LED** follows a Poisson distribution, corresponding to a Gaussian distribution for many photons, the e-h pair production is also Gaussian. This process is visually depicted in fig. 5.8b. Eq. (19) changes then into:

$$\sigma_{\text{LED}}^2 = E \cdot \varepsilon. \quad (23)$$

The charge cloud is generated across the entire pixel since the **LED** illuminated the entire detector. In contrast, the charge cloud of an X-ray is created in a small region of the detector.



(a) Production mechanism of **e-h pairs** with an X-ray.

(b) Production mechanism of **e-h pairs** with an **LED**.

Figure 5.8: (a) The production mechanism of **e-h pairs** from X-rays. They possess sufficient energy to generate numerous **e-h pairs** per incoming X-ray. (b) The production mechanism of **e-h pairs** from an **LED**. Each photon produced by the **LED** carries just enough energy to create one **e-h pairs** pair. Figure courtesy of K. Urban.

5.5. Energy Calibration with ^{55}Fe

The two lines of the ^{55}Fe spectrum are used to calibrate the detector. The spectrum is presented on the left side of fig. 5.7, comprising two distinct peaks. The primary

peak corresponds to the K_α peak with an energy of 5.9 keV, while the second peak represents the K_β peak with an energy of 6.49 keV. Gaussian fits are applied to these peaks to extract their amplitude, width, and mean values, as illustrated in fig. 5.9. The calculated means and known peak positions at 5.9 keV and 6.49 keV are used to calibrate the detector from units of lsb to energy in keV. The same calibration procedure is applied to all seven pixels. The results are depicted in fig. 5.10. Notably, the peak positions of the LED vary for each pixel. This variation is attributed to the fact that each pixel is exposed to a different number of photons. Due to the off-center positioning of the LED and its non-radial cone of light, each pixel is exposed to a different number of photons. Consequently, the energy of a single LED pulse corresponds to the sum of photons reaching the pixel.

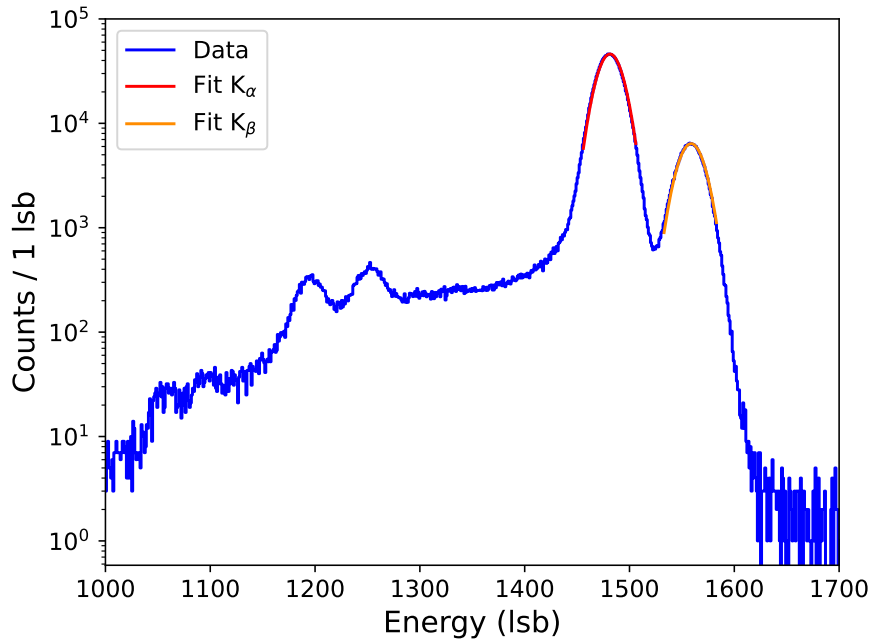


Figure 5.9: ^{55}Fe spectrum for measurements of listmode data in campaign 1. Gauss fits of the K_α peak (red) at 5.9 keV and the K_β peak (orange) at 6.49 keV were performed to allow energy calibration.

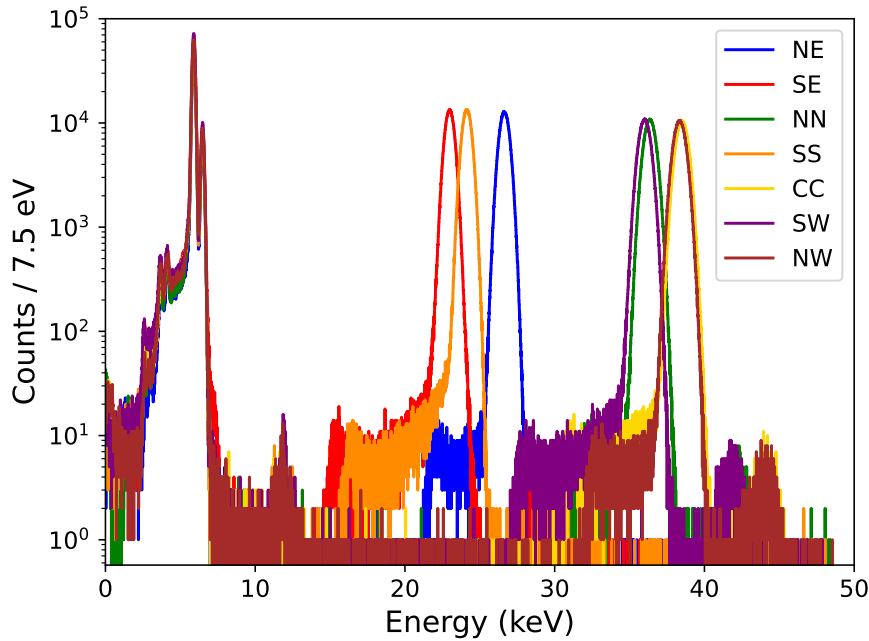


Figure 5.10: Calibrated spectra for all seven pixels. The left section from 0 – 8 keV represents the spectra from the ^{55}Fe source, while the peaks from 20 – 40 keV are attributed to the LED.

5.6. Count Rate Analysis

As described in section 5.2 the electronic signal applied to the LED has been recorded in the DAQ using a signal splitter. It serves as a trigger for the DAQ, providing additional pulse information. It serves as a valuable cross-check to ensure the agreement between the number of pulses created and detected. The energy spectrum of this trigger signal is illustrated in fig. 5.11. It exhibits a slightly broad peak. While theoretically, it should represent a single line at a specific energy, in practice, there appear to be some energetic fluctuations in the pulser. However, these are no longer considered relevant because only the number of produced pulses is of interest.

The total number of generated pulse events can be counted. However, for counting the LED events, it is essential to separate the LED spectrum from the ^{55}Fe and other background events. To achieve this separation, two boundaries were defined: one on the left side of the peak or "shoulder" at 21 keV and the other on the right side of the small pile-up peak 34 keV. These boundaries ensure that only events produced by the LED are considered. The spectrum with the set boundaries for the NE pixel is depicted in fig. 5.12. This process was repeated for every pixel. The number of detected LED events can be divided by the number of generated pulser events. This ratio is illustrated in the pixel map in fig. 5.13. The result for each pixel is consistently between 99.65 % and 99.75 %. To explain the missing ratio, it is necessary to examine the pulse frequency and reset period. The pulser frequency of 400 Hz corresponds to a time period of 2.5 ms, and the reset period is 2.0 ms with a

pulse width of $5.0 \mu\text{s}$. If both systems were perfectly in phase, every fifth pulse would occur during the reset period when the DAQ is deactivated, leading to a potential missing pulse rate of 20%. However, this scenario is unlikely since the observed ratios are higher than 99.5%. On the other hand, if both systems are completely out of phase, no pulse event would occur during a reset period, resulting in a theoretical ratio of 100%. Since the systems are not perfectly synchronized in time, a beat phenomenon could explain the observed missing ratio of approximately 0.4%. For a more detailed explanation, an in-depth investigation of the DAQ system would be required, but this goes beyond the scope of the current work. In summary, a high ratio of observed LED events to generated pulse events has been achieved, with consistently high values exceeding 99.5%. This suggests that most generated LED events are successfully detected, demonstrating the effectiveness of the measurement setup.

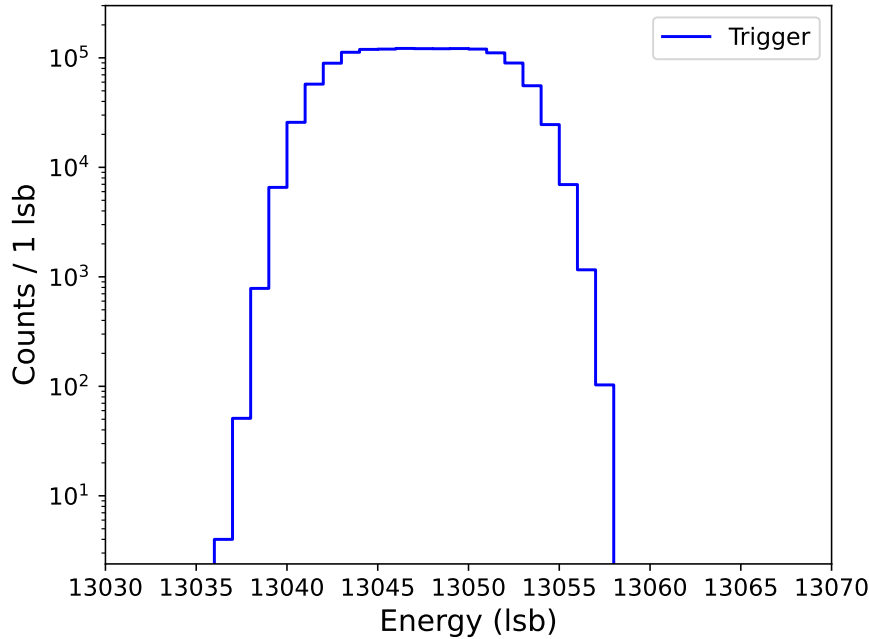


Figure 5.11: Spectrum of the trigger signal. The 8th DAQ channel was used to get a direct signal from the pulser.

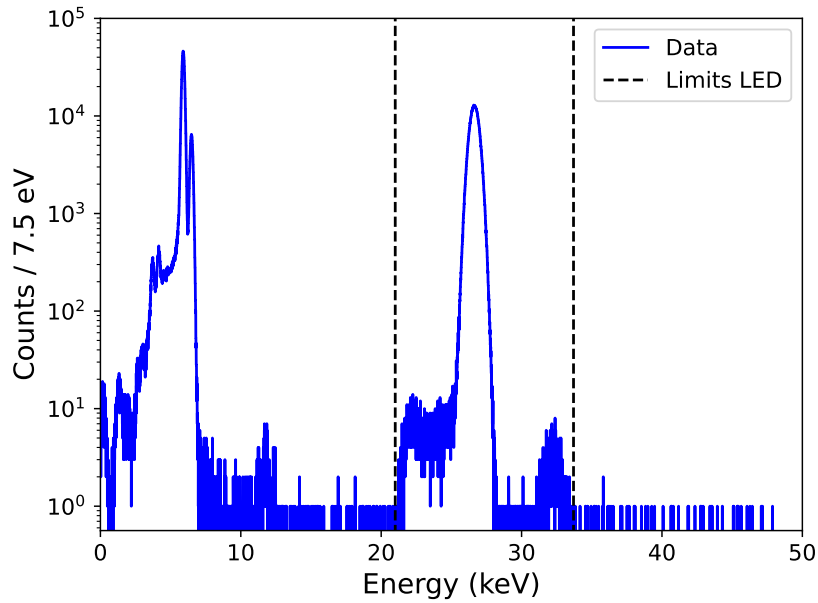


Figure 5.12: The calibrated energy spectrum for the NE pixel. Limits around the LED peak were chosen for counting the number of LED events. The boundaries are set close to the LED spectrum.

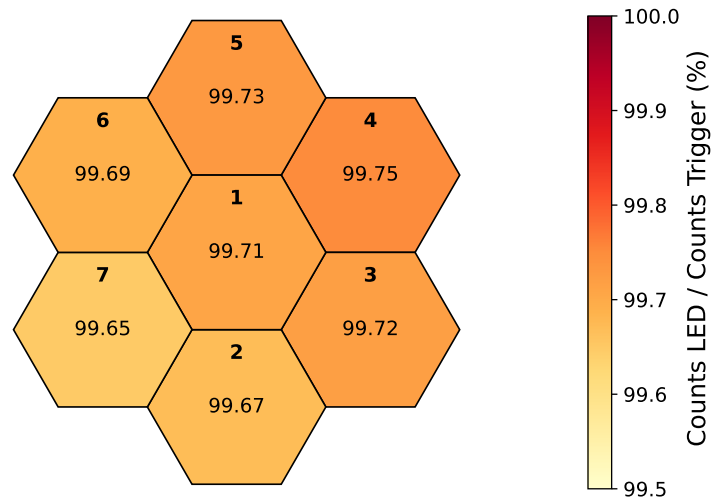


Figure 5.13: Pixel map of the ratio between the measured number of LED events and produces events by the pulser. In total, there were about $1.4 \cdot 10^6$ counts.

5.7. Energy Resolution

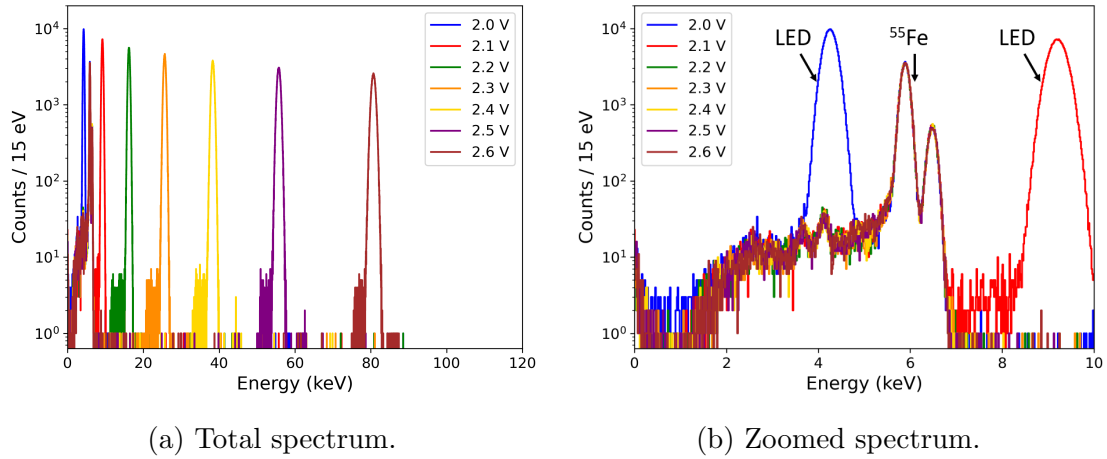
One of the crucial parameters of the detector performance is the energy resolution. Hence, a measurement was conducted by varying the high-level voltages within 2.0 – 2.6, V, as described in section 5.2. The outcome for the NN pixel is illustrated in fig. 5.14a. This particular pixel was selected due to its unique characteristic of exhibiting seven distinct LED peaks, unlike the other pixels where only five or six

peaks were observed. The spectrum of ^{55}Fe , characterized by its predominant peak at 5.9 keV, is presented in brown for the highest voltage setting. This spectrum is overlaid with all other iron spectra. Notably, the peak positions generated by the LED vary for each voltage. That is because the LED emits a different number of photons at each voltage. As described in eq. (23), the energy of the peak depends on the sum of detected photons, resulting in peak extensions across the 4 – 80 keV range.

To determine the energy resolution of ^{55}Fe , the K_α peak is fitted using a Gaussian function, and the resulting width is converted to FWHM. The outcomes are depicted as a pixel map in fig. 5.15a. All values fall within the 211 eV to 217 eV, indicating a proximity among them. For the energy resolution of the LED, the peak at a high-level voltage of 2.3 V, corresponding to an energy of about 38 keV was selected for every pixel. The FWHM was calculated using the same procedure employed for ^{55}Fe . The FWHM ranges from a minimum of 753 eV to a maximum of 1087 eV and is shown in fig. 5.15b. Since the energy resolution depends on the measured energy, no meaningful comparison between them is possible, see eq. (19). Instead, the energy resolution of the LED peaks must also be calculated at 5.9 keV, corresponding to the K_α peak of ^{55}Fe . Given the challenges associated with achieving a LED peak exactly at this position, analyzing the existing measurement with the energy scan proves more practical. As depicted in fig. 5.14a, the width of the LED peak increases with higher voltages, corresponding to higher energies. In fig. 5.16, the energy resolution is plotted as a function of the peak position as energy, revealing a clear upward trend. These data points can be fitted and evaluated at 5.9 keV to make a meaningful comparison between ^{55}Fe and each pixel. The chosen fit function is derived from eq. (20) and 23, as there is no Fano correlation for the LED:

$$\sigma_{\text{LED}} = \sqrt{E \cdot \varepsilon + \sigma_{\text{Noise}}^2}. \quad (24)$$

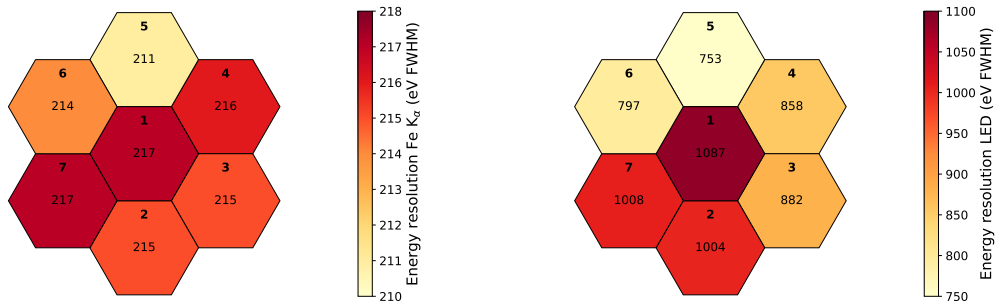
To achieve the most accurate fit, the parameters ε and σ_{Noise}^2 were left as free parameters during the fitting process. Upon evaluating the resulting fit function at 5.9 keV, the calculated energy resolution was converted to FWHM, as illustrated in fig. 5.17. The range of values only differs within a range of 13 eV, which is a plausible outcome. When compared with the average FWHM of ^{55}Fe at 215 eV, it is noteworthy that the energy resolution of the LED peak is higher by approximately 390 eV. This discrepancy can be attributed to the absence of a Fano factor in producing the e-h pairs for the LED. Assuming a σ_{Noise} of 80 eV and utilizing an energy of $E = 5.9$ keV along with $\varepsilon = 0.115$, a FWHM of 221 eV for the ^{55}Fe peak and 391 eV for the LED peak are calculated, thereby confirming the results.



(a) Total spectrum.

(b) Zoomed spectrum.

Figure 5.14: Energy scan for the NN pixel from campaign 2 for (a) the total spectrum and (b) the zoomed spectrum. The high level voltages for the LED were 2.0 – 2.6 V. Each voltage leads to another position for the LED, which generates another number of photons for each voltage. The K_{α} peak is at 5.9 keV and the K_{β} peak at 6.49 keV and is located between the first and second LED peak.

(a) Pixel map of the energy resolution of the K_{α} peak.

(b) Pixel map of the energy resolution of the LED peak at a high level voltage of 2.3 V.

Figure 5.15: (a) Pixel map of the energy resolution of the K_{α} peak. All values fall within a FWHM of 211 eV to 217 eV, indicating a proximity among them. (b) Pixel map of the energy resolution of the LED peak, measured at a high-level voltage of 2.3 V. Since each pixel is irradiated by a different number of photons the peak energy of the peak differs for each pixel, see fig. 5.10. This results in FWHM values ranging from 753 eV to 1087 eV and is significantly higher than that of the K_{α} peak because the energy resolution depends on the energy.

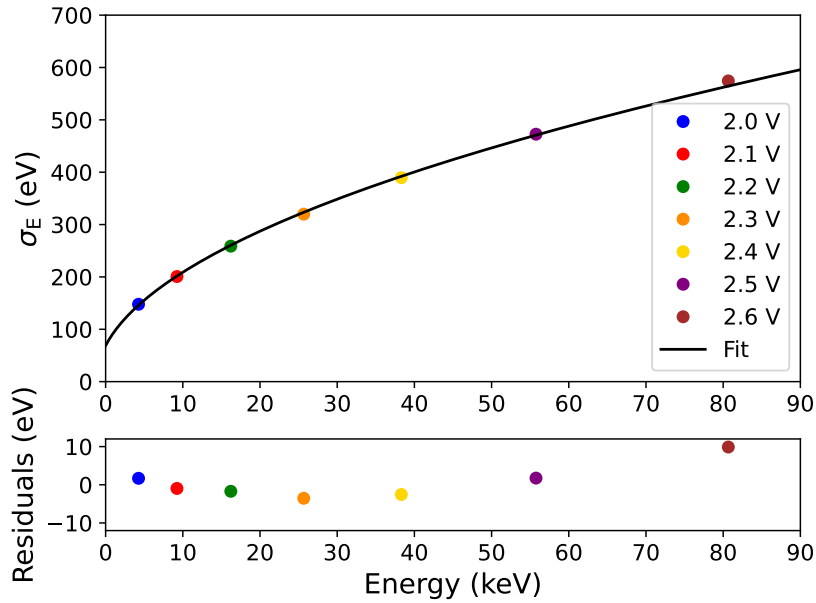


Figure 5.16: Energy resolution for different high-level voltages with fit. Firstly, there is an decreasing trend and from 25 keV an increasing trend in the residuals.

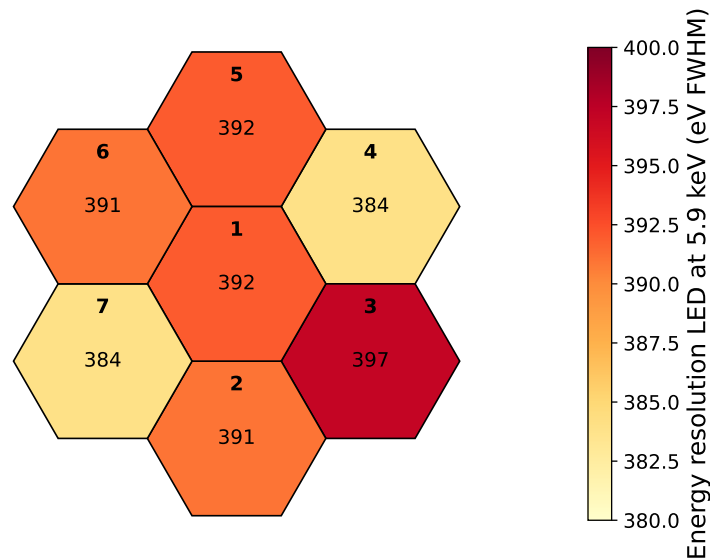


Figure 5.17: Pixel map of the energy resolution of the LED peak at 5.9 keV, given in FWHM. All values are in a range of 13 eV and are calculated with a fit to interpolate the energy resolution at 5.9 keV to be able to compare it with the K_α peak.

5.8. Comparison to Poissonian Nature

The previous results showed that the width of the LED peak depends on the energy. A clear increasing trend can be seen, especially in fig. 5.14a. The peak width can be described as σ_N or σ_E , depending on the x-axis by plotting. For σ_N , the counts are plotted as a function of the number N of produced e-h pairs in one pulse, while for σ_E , the counts are plotted as a function of the corresponding energy of the pulse.

The number of produced photons by the LED follows a Poisson distribution, which converges to a Gaussian distribution for a high number of photons, resulting in the following relation:

$$\sigma_N = \sqrt{N}. \quad (25)$$

To convert σ_N into σ_E , we utilize the parameter ε , which represents the energy required to produce a single e-h pair, refer to eq. (17). The equation gives this conversion:

$$\sigma_E = \varepsilon \cdot \sigma_N. \quad (26)$$

By substituting the expression for σ_N from equation 17, we obtain:

$$\sigma_E = \varepsilon \cdot \sigma_N = \varepsilon \cdot \sqrt{\frac{E}{\varepsilon}} = \sqrt{\varepsilon \cdot E}. \quad (27)$$

This result aligns with the general formula for the peak width, as expressed in eq. (23). So, in theory, one could calibrate the detector by measuring the peak width of the LED and calculate the resulting energy.

The measurement with the energy scan is used to investigate this effect. Fig. 5.14a already showed the resulting energy spectrum for varying the pulse voltages from 2.0 – 2.6 V for the NN pixel. After extracting the peak widths and corresponding positions, the received data can be compared with eq. (24). Three fits were performed to achieve an overview of the impact of ε and the σ_{Noise} . In the first fit, both parameters were left unconstrained. In the second fit, only ε was left as a free parameter while σ_{Noise} was fixed at 78.79 eV, a value obtained from the noise analysis. Finally, in the third fit, ε was fixed at 3.62 eV, and σ_{Noise} was allowed to vary. The outcomes of all three fit combinations for the NN pixel and the resulting parameters are illustrated in fig. 5.18.

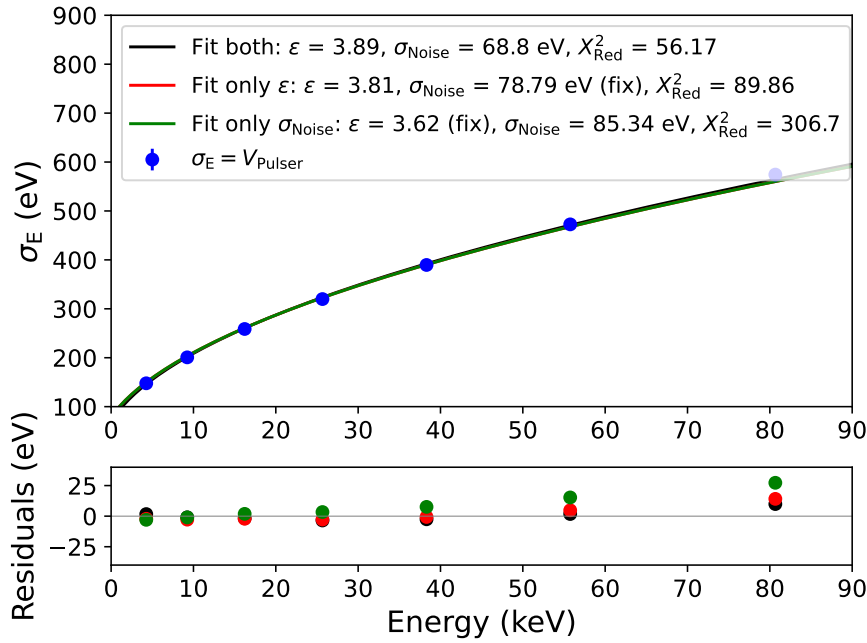


Figure 5.18: All fit combinations for comparison with Poissonian nature. The best fit is in which both parameters are free and the fit with the fixed ε is worst. The residuals increases for higher energies

Overall, the performed fits generally align with the data points with 5% accuracy yet exhibit a noticeable deviation, as evidenced in the residual plot. Particularly at higher energies, the disparity between the fit and the data points becomes more pronounced. The optimal fit, naturally, involves both parameters being free, and the fit with the fixed noise is only slightly inferior but still acceptable. However, the third fit with a fixed ε demonstrates the highest reduced χ^2 . This fixed value is noticeably smaller than the resulting values in the other fits, where it was left unconstrained. A possible explanation could be attributed to the energy calibration. The calibration, conducted using the K_α and K_β peaks at 5.9 eV and 6.49 eV, respectively, occurred at very low energies. To test this hypothesis, an energy calibration with ^{241}Am can be performed. Consequently, even a minor inaccuracy in this low-energy calibration may result in a substantial error at higher energies. If the energy scale on the x-axis is too small, it will necessitate a higher ε to ensure the correctness of the product $\varepsilon \cdot E$. Also, the measurement uncertainties further contribute to the discrepancies between the fits and the data points. The discernible structure in the residuals implies the existence of other effects that are not yet fully comprehended.

5.9. Noise Analysis

An important setting of the detector is its energy filter rise time, which directly influences the energy resolution. A noise curve is measured at different energy filter items using an ^{55}Fe source to investigate this behavior. The calculation of the noise

curve can be approached in different ways. In the following analysis, the baseline noise was used.

The existing listwave data can be utilized to perform this measurement. The area before the event itself can be used to extract the baseline value of the raw waveform data. A raw waveform data sample is presented in fig. 5.19a. The first short segment, followed by the rise caused by an event, contains the baseline data needed for the noise analysis. However, this baseline segment from 0 – 4.0 μs is too short for a comprehensive noise analysis. Therefore, baseline and PZ-correction can be applied to the waveform, as illustrated in fig. 5.19b. After removing the front part after the PZ-correction, the remaining waveform can be utilized for the noise curve analysis. Subsequently, the trapezoid filter with filter rise times ranging from 0.5 to 4.0 μs and a fixed flat-top of 0.192 μs can be applied. The energy readout was analyzed at one fixed position, resulting in a Gaussian energy distribution around zero. Finally, the noise can be determined by calculating the width of this distribution. The described procedure was separately performed for both ^{55}Fe and LED events, ensuring that events do not impact the noise curve. The ^{55}Fe and LED events can be distinguished through their energy. This analysis was conducted for each pixel, excluding the SE pixel due to anomalous spectrum characteristics. The results for ^{55}Fe are presented in fig. 5.20a, and for the LED in fig. 5.20b. The average of each pixel for ^{55}Fe and the LED is depicted in fig. 5.21. Both methods show the same noise curve, confirming the independence of the used data, as expected. The shape of the noise curve is attributed to different types of noise: Fano noise, series noise, and shot noise. Fano noise describes the statistical fluctuation of the number of e-h pairs in the charge cloud, adding a constant noise term at each filter rise time. Series noise arises because the CSA can measure the tiny charge of an event only with limited precision, increasing with lower filter rise times. Shot noise originates from the leakage current in the detector diode, introducing a random number of electrons to the charge cloud. For lower filter rise times, shot noise is less sensitive. Consequently, the noise curve exhibits a minimum at the interface where the series and shot noise reach their minimum. For the performed analysis, the minimum of about 180 eV occurs at a filter rise time of 2.0 μs , confirming this value as the optimal choice for every measurement.

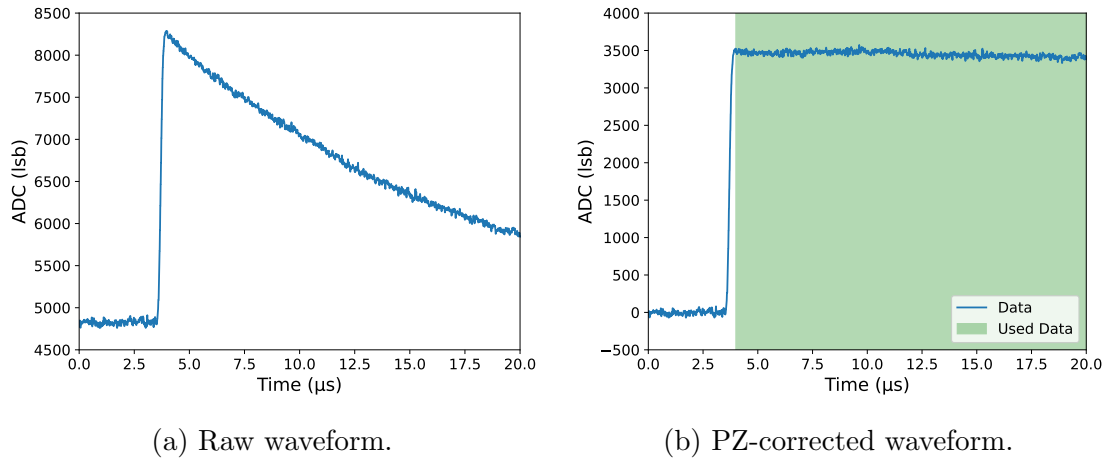


Figure 5.19: (a) A raw waveform is shown. The fast rise of the signal indicates the event, followed by an exponential decay. (b) A PZ-corrected waveform is shown. After baseline correction, the PZ filter was applied to counteract the exponential decay tail. The green-marked area was used for the noise analysis.

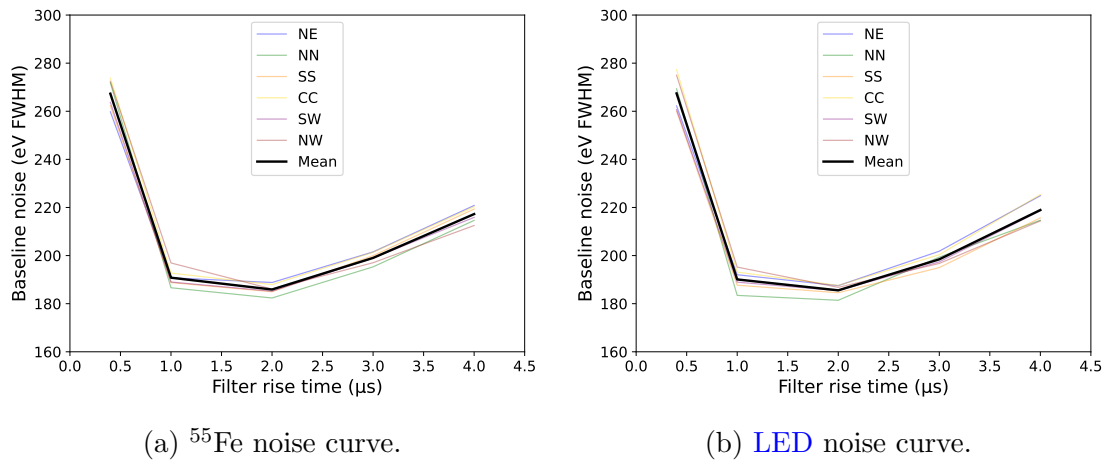


Figure 5.20: (a) Noise curve for ^{55}Fe and (b) for LED events for every pixel. The noise was calculated using baseline noise from PZ-corrected waveform data. The minimal noise can be reached with a filter rise time of 2.0 μs .

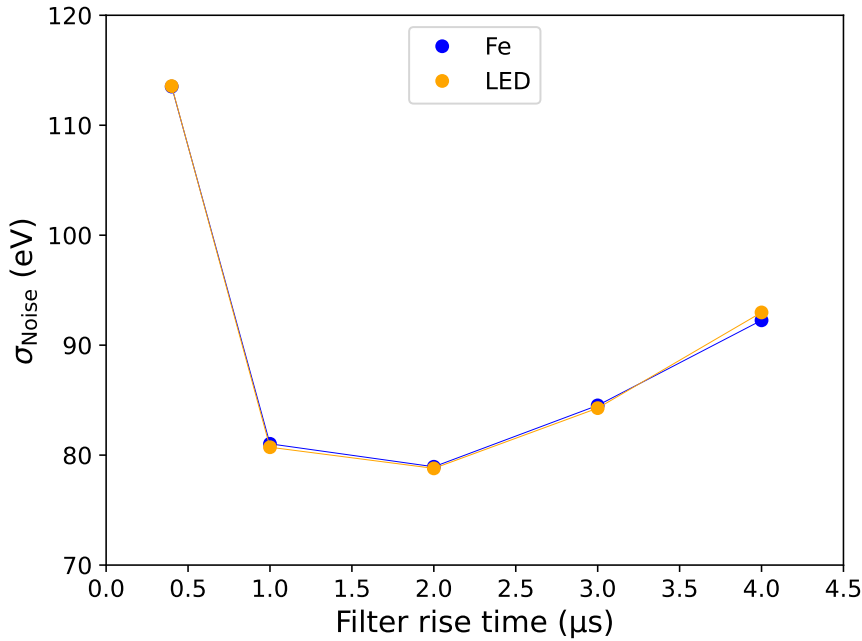


Figure 5.21: Noise curve for ^{55}Fe and LED. The noise was calculated using baseline noise from PZ-corrected waveform data. Both curves are similar, so the events do not influence the noise. The minimal noise can be reached with a filter rise time of $2.0 \mu\text{s}$.

5.10. Rise Time Analysis

Typically, the time between 10% and 90% of the signal height is being used to characterize the rise time of a detector. To investigate this, superpulses for ^{55}Fe and LED events were calculated, and their rise times were compared. Superpulses are the average of each waveform. After baseline correction, PZ-correction, and normalization of each waveform, superpulses can be obtained by averaging each waveform. This process provides a representation of the mean waveform for the analysis. The normalized superpulses for K_α and LED events are presented in fig. 5.22. The slope of the LED superpulse is flatter than the K_α superpulse, indicating that the signal takes more time to reach its maximum amplitude. The observed difference in the rise time between the LED and K_α events can be attributed to the irradiation pattern. The LED irradiates the entire pixel area, leading to the generation of e-h pairs across the entire detector area. Consequently, collecting all charge carriers at the anode takes some time, details can be found in [52]. The signal rises when the charge carriers closest to the anode arrive and concludes when those furthest from it reach it. In contrast, the charge cloud generated by a K_α event from ^{55}Fe is localized to a specific point and is much smaller than the entire detector area. This localized nature results in a faster rise time for the K_α event as the charge carriers have a shorter distance to travel to reach the anode. These differences provide an understanding of the temporal characteristics of signals generated by different radiation sources in the detector system.

To provide quantitative values, the rise times for the superpulses of ^{55}Fe events are illustrated in a pixel map in fig. 5.23a, and for LED events in fig. 5.23b. The rise times of the superpulses for the ^{55}Fe events, about 50 ns, are approximately four times shorter than those of the LED events, which have rise times of about 200 ns.

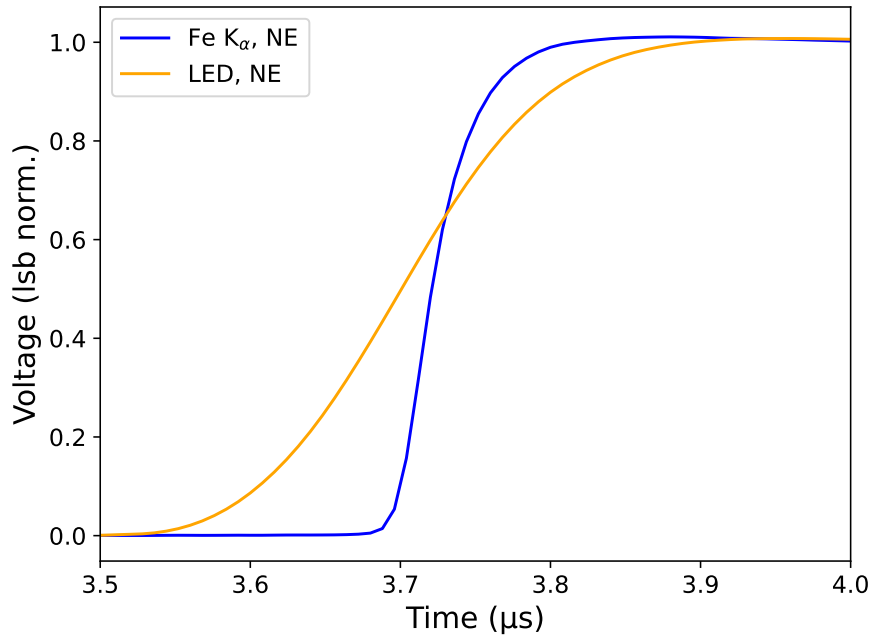
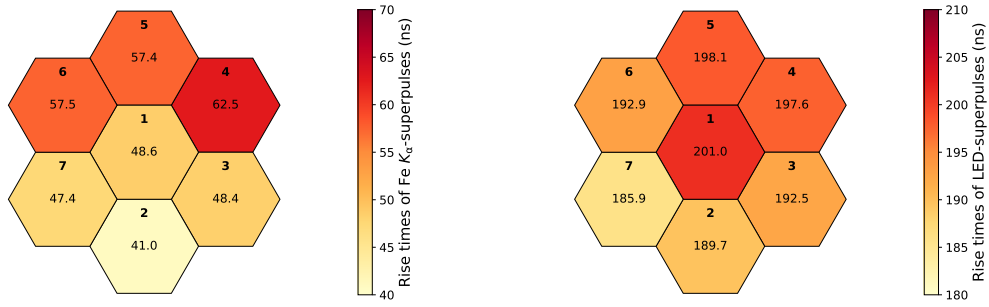


Figure 5.22: Superpulses, the average of normalized waveforms, of ^{55}Fe and LED events. The LED events have a more significant rise time because the entire pixel is irradiated. Therefore, the charge carried has to be collected from the whole pixel and sent to the anode.



(a) Pixel map of the rise times of the ^{55}Fe K_α peak of superpulses.

(b) Pixel map of the rise times of the LED peak events of superpulses.

Figure 5.23: (a) Pixel map of the rise times of the superpulses of the ^{55}Fe K_α peak. Superpulses are the average normalized waveform for each event. All values fall within a rise time of 41 ns to 62.5 ns. (b) Pixel map of the rise times of the superpulses of LED peak events. These values are significantly higher than those from the K_α peak because the LED irradiates the entire pixel area, so collecting the charge carriers at the anode takes more time.

5.11. Energy Stability

To investigate the energy stability of the LED, a long-term measurement spanning 12 hours was conducted (see tab. 3, Measurement 3). The relationship between the energy of each light pulse and time is illustrated in a 2D plot with a histogram on the right, as shown in fig. 5.24. The histogram exhibits a Gaussian shape, indicating that the energy is distributed homogeneously over the entire duration. Another option to investigate energy stability is to divide the entire measurement into equal time segments, create histograms for each segment, and compare them. The measurement is segmented into 12 one-hour intervals. The energy distribution of these runs is illustrated in fig. 5.25. If the LED exhibited energy instabilities, it would result in a drift of the histograms. However, since they all overlap precisely, no drift is observed. Overall, the LED has no discernible energy instability within this timeframe.

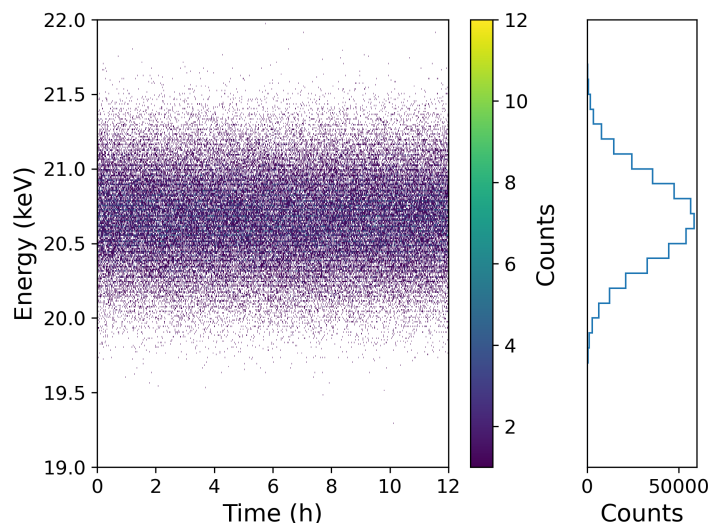


Figure 5.24: 2D histogram of a 12-hour measurement to investigate the energy stability of the LED. The energies and fluctuations are evenly distributed over the entire period. The histogram on the left side concludes with a Gaussian distribution.

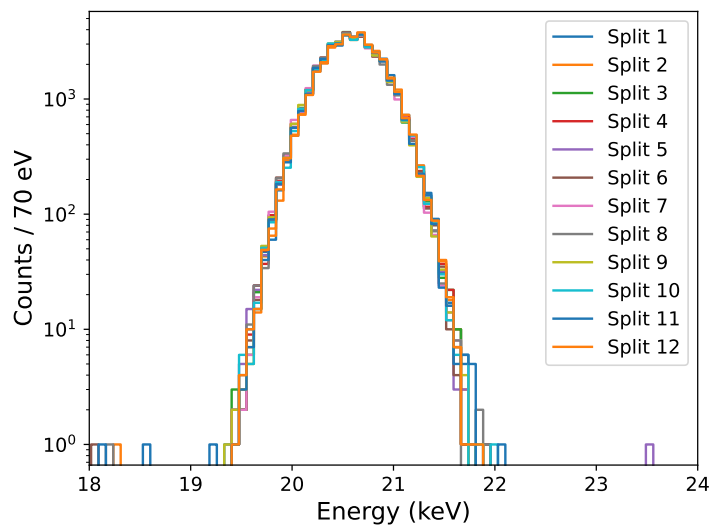


Figure 5.25: A 12-hour measurement was performed to investigate the energy stability of the LED. The measurement is segmented into 12 one-hour intervals. The histogram of all intervals is plotted over each other. All peaks have the same energy position, indicating good energy stability.

5.12. Conclusions

This measurement demonstrates the functionality of shooting an SDD detector with an LED. It is crucial to note that this setup only proves effective when the energy of the emitted photons surpasses the band gap of the detector material. The detector's characteristics can be evaluated similarly to those observed with ^{55}Fe . However, there's a notable distinction: the rise time is considerably longer, at 200 ns, compared to ^{55}Fe at 50 ns. This delay arises because the LED irradiates the entire pixel, necessitating more time to collect charge carriers from across the detector volume to the anode. Furthermore, it is observed that the width of the LED peaks correlates with their position, defined by the number of detected photons. This can be regulated by adjusting the high-level voltage of the LED. Higher voltages lead to higher LED intensity and subsequently more produced photons. Plotting the peak widths as a function of the energy position reveals an increasing trend. Detailed analysis involved exploring various fit combinations incorporating parameters like ε and noise. This measurement and analysis demonstrate the feasibility of energy calibration using LED pulses. While the current calibration method offers a certain level of precision, achieving accuracy comparable to that of a radioactive source necessitates further optimization and investigation. Potential areas for improvement include refining the energy calibration process and conducting a thorough characterization of the LED used. Nevertheless, the versatility of LEDs extends beyond energy calibration, offering potential applications in low background or dead time measurements.

6. Detector Operating Parameter Optimization

To optimize the detector performance, one crucial step is the optimization of its operating parameters, particularly the bias voltages. In this chapter, the impact of the **IGR** voltage on the performance is investigated. The **IGR** acts as a potential barrier between the anode and the **nJFET** in the pixel center. If the potential barrier is not high enough, a fraction of the charges may bypass it. In this case, they are not drifting to the anode but directly to the **nJFET**. This reduces the charge collection efficiency and distorts the detector response. In the scope of this work, a dedicated experimental setup was used to optimize the **IGR** voltage. More specifically, the **IGR** region of one pixel of a 7-pixel prototype detector was scanned with a pulsed **LED**. This approach was used to quantify the charge loss for different **IGR** voltages.

This chapter is structured as follows: First, in section 6.1, the experimental setup will be described, followed by a detailed explanation of the optimization process of the beam spot of the pulsed **LED** in section 6.2. Section 6.3 gives an overview of the measurement procedure. Finally, section 6.5 discusses the measurement results.

6.1. Experimental Setup

The experimental setup consists of a 7-pixel TRISTAN detector, a movable X-Y-Z stage, and a pulsed **LED**. All components are assembled in a light-tight enclosure, as shown in fig. 6.1. The 7-pixel detector is mounted in a cooper holding structure. The movable X-Y-Z stage is used to scan over the detector entrance window with the light provided by a pulsed **LED**. The light is coupled into a fiber and focused using a collimating lens (CFC2-A) using an adapter (SM05PT [72]) adapter above to be able to fix the fiber at the X-Y-Z stage. The scheme in fig. 6.2 illustrates how the **LED** irradiates the detector surface, and fig. 6.3 shows a photograph of the entire setup, including the bias and **DAQ** system.

To conduct a detector characterization, such as the one discussed in chapter 5.7- 5.10, a measurement with an ^{55}Fe source was conducted. For this purpose, the X-Y-Z stage was disassembled, and the ^{55}Fe source was positioned above the detector entrance window using a custom-designed holding structure, see fig. 6.4.

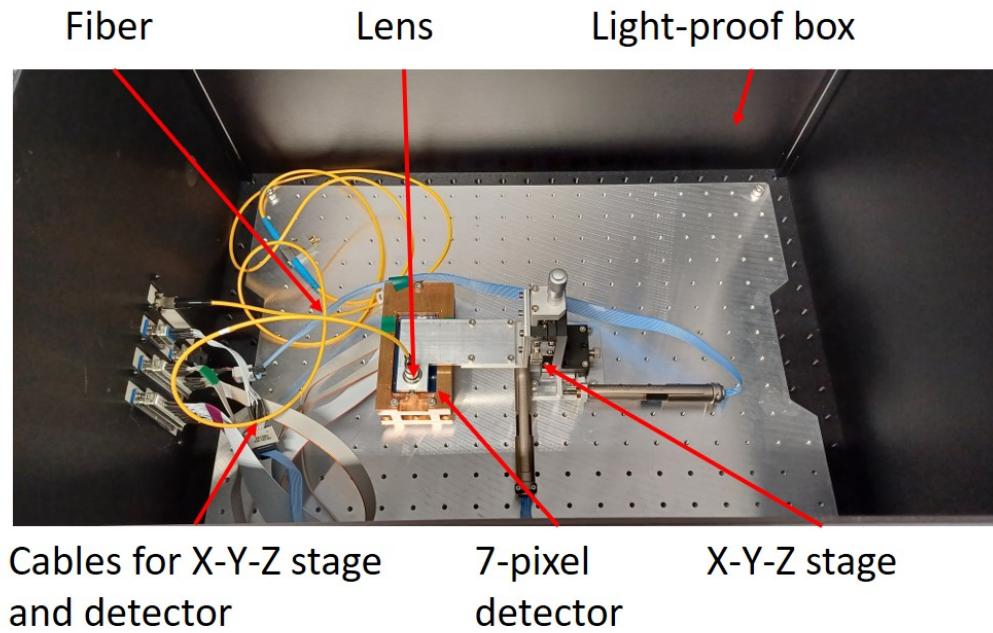


Figure 6.1: A photograph showing the IGR setup. All components are assembled in a light-proof box. The X-Y-Z stage is mounted in the center, precisely guiding the light from the fiber to the entrance window of the 7-pixel detector.

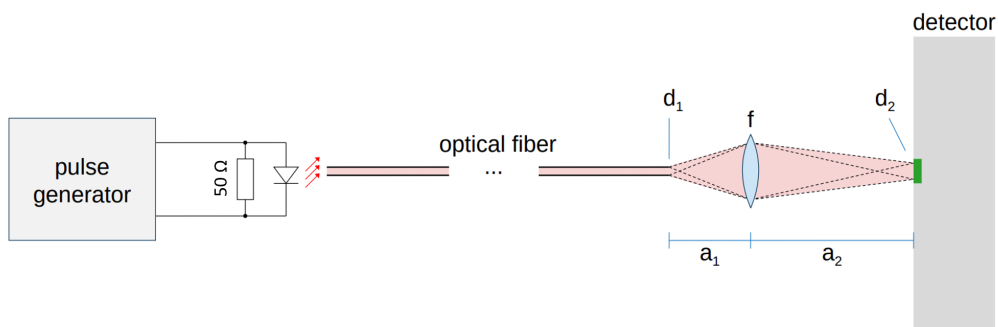


Figure 6.2: Scheme of the IGR setup. A pulse generator is used to generate a pulsed LED light beam. The light is transmitted via an optical fiber. A lens is used to focus the light, ensuring that the detector intercepts the minimal beam spot. The distance from the output of the fiber with size d_1 to the focus point f is described by a_1 , and from f to the detector surface with the beam spot size d_2 is described by a_2 . Figure courtesy of K. Urban.

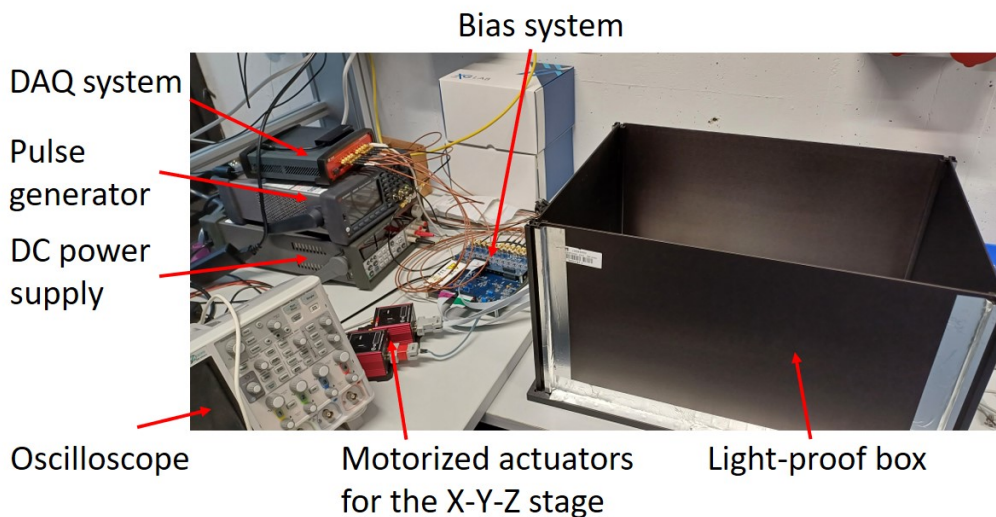


Figure 6.3: A photograph showing the entire setup for the IGR voltage optimization. The detector is mounted in the light-proof box on the right-hand side, while the pulse generator, biasing and DAQ system can be seen on the left-hand side.

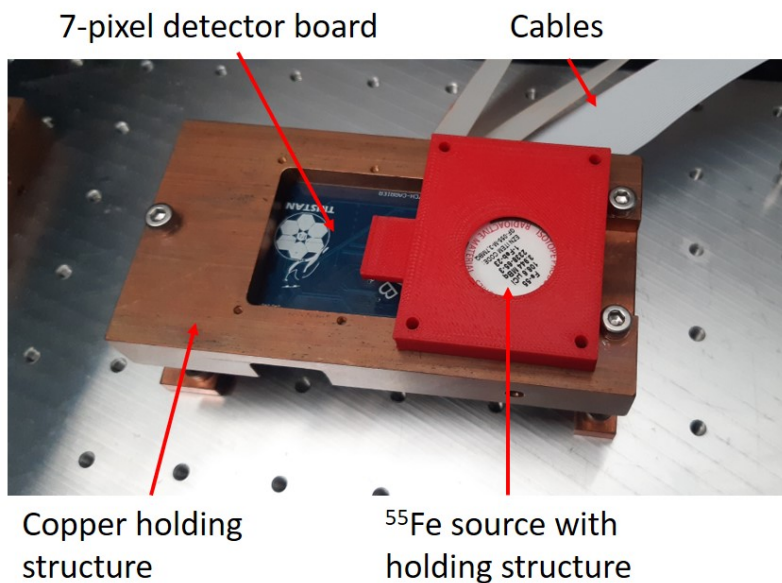


Figure 6.4: Photograph showing the ^{55}Fe calibration source above the entrance window of the detector. The detector board (blue) is mounted on the copper holding structure (brown).

6.2. Optimization of the Beam Spot Width

To be capable of investigating the detector response at a specific position, the LED light beam needs to be focused. For this purpose, a lens (CFC2-A) is at the end of the optical fiber. It is connected to the X-Y-Z stage using a thread at the fiber's end. The fiber is screwed from the top side into the X-Y-Z stage, and the light in

the focus point radiates directly on the **Charge-Coupled Device (CCD)** chip of a webcam to measure the beam spot size. This arrangement allows it to scan across the detector surface. For the distance of the lens to the detector to be in focus, the following must apply: $1/a_1 + 1/a_2 = 1/f$, and for the image size $d_1/a_1 = d_2/a_2$, see fig. 6.2. The distance from the output of the fiber with size $d_1 = 4.2 \mu\text{m}$ to the focus point f is described by a_1 , and from f to the detector surface with the beam spot size d_2 is described by a_2 . The pulsed **LED** light beam is directed onto the **CCD** chip of the webcam. The **CCD** is capturing the data of the **CCD** chip. A photograph of the measurement configuration with the webcam is shown in fig. 6.5.

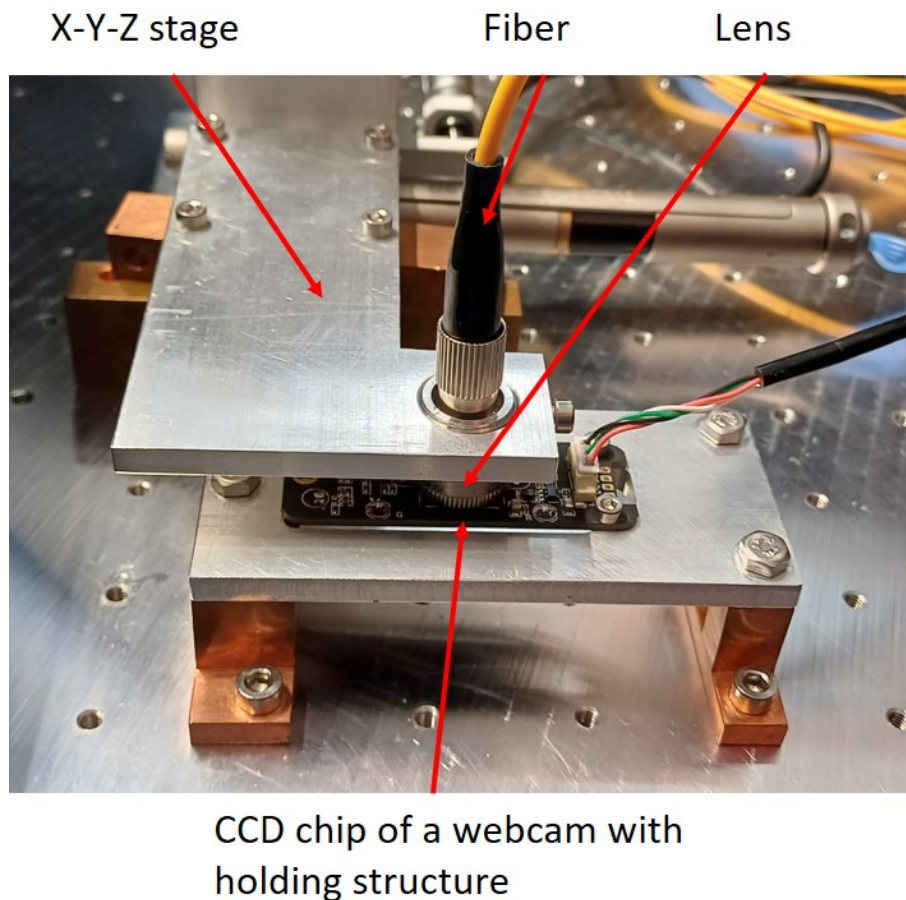


Figure 6.5: Photograph of the X-Y-Z stage, the optical fiber, and the webcam used to determine the minimal size of the beam spot. The fiber is connected to the X-Y-Z stage using an aluminum holding structure. The pulsed **LED** light beam is directed onto the **CCD** chip of the webcam.

To determine the smallest beam spot size, a systematic scan was performed by varying the Z-position. More specifically, the distance between the lens and the **CCD** chip of the webcam d_2 was varied. For each Z-position, a webcam picture was captured, and the intensity values of all pixels were stored in a separate file. An example of a beam spot picture taken with the webcam is shown in fig. 6.6.

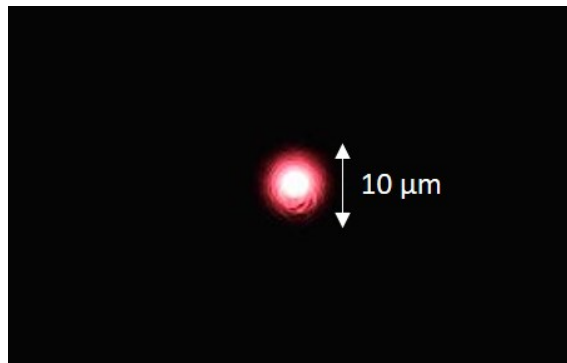


Figure 6.6: An example showing the LED beam spot recorded with the webcam. In this measurement, the distance between the lens and the CCD chip of the webcam was $Z = 5.97$ mm.

The measurement was performed automatically by varying the Z-position in 10 μm -steps. For every scanning point, the intensities of all pixels were analyzed. The beam spot was approximated with a 1D Gaussian distribution in both the X and Y directions to determine the width of the beam spot. An example of the beam spot fit is shown in fig. 6.7. The X- and Y-beam widths can then be analyzed as a function of the Z-position, as shown in fig. 6.8. A minimum value of the beam spot width of $\sigma = 8.6 \mu\text{m}$ was obtained for a distance of $Z = 5.97$ mm.

From the theoretical point of view, the optimal beam spot size can be calculated using a model consisting of two linear fits for both sides. The intersection of these linear functions then determines the beam spot with the minimum size. For the measurements performed in the scope of this thesis, the calculated minimum beam spot size is $\sigma = 7.6 \mu\text{m}$ at a Z-position of $Z = 5.99$ mm. However, taking into account that the beams and the lens are subject to effects such as divergence and aberration, the values obtained in the measurement have been used for the detector scans with the pulsed LED.

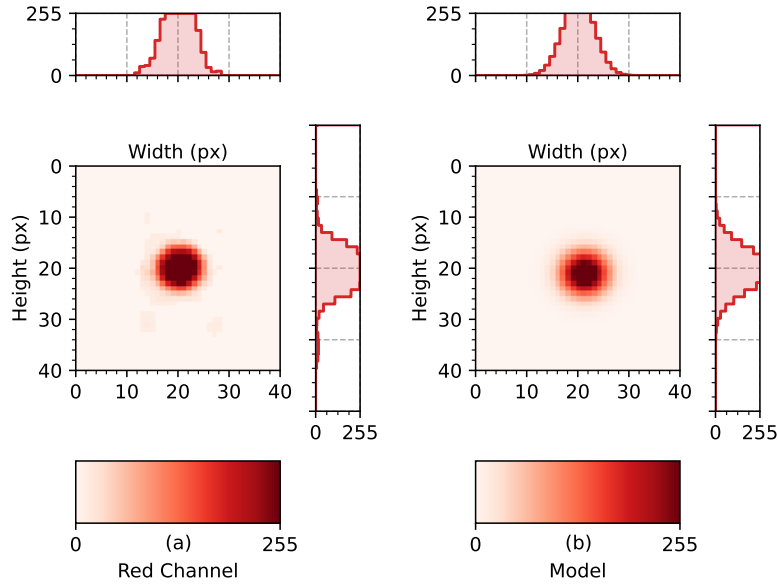


Figure 6.7: (a) Measurement and (b) fit of the LED beam spot with the webcam. The red channel corresponds to the measured intensity value.

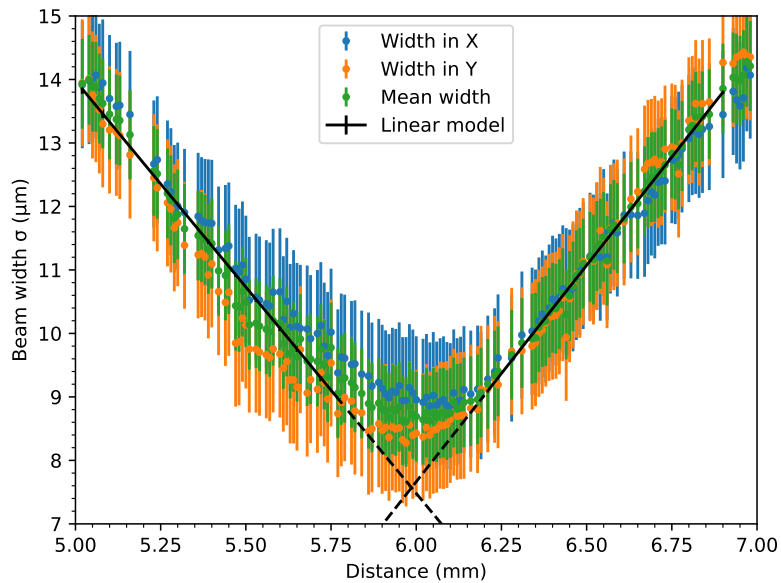


Figure 6.8: LED beam width measured with a webcam as a function of the distance between the fiber and CCD chip. The minimum beam spot size is $\sigma = 8.6 \mu\text{m}$ at a distance of $Z = 5.97 \text{ mm}$.

6.3. Measurement Overview

The IGR voltage optimization measurements were performed in three phases. 1) First, the center of the CC pixel was determined by scanning across the detector surface with the oscilloscope. Connecting neighboring pixels to the oscilloscope, a signal from the LED was observed on both pixels when crossing the boundary of adjacent pixels.

Table 6: Pulse generator settings of the LED beam for the IGR voltage optimization measurements.

Parameter	Value
Frequency	500 kHz
High level voltage	2.9 V
Low level voltage	0 V
Pulse width	50 ns
Leading/Tail edge	4.0 ns

2) In the second phase, various test measurements were performed to validate the experimental setup and working principle, including data acquisition and analysis. Initially, a single measurement position was selected to verify the functionality of the system and to optimize the pulser settings of the LED. The pulse generator settings that were finally used for the IGR voltage optimization measurements are listed in tab. 6. 3) Finally, scanning measurements using small grids were carried out to optimize the measurement settings for the IGR measurements.

The IGR voltage optimization measurements was performed such that the X-Y-Z stage was moved automatically to the different scanning positions, by scanning across the central region of the CC pixel. More specifically, a square grid with a spacing of 10 μm between the grid points was chosen. Designating the center of the CC pixel as the origin of the coordinate system, the grid spans an area of 40000 μm^2 (200x200 μm , considerably larger than the size of the IGR with an area of 2827 μm^2 (radius of 30 μm). For the selected scanning point step size of 10 μm , this results in 21 scanning points per side and, consequently, a total of 441 scanning points. Due to small drifts observed in the light intensity of the LED during the measurements, each grid was measured twice, once forward and once backward. Fortunately, the small drifts could be eliminated by averaging the data of the two measurements at each given scanning position. This scanning procedure was repeated for different IGR voltages in the range from -15 V to -25 V . Measurements between -19 V and -23 V were conducted in 0.5 V steps, while measurements outside this range were performed in 1 V steps. After completing the IGR voltage optimization measurements, additional data were collected using a ^{55}Fe source for detector calibration purposes.

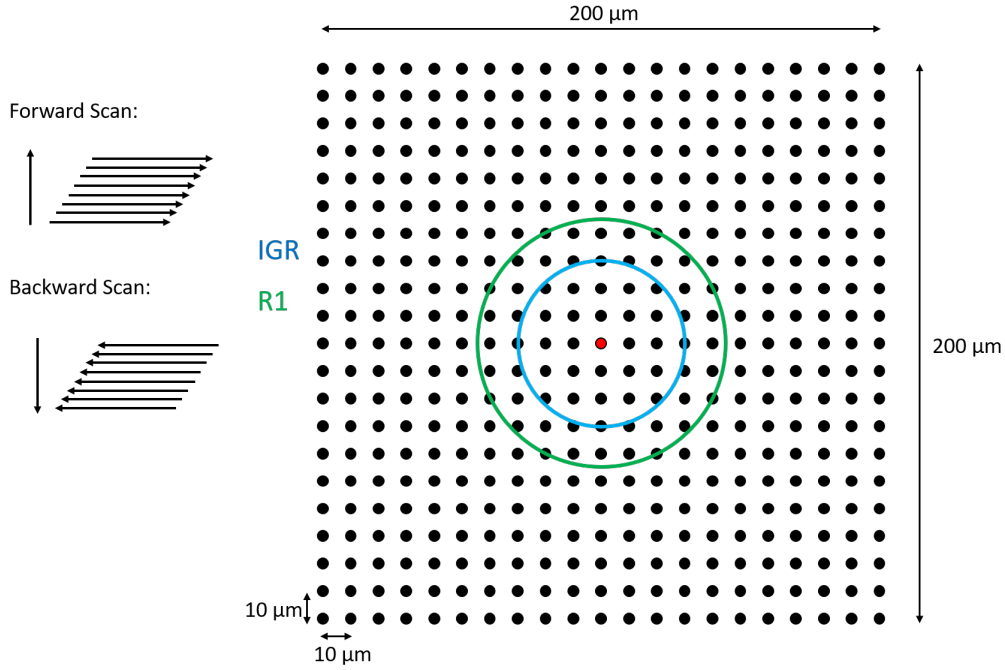


Figure 6.9: Grid for the IGR measurements. The grid spans an area of $40000 \mu\text{m}^2$ ($200 \times 200 \mu\text{m}$, considerably larger than the size of the IGR with an area of $2827 \mu\text{m}^2$ (radius of $30 \mu\text{m}$). For the selected scanning point step size of $10 \mu\text{m}$, this results in 21 scanning points per side and, consequently, a total of 441 scanning points.

6.4. Detector Characteristics

In this section, the detector is characterized using a ^{55}Fe calibration source. The detector characterization procedure was performed in a similar way as the one for the detector calibration with an LED, see section 5.7 - 5.10. The calibrated spectrum is shown in fig. 6.10, and no spectral anomalies were observed. The energy resolution of the different pixels at the K_α line is shown in the pixel map in fig. 6.11. As can be observed, except for pixel NW, a homogeneous performance in terms of energy resolution was obtained. The origin of the increased energy resolution of pixel NW is not clear. Still, it does not impact the IGR voltage optimization measurements for which pixel CC was used. Furthermore, the electronic noise, see noise curve in fig. 6.12, agrees with former measurements [61]. Fig. 6.13 shows the rise time distributions of the different pixels. It can be observed that the mode of the distribution is about 28 ns, in contrast to the 50 ns observed in the detector characterization in the section 5.10. This discrepancy can be explained by the fact that the detector used for the IGR voltage optimization measurements is from a later detector production, which included several detector design optimizations.

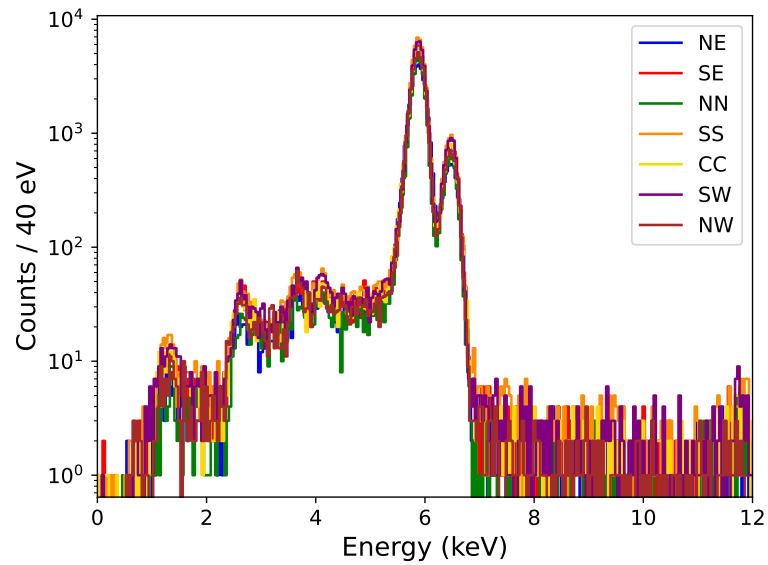


Figure 6.10: Energy spectrum measured with the 7-pixel SDD in the presence of an ^{55}Fe calibration source. The K_α peak is at 5.9 keV, while the K_β peak is at 6.45 keV.

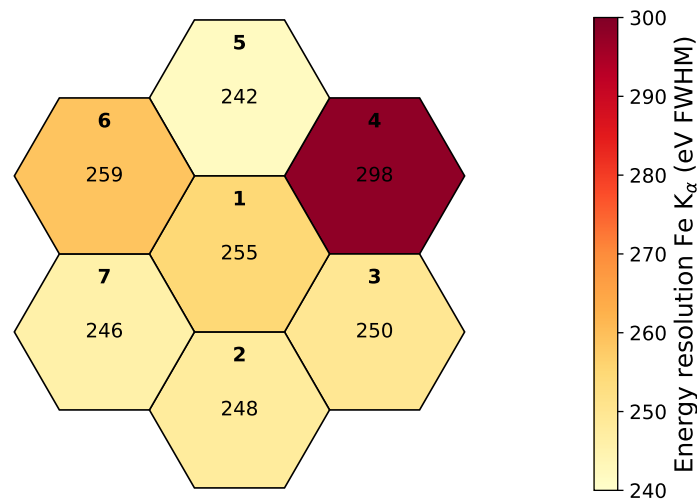


Figure 6.11: Pixel map showing the energy resolution of the K_α peak for all pixels.

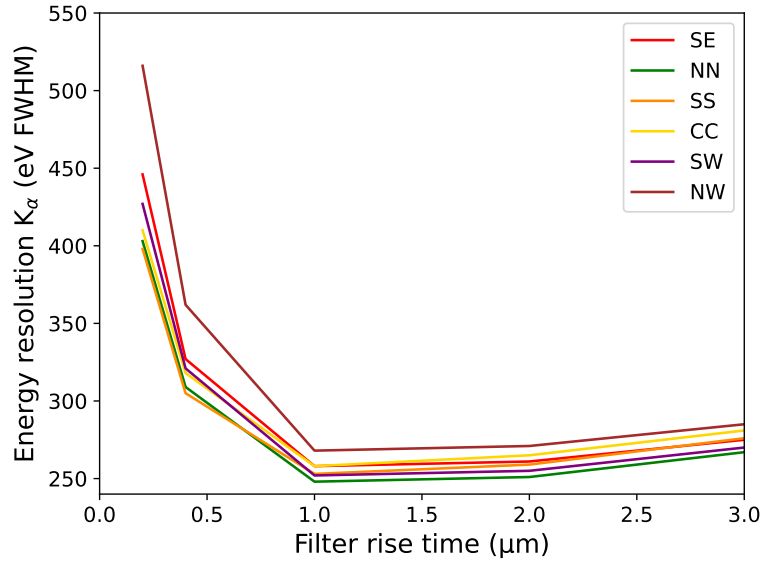


Figure 6.12: Noise curves of the 7-pixel detector. The noise has been obtained by varying the energy filter rise time and extracting the energy resolution of the K_α line. Due to non-understood features, pixel NE has been excluded from the analysis.

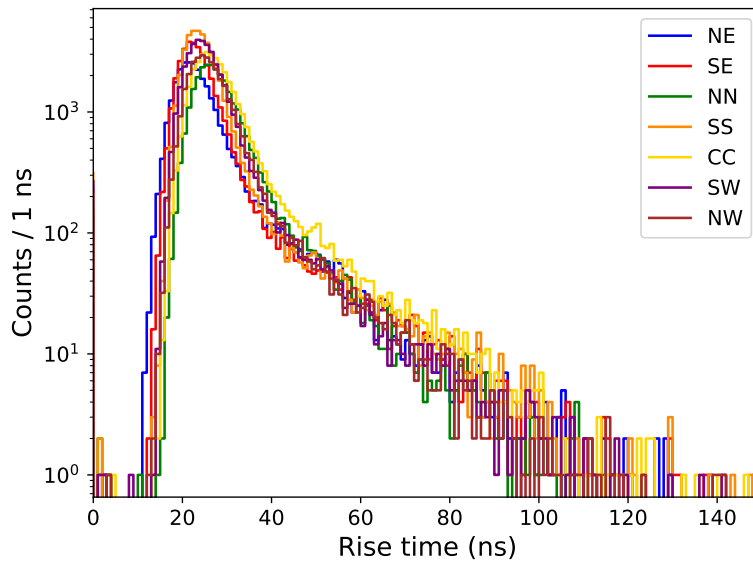


Figure 6.13: Rise time distributions of the 7-pixel detector for a measurement with K_α of an ^{55}Fe source. The mode of the distribution is at 28 ns.

6.5. Analysis Procedure

In this chapter, the measurement data will be analyzed. All data have been recorded using the first amplifier stage, see section 4.4. The following will discuss the analysis procedure to determine the charge collection efficiency at different IGR voltages. Fig. 6.14 shows an example of a measured waveform. The small steps visible on

the linearly increasing ramps correspond to signal events from the pulsed LED. The step drops correspond to reset events of the detector, see section 4.4.

In the analysis process, the first step was to isolate the pulser events. An example of a waveform snippet is shown in fig. 6.15a. In the next steps, the events have been corrected for their offset, i.e. a baseline correction was performed. Afterward, a trapezoidal filter (rise time of $0.4\ \mu\text{s}$, flat top time of $0.3\ \mu\text{s}$) was applied to the signals to extract the energy, see figure. 6.15b. Finally, the calculated energies at a given detector position have been averaged.

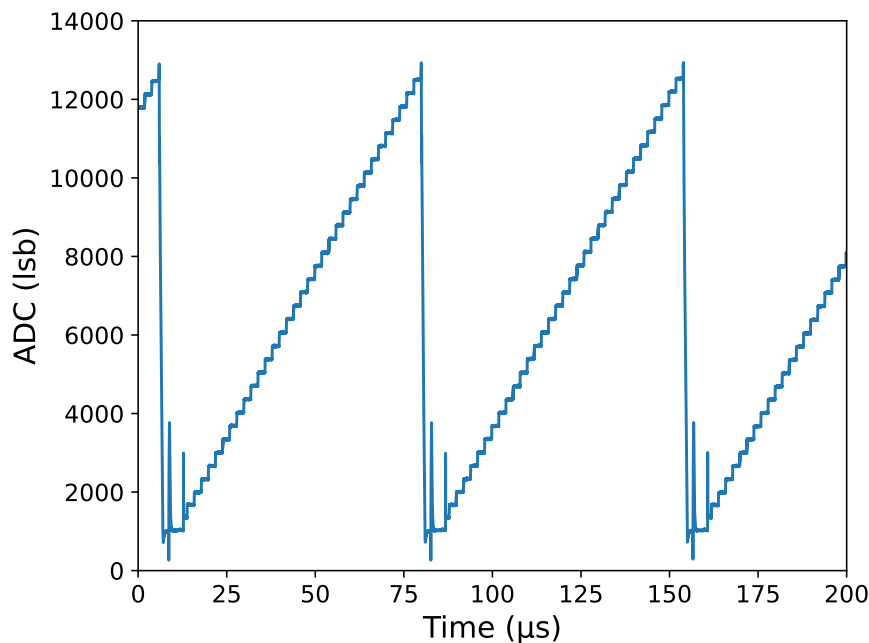


Figure 6.14: Waveform example showing the output of the first amplifier stage in the IGR voltage optimization measurements. While the small steps correspond to LED events, the steep steps can be related to reset events.

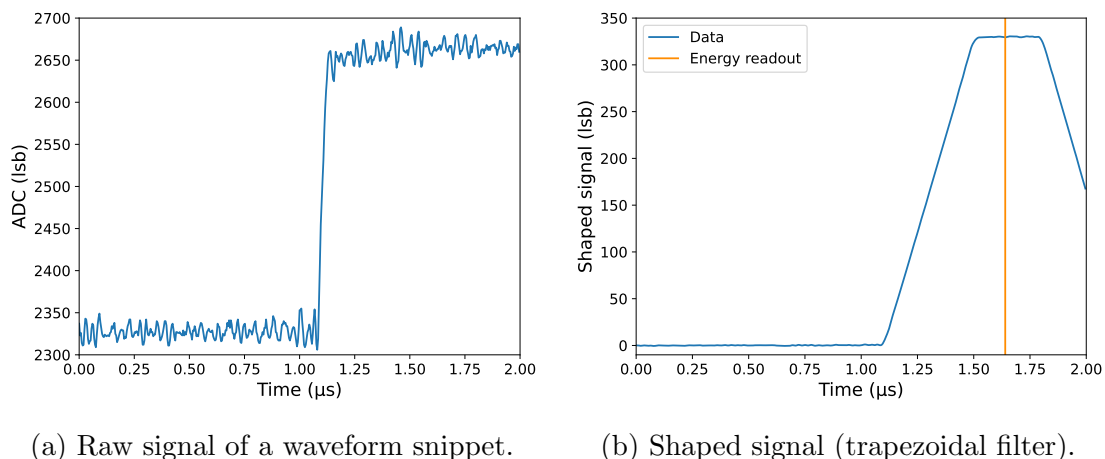


Figure 6.15: (a) Example of a waveform snippet corresponding to an LED event. The fast rise of the signal indicates the LED event. (b) Shaped waveform using a trapezoidal energy filter. The event energy is estimated in the region of the flat top.

6.6. Results of the IGR Scans

The procedure described in section 6.5 was performed for the measurement data taken at every position. The average reconstructed energy at every scan position can then be illustrated in a two-dimensional heat map. An example of such a map at the IGR voltage of $\text{IGR} = -16\text{ V}$ is shown in fig. 6.16a for the example of the forward scan. It can be observed that in the center, the reconstructed energy is smaller than at higher radial positions. This can be explained by an energy loss at the pixel center, i.e. charge carriers drifting to the nJFET instead of the readout anode. Also, small instabilities of the output power of the LED are visible. As discussed above, for a given IGR voltage, two scan measurements have been performed (differing in the scanning direction). This was done to reduce instabilities related to the output power of the LED. As a first step, the energy was reconstructed independently for the two measurements. Thereupon, at a given scanning position, the average of the two measurements was calculated. This result is shown in fig. 6.16b.

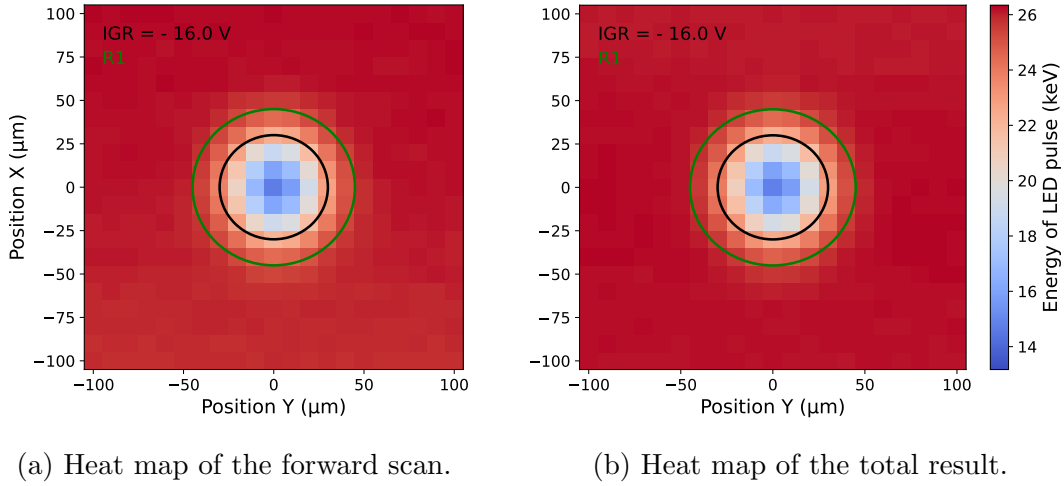


Figure 6.16: Heat maps showing the reconstructed LED pulse energy at the different scanning positions. The maps show the average results of two independent measurements (differing in the scanning direction): (a) forward scan and (b) total result. The measurement was performed at an IGR voltage of $\text{IGR} = -16 \text{ V}$. The figure also shows the position of the IGR (black circle) and of R1 (green circle)

To investigate the impact of the IGR voltage on the reconstructed energy, the entire analysis was repeated for the measurements at the different IGR voltages in the range from -16 V to -25 V . For reasons of comparability, all results were normalized due to slightly different maximum energy for the different voltages. For data normalization, only the outermost scanning points were used. More specifically, only scanning positions with a distance of more than $70 \mu\text{m}$ to the pixel center were used for the normalization. At this distance, the impact of the IGR is negligible and does not affect the normalization. This allows the charge loss to be quantified in percent, which makes a comparison feasible. The result of some selected IGR voltages is shown in fig. 6.17. The heat maps for all IGR voltage scans can be found in appendix A. For the most positive IGR voltage of -15 V , the charge loss at the pixel center is up to about 50%. With decreasing IGR voltage, a higher fraction of the charge is collected, i.e. the charge loss decreases. At IGR voltages below -22 V , no charge loss can be observed any longer. For illustration purposes, the charge loss in the pixel center (scanning position $X = 0 \mu\text{m}$, $Y = 0 \mu\text{m}$) was plotted as a function of the IGR voltage, see fig. 6.18a. The plot shows that for IGR voltages below -22.0 V all charges are collected.

Another approach to quantifying the charge loss is the extraction of the reconstructed energy along a fixed Y-position of $Y = 0 \mu\text{m}$ (cut through the center of the pixel), see fig. 6.19. The plot shows how the collected charge depends on the IGR voltage. For voltages of $\text{IGR} < 22 \text{ V}$, all charges are collected at the anode, i.e. no charges are lost at the nJFET. The measurement results show that it is indispensable to set the IGR voltage properly. The results obtained in the scope of this thesis are

vital for a better understanding of the detector response. More specifically, setting the correct IGR voltage is imperative to mitigate a charge loss in the central region of the pixel.

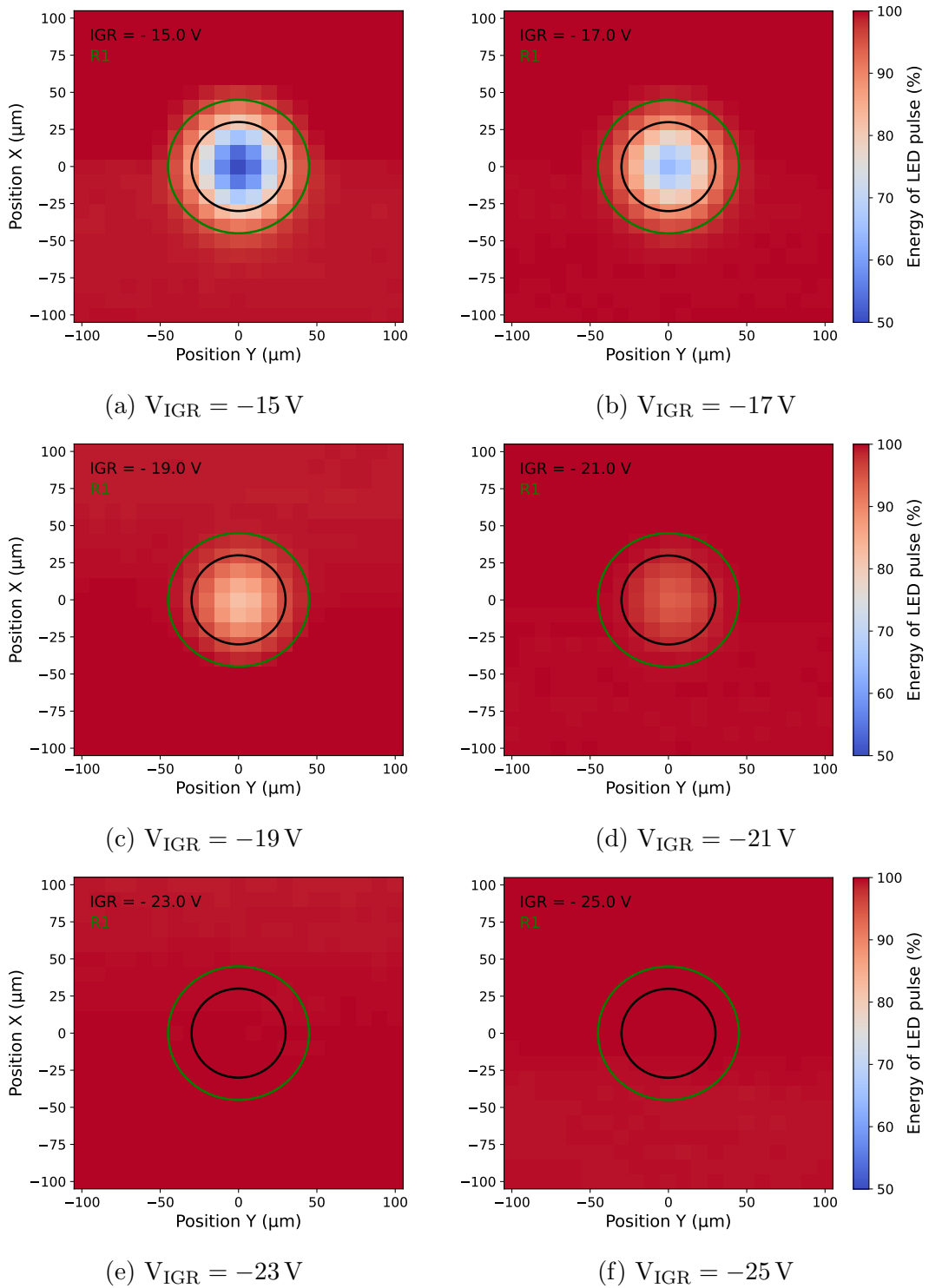


Figure 6.17: Heat maps showing the reconstructed energy at the different scanning positions for different **IGR** voltages. The plot shows the average energy of all events and two measurements at a given position. The lower the **IGR** voltage the lower the energy loss. From 23 V there is so charge loss.

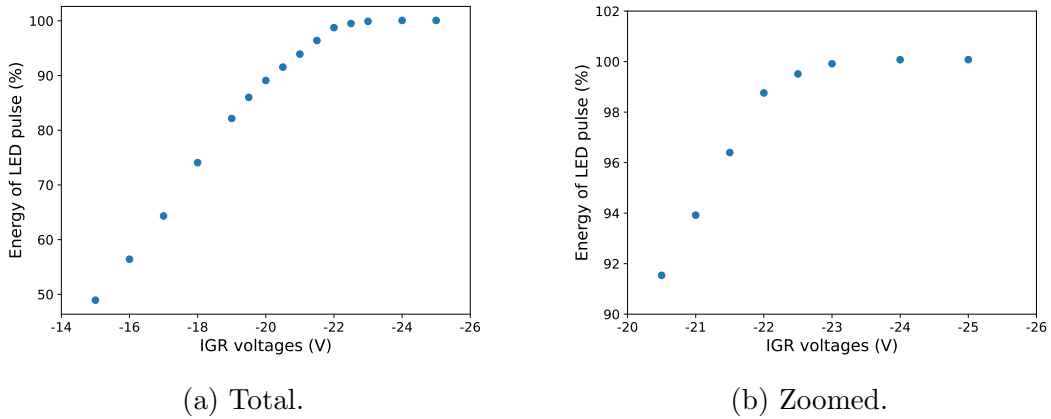


Figure 6.18: Reconstructed average energy in the center of the pixel (position $X = 0 \mu\text{m}$, $Y = 0 \mu\text{m}$) as a function of the IGR voltage for (a) every IGR voltage and (b) zoomed between 90 % 100 %. For an IGR voltage of $\text{IGR} = -15 \text{ V}$, 50 % of all charges are lost. The charge loss decreases approximately linearly for more negative IGR voltages. For IGR voltages of $\text{IGR} \leq -22 \text{ V}$, all charges are collected, i.e. no charge loss is observed.

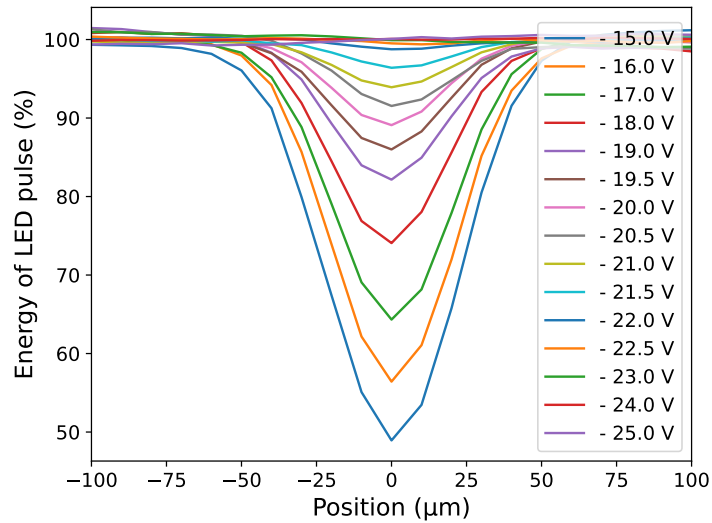


Figure 6.19: Reconstructed energy along a fixed Y-position of $Y = 0 \mu\text{m}$ (cut through the center of the pixel). The plot shows how the collected charge depends on the IGR voltage. For voltages of $\text{IGR} < -22 \text{ V}$, all charges are collected at the anode, i.e. no charges are lost at the nJFET.

7. Conclusions

Sterile neutrinos are a natural extension of the [Standard Model \(SM\)](#) of particle physics. If their mass is in the keV range, they are a suitable dark matter candidate. The Karlsruhe Tritium Neutrino (KATRIN) experiment currently measures the effective electron antineutrino mass by investigating the endpoint region of tritium β -decay. After the neutrino mass measurements have been completed at the end of 2025, the KATRIN beamline will be upgraded to enable a search for sterile neutrinos in the keV mass range. This includes the development of a novel detector and readout system within the so-called TRISTAN project [1, 41]. The main goal of this thesis was the calibration and characterization of a 7-pixel TRISTAN detector with a [Light-Emitting Diode \(LED\)](#). As a first step, the feasibility of calibrating a [Silicon Drift Detector \(SDD\)](#) with an LED has been investigated. The second main goal was the optimization of one of the detector operating voltages, i.e. the [Inner Guard Ring \(IGR\)](#) voltage. The IGR is a small electrode in the center of the pixel that prevents the charges from drifting to the integrated [n-channel Junction Field Effect Transistor \(nJFET\)](#). More specifically, the impact of the voltage on the charge collection efficiency was studied by performing a dedicated scan of the central region of a detector pixel with a pulsed LED.

Calibration with an LED

For the calibration of a 7-pixel TRISTAN prototype detector with an LED, the first step was the selection of a suitable device. After a thorough study, an LED with a high intensity and fast signal rise time was chosen. These properties are required to produce short pulses with sufficient energy. Subsequently, detector properties such as the energy resolution, rise time, and electronic noise were examined. It could be demonstrated that the rise time of LED events is much longer compared to those of conventional calibration sources such as ^{55}Fe . This is due to the fact that the LED irradiates the entire pixel. Charges produced at the outer pixel edges have a much longer drift toward the readout anode in the center of the pixel. Moreover, a relation between the energy resolution and the intensity of the LED, i.e. the peak position was found. By fitting the observed LED peak width at different energy positions to the theoretical model of energy resolution, an accuracy of about 5% from the fits and data can be achieved. To achieve a similar calibration performance as with conventional radioactive calibration sources, detailed investigations about the stability of the LED, noise, and other detector effects are required. These factors have a significant impact on the energy resolution and calibration accuracy. Despite this, LEDs offers promising advantages due to their straightforward implementation and individual control. This calibration method could also present a promising alternative for other experiments, such as IAXO, which searches for axions or axion-like particles

produced by the sun. In experiments like IAXO, where reaching very low background levels is crucial, calibrating with a radioactive source is not feasible. Using an LED, which can switch on or off, could be a viable solution for such experiments.

IGR voltage optimization scans

For the IGR voltage investigations, a dedicated measurement setup was developed. The setup consists of a pulsed LED (the same one as used for the calibration measurements) whose beam is focused on the entrance window of a 7-pixel prototype TRISTAN detector. An X-Y-Z stage can be used to scan across the detector surface. In the first step, the optimal size of the LED beam spot was determined by investigating the beam properties with the Charge-Coupled Device (CCD) chip of a webcam. Subsequently, a surface scan of the central region of one detector pixel was performed. At each scanning point, waveform data was acquired at varying IGR voltages. In offline processing, the pulse height of each signal was determined. It could be shown that if the IGR voltage is too positive, charges are lost to the integrated nJFET. At an IGR voltage of -15 V, a charge loss of about 50% was observed. For more negative IGR voltages, the charge collection efficiency gradually increases. For IGR voltages below -22 V, all charges are collected at the readout anode, i.e. no charges are lost at the nJFET. Even if the affected area is rather small compared to the area of the entire pixel, optimizing the operating voltages to achieve the best detector performance is crucial. This measurement shows for the first time the functionality of the IGR electrode and confirms the concept of this design. A new setpoint for the IGR voltage was determined that will be used for all future measurements with the TRISTAN detector.

A. Appendix

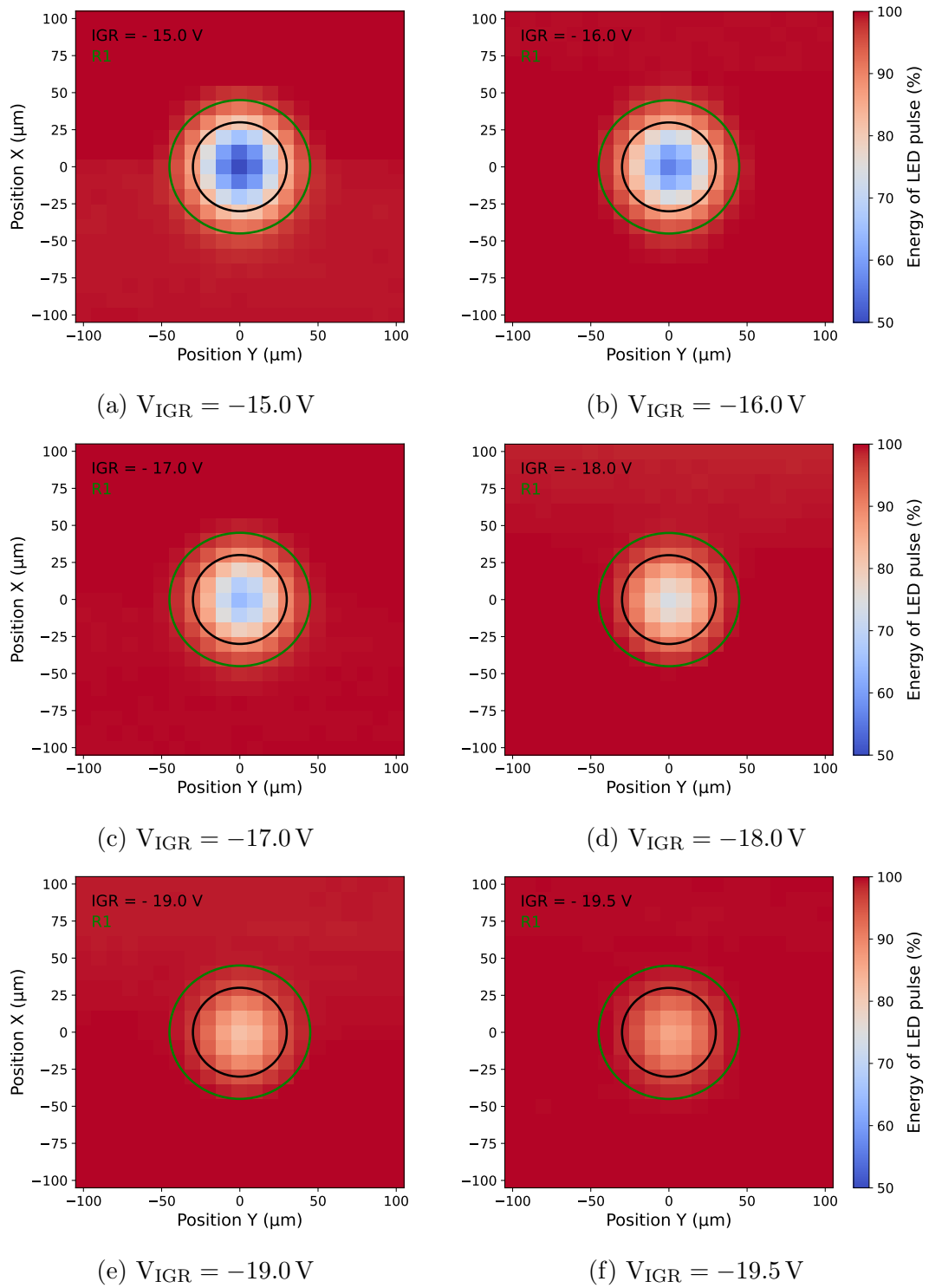


Figure A.1: Heat maps showing the reconstructed energy at the different scanning positions for different IGR voltages.

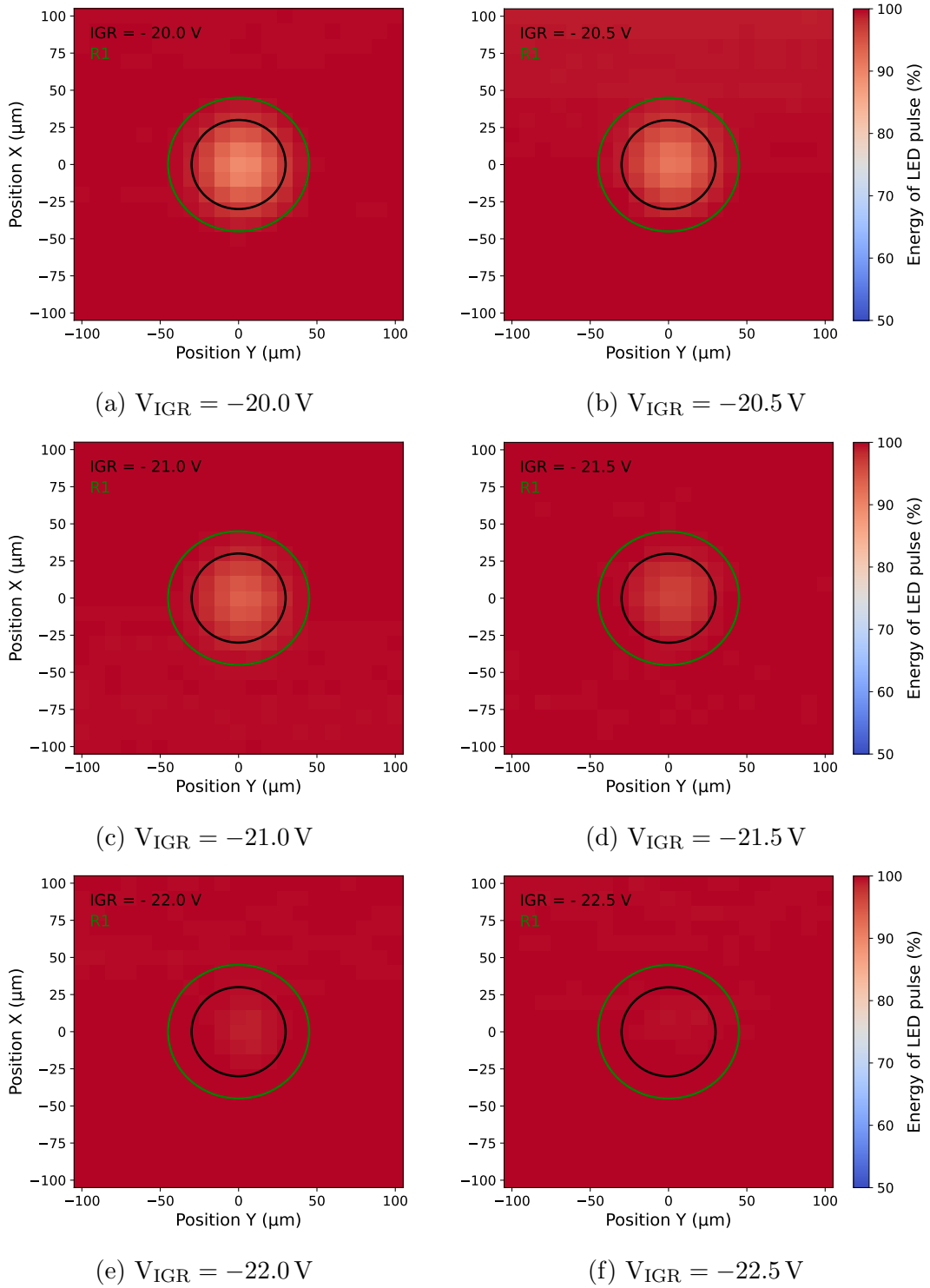


Figure A.2: Heat maps showing the reconstructed energy at the different scanning positions for different IGR voltages.

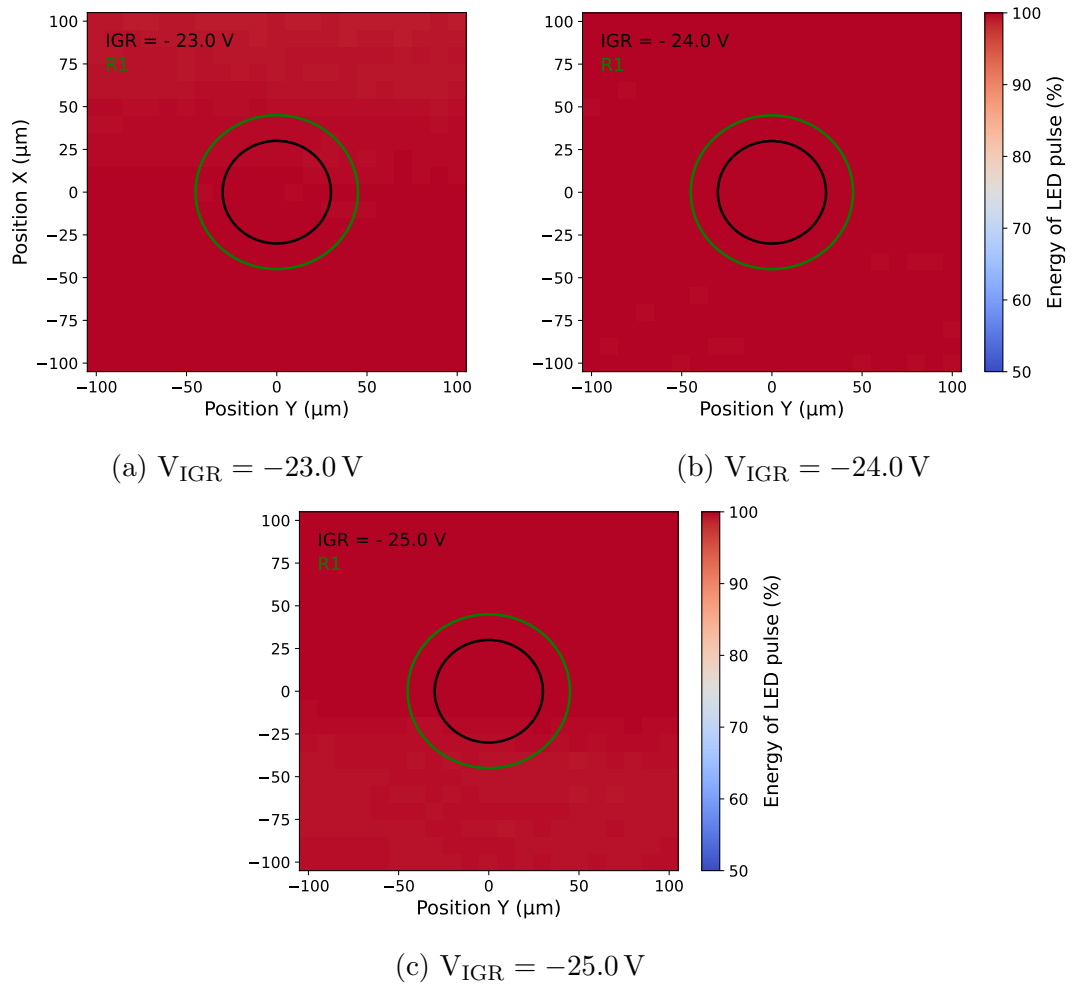


Figure A.3: Heat maps showing the reconstructed energy at the different scanning positions for different IGR voltages.

List of Figures

2.1	Standard model of particle physics	5
2.2	Masses of all fermions	7
2.3	Tritium spectrum	8
3.1	KATRIN beamline	11
3.2	MAC-E filter principle	13
3.3	Focal Plane Detector	14
3.4	Sterile Neutrino Imprint on β -spectrum	16
3.5	166-pixel detector module	18
3.6	TRISTAN Detector Design	18
4.1	Bandstructure of metals, semiconductor and insulators	20
4.2	Illustration of band structure for doped semiconductors	20
4.3	Illustration of reverse-bias pn-junction	22
4.4	Illustration of sideways depletion	23
4.5	Scheme of an SDD with integrated nJFET for the TRISTAN project	24
4.6	Simulation of the electrical potential of an SDD	24
4.7	Illustration of the charge collection efficiency function	26
4.8	Illustration of the nomenclature of a 7-pixel detector	27
4.9	Technical drawings of the PCB	29
4.10	Technical drawings of the detector bias system	29
4.11	DAQ system CAEN DT5725	30
4.12	Simplified sketch of the detector readout scheme for one pixel	31
4.13	Waveform of first and second amplifier stage	32
4.14	Examples for the event energy reconstruction	32
5.1	Photograph of the LED carrier board	34
5.2	Circuit diagram of the LED carrier board	34
5.3	Photograph of the LED placed below the entrance window of 7-pixel TRISTAN detector	35
5.4	Photograph of the dark box with 7-pixel detector and LED	35
5.5	Photograph of the total LED calibration setup	36
5.6	Comparison of all LEDs	41
5.7	Uncalibrated spectrum for the NE pixel	42
5.8	Production mechanism of e-h pairs with an X-ray and an LED	43
5.9	^{55}Fe spectrum with fits for calibration	44
5.10	Calibrated spectra for all seven pixels	45
5.11	Spectrum of the trigger signal	46
5.12	Limit for counting the LED events	47
5.13	Number of LED events divided through pulser events	47
5.14	Energy scan for the NN pixel	49

5.15	Energy resolutions of the K_{α} and LED peak	49
5.16	Energy resolution for different high-level voltages	50
5.17	Energy resolution of the LED peak at 5.9 keV	50
5.18	All fit combinations for comparison with Poissonian nature	52
5.19	Raw and PZ-corrected waveform	54
5.20	Noise curve for ^{55}Fe and LED events for every pixel	54
5.21	Noise curve for ^{55}Fe and LED	55
5.22	Superpulse of ^{55}Fe and LED events	56
5.23	Pixel maps of the rise times of the ^{55}Fe K_{α} and LED of superpulses	57
5.24	2D histogram of a long term measurement	58
5.25	Long term measurement divided into time steps	58
6.1	Photograph of the IGR setup in the dark box	61
6.2	Scheme of the IGR setup	61
6.3	Photograph of the entire IGR setup	62
6.4	Photograph of the ^{55}Fe on top of the detector	62
6.5	Photograph of the fiber, fixed on the X-Y-Z stage to shoot on a webcam	63
6.6	Example of one recorded picture with the webcam	64
6.7	Fit to get the width of the beam spot	65
6.8	Result of the scan with the webcam	65
6.9	Grid for the IGR measurements	67
6.10	Calibrated spectrum of ^{55}Fe	68
6.11	Pixel map of the energy resolution of the K_{α} peak in FWHM	68
6.12	Noise curve of the resolution of the ^{55}Fe K_{α} peak	69
6.13	Histogram of the rise time of ^{55}Fe	69
6.14	Raw waveform of one IGR measurement	70
6.15	Example of a waveform snipped of the IGR measurement and applied trapezoid filter	71
6.16	2D map of the backwards and total result for anIGR voltage of 16.0 V	72
6.17	Heat maps of the result of the IGR measurement	74
6.18	The charge loss for every IGR voltage	75
6.19	Charge loss for the central line of the 2D plot	75
A.1	Heat maps of the result of the IGR measurement	79
A.2	Heat maps of the result of the IGR measurement	80
A.3	Heat maps of the result of the IGR measurement	81

List of Tables

1	Values for the operating voltages at the bias board were taken. Before every measurement, these values were set.	37
2	Overview over all measurement parameter in campaign 1 for measuring pulsed events from the LED.	38
3	Overview over all measurement parameter in campaign 2 for measuring pulsed events from the LED.	39
4	Overview of the most important DAQ parameters.	39
5	Overview over all LEDs. 650 nm corresponds to an energy of 1.9 eV. "Op." stands for "operating".	40
6	Pulse generator settings of the LED beam for the IGR voltage optimization measurements.	66

Acronyms

ADC	Analog-to-Digital Converter
ASIC	Application-Specific Integrated Circuit
BBN	Big Bang Nucleosynthesis
BC	Back Contact
BF	Back Frame
BIXS	Beta-Induced X-ray Spectroscopy
CCD	Charge-Coupled Device
CDM	Cold Dark Matter
CPS	Cryogenic Pumping Section
CSA	Charge Sensitive Amplifier
DAQ	Data Acquisition
DM	Dark Matter
DPP	Digital Pulse Processor
DPS	Differential Pumping Section
e-gun	electron gun
e-h pair	electron-hole pair
FPD	Focal Plane Detector
FPGA	Field-Programmable Gate Array
FWHM	Full Width Half Maximum
IGR	Inner Guard Ring
LED	Light-Emitting Diode
MOS	Monitor Spectrometer
nJFET	n-channel Junction Field Effect Transistor
PCB	Printed Circuit Board
PHA	Pulse Height Analysis
PIN	Positive Intrinsic Negative
PMNS	Pontecorvo-Maki-Nakagawa-Sakata
PSD	Pulse Shape Discrimination
R1	Ring 1
RX	Ring X
SDD	Silicon Drift Detector
SM	Standard Model
TMPs	Turbo Molecular Pumps
WDM	Warm Dark Matter
WGTS	Windowless Gaseous Tritium Source

References

- [1] S. Mertens et al. “A novel detector system for KATRIN to search for keV-scale sterile neutrinos”. In: *J. Phys. G: Nucl. Part. Phys.* 46.065203 (May 2019). DOI: [10.1088/1361-6471/ab12fe](https://doi.org/10.1088/1361-6471/ab12fe).
- [2] R. Mann. *An introduction to particle physics and the standard model*. CRC Press, 2007. ISBN: 9780429141225. DOI: [10.1201/9781420083002](https://doi.org/10.1201/9781420083002).
- [3] N. Barros et al. “Final results from SNO”. In: *Nuclear Physics B - Proceedings Supplements* 237-238 (May 2013). DOI: [10.1016/j.nuclphysbps.2013.04.069](https://doi.org/10.1016/j.nuclphysbps.2013.04.069).
- [4] Y. Fukuda et al. “Evidence for Oscillation of Atmospheric Neutrinos”. In: *Phys. Rev. Lett* 81 (Aug. 1998). DOI: [10.1103/PhysRevLett.81.1562](https://doi.org/10.1103/PhysRevLett.81.1562).
- [5] W. Pauli. *Pauli letter collection: letter to Lise Meitner*. <https://cds.cern.ch/record/83282>. Dec. 1930.
- [6] C.L. Cowan Jr. et al. “Detection of the Free Neutrino: a Confirmation”. In: *Science* 124.3212 (July 1956), pp. 103–104. DOI: [10.1126/science.124.3212.103](https://doi.org/10.1126/science.124.3212.103).
- [7] G. Danby et al. “Observation of High-Energy Neutrino Reactions and the Existence of Two Kinds of Neutrinos”. In: *Phys. Rev. Lett.* 9.36 (July 1962). DOI: [10.1103/PhysRevLett.9.36](https://doi.org/10.1103/PhysRevLett.9.36).
- [8] *Verein zur Förderung des physikalischen und chemischen Unterrichts*. URL: <https://pluslucis.org/Zeitschrift.html>.
- [9] DONUT Collaboration; K. Kodama et al. “Observation of tau neutrino interactions”. In: *Phys. Lett. B* 504 (Apr. 2001). DOI: [10.1016/S0370-2693\(01\)00307-0](https://doi.org/10.1016/S0370-2693(01)00307-0).
- [10] M. Goldhaber; L. Grodzins and A. W. Sunyar. “Helicity of Neutrinos”. In: *Phys. Rev.* 109.1015 (Feb. 1958). DOI: [10.1103/PhysRev.109.1015](https://doi.org/10.1103/PhysRev.109.1015).
- [11] S.N. Gninenko; D.S. Gorbunov and M.E. Shaposhnikov. “Search for GeV-Scale Sterile Neutrinos Responsible for Active Neutrino Oscillations and Baryon Asymmetry of the Universe”. In: *Advances in High Energy Physics* 2012.718259 (Dec. 2012). DOI: [10.1155/2012/718259](https://doi.org/10.1155/2012/718259).
- [12] B.T. Cleveland et al. “Measurement of the Solar Electron Neutrino Flux with the Homestake Chlorine Detector”. In: *The Astrophysical Journal* 496.1 (Apr. 1998). DOI: [10.1086/305343](https://doi.org/10.1086/305343).
- [13] M. Zito C. Giganti S. Lavignac. “Neutrino oscillations: The rise of the PMNS paradigm”. In: *Progress in Particle and Nuclear Physics* 98 (Oct. 2017). DOI: [10.1016/j.pnpnp.2017.10.001](https://doi.org/10.1016/j.pnpnp.2017.10.001).

- [14] J.K. Ahn et al. (RENO Collaboration). “Observation of Reactor Electron Antineutrinos Disappearance in the RENO Experiment”. In: *Phys. Rev. Lett.* 108.191802 (May 2012). DOI: [10.1103/PhysRevLett.108.191802](https://doi.org/10.1103/PhysRevLett.108.191802).
- [15] F.P. An et al. “Observation of Electron-Antineutrino Disappearance at Daya Bay”. In: *Phys. Rev. Lett.* 108.171803 (Apr. 2012). DOI: [10.1103/PhysRevLett.108.171803](https://doi.org/10.1103/PhysRevLett.108.171803).
- [16] K. Abe et al. (T2K Collaboration). “Observation of Electron Neutrino Appearance in a Muon Neutrino Beam”. In: *Phys. Rev. Lett.* 112.061802 (Feb. 2014). DOI: [10.1103/PhysRevLett.112.061802](https://doi.org/10.1103/PhysRevLett.112.061802).
- [17] F.A. Edzards. “Characterization of Point Contact Germanium Detectors and Development of Signal Readout Electronics for LEGEND”. PhD Thesis. Technical University of Munich, 2021. URL: <https://mediatum.ub.tum.de/?id=1609363>.
- [18] *An den Grenzen des technisch Machbaren*. URL: <https://www.weltderphysik.de/gebiet/teilchen/nachrichten/2018/an-den-grenzen-des-technisch-machbaren>.
- [19] N. Aghanim et al. (Planck Collaboration). “Planck 2018 results. VI. Cosmological parameters”. In: *Astronomy and Astrophysics* 641 (July 2018). DOI: [10.48550/arXiv.1807.06209](https://doi.org/10.48550/arXiv.1807.06209).
- [20] C. Wiesinger. “No neutrinos not found”. PhD Thesis. Technical University of Munich, 2021. URL: <https://mediatum.ub.tum.de/node?id=1575899>.
- [21] S. Abe et al. (KamLAND-Zen Collaboration). “Search for the Majorana Nature of Neutrinos in the Inverted Mass Ordering Region with KamLAND-Zen”. In: *High Energy Physics - Experiment* (Mar. 2022). DOI: [10.48550/arXiv.2203.02139](https://doi.org/10.48550/arXiv.2203.02139).
- [22] D. Siegmann. “Investigation of the Detector Response to Electrons of the TRISTAN Prototype Detectors”. Master’s Thesis. Technical University of Munich, 2019.
- [23] The KATRIN Collaboration. “Improved Upper Limit on the Neutrino Mass from a Direct Kinematic Method by KATRIN”. In: *Phys. Rev. Lett.* 123 (Nov. 2019). DOI: [10.1103/PhysRevLett.123.221802](https://doi.org/10.1103/PhysRevLett.123.221802).
- [24] The KATRIN Collaboration. “Analysis methods for the first KATRIN neutrino-mass measurement”. In: *Phys. Rev. D* 104 (July 2021). DOI: [10.1103/PhysRevD.104.012005](https://doi.org/10.1103/PhysRevD.104.012005).
- [25] The KATRIN Collaboration. “Direct neutrino-mass measurement with sub-electronvolt sensitivity”. In: *Nature Physics* 18 (Feb. 2022), pp. 160–166. DOI: [10.1038/s41567-021-01463-1](https://doi.org/10.1038/s41567-021-01463-1).

- [26] R.N. Mohapatra and G. Senjanović. “Neutrino Mass and Spontaneous Parity Nonconservation”. In: *Phys. Rev. Lett.* 44.912 (Apr. 1980). DOI: [10.1103/PhysRevLett.44.912](https://doi.org/10.1103/PhysRevLett.44.912).
- [27] V. Domcke et al. “MeV-scale Seesaw and Leptogenesis”. In: *High Energy Physics* (Apr. 2021). DOI: [10.48550/arXiv.2009.11678](https://doi.org/10.48550/arXiv.2009.11678).
- [28] J.P. Conlon et al. “Consistency of Hitomi, XMM-Newton and Chandra 3.5 keV data from Perseus”. In: *Phys. Rev. D* 96 (123009 Dec. 2017). DOI: [10.1103/PhysRevD.96.123009](https://doi.org/10.1103/PhysRevD.96.123009).
- [29] M. Cribier et al. “Results of the whole GALLEX experiment”. In: *Nuclear Physics B - Proceedings Supplements* 70 (Jan. 1999). DOI: [10.1016/S0920-5632\(98\)00438-1](https://doi.org/10.1016/S0920-5632(98)00438-1).
- [30] J. N. Abdurashitov et al. “The Russian-American Gallium Experiment (SAGE) Cr Neutrino Source Measurement”. In: *Phys. Rev. Lett.* 77 (Dec. 1996). DOI: [10.1103/PhysRevLett.77.4708](https://doi.org/10.1103/PhysRevLett.77.4708).
- [31] Vladislav Barinov and Dmitry Gorbuno. “BEST impact on sterile neutrino hypothesis”. In: *Phys. Rev. D* 105 (Mar. 2022). DOI: [10.1103/PhysRevD.105.L051703](https://doi.org/10.1103/PhysRevD.105.L051703).
- [32] M. Aker et al. “Improved eV-scale sterile-neutrino constraints from the second KATRIN measurement campaign”. In: *Physical Review D* 105.7 (Apr. 2022). DOI: [10.1103/physrevd.105.072004](https://doi.org/10.1103/physrevd.105.072004).
- [33] M. Aker et al. “First operation of the KATRIN experiment with tritium”. In: *The European Physical Journal C* 80.264 (Mar. 2020). DOI: [10.1140/epjc/s10052-020-7718-z](https://doi.org/10.1140/epjc/s10052-020-7718-z).
- [34] M. Aker et al. “First direct neutrino-mass measurement with sub-eV sensitivity”. In: *High Energy Physics - Experiment* (May 2021). DOI: [10.48550/arXiv.2105.08533](https://doi.org/10.48550/arXiv.2105.08533).
- [35] KATRIN Collaboration. *Katrin design report 2004*. Technical report. Forschungszentrum Karlsruhe, Feb. 2005. DOI: [10.5445/ir/270060419](https://doi.org/10.5445/ir/270060419).
- [36] K. Hugenberg. “Design of the electrode system of the KATRIN main spectrometer”. Diploma Thesis. WWU Münster, 2008. URL: https://www.uni-muenster.de/Physik.KP/AGWeinheimer/theses/Diplom_%20Karen_Hugenberg.pdf.
- [37] L. Schlüter. “Development of New Methods to Include Systematic Effects in the First Tritium Data Analysis and Sensitivity Studies of the KATRIN Experiment”. Master’s Thesis. TUM, 2019. URL: https://www.ph.nat.tum.de/fileadmin/w00bya/neutrinos/Thesis/Master/KATRIN_Schlueter_Lisa_19.pdf.

- [38] R. Adhikari et al. “A White Paper on keV sterile neutrino Dark Matter”. In: *Journal of Cosmology and Astroparticle Physics* (Jan. 2017), pp. 025–025. DOI: [10.1088/1475-7516/2017/01/025](https://doi.org/10.1088/1475-7516/2017/01/025).
- [39] T.B. Brunst. “First generation prototype detectors for the TRISTAN project”. PhD Thesis. Technical University of Munich, 2020. URL: <https://mediatum.ub.tum.de/?id=1540377>.
- [40] M. Aker et al. (KATRIN collaboration). “Search for keV-scale Sterile Neutrinos with first KATRIN Data”. In: *Nuclear Experiment* (July 2022). DOI: [10.48550/arXiv.2207.06337](https://doi.org/10.48550/arXiv.2207.06337).
- [41] TRISTAN group. *Conceptual Design Report: KATRIN with TRISTAN modules*. URL: [https://www.katrin.kit.edu/downloads/TRISTAN__Technical_Design_Report%20\(10\).pdf](https://www.katrin.kit.edu/downloads/TRISTAN__Technical_Design_Report%20(10).pdf).
- [42] M. Gugiatti. “Development of a Large-matrix SDD-based Radiation Detector for Beta-decay Spectroscopy in Neutrino Physics”. PhD Thesis. Politecnico Milano, 2022.
- [43] K. Dolde. “Detector and read-out development to search for sterile neutrinos with KATRIN”. Master’s Thesis. Karlsruhe Institute of Technology, 2016.
- [44] J. Kholdkov. “Measurement of ADC Nonlinearities and Development of a Bias Board for the TRISTAN Detector”. Master’s Thesis. Technical University of Munich, 2021.
- [45] D. Siegmann et al. “Development of a Silicon Drift Detector Array to Search for keV-scale Sterile Neutrinos with the KATRIN Experiment”. 2024. arXiv: [2401.14114](https://arxiv.org/abs/2401.14114) [[physics.ins-det](https://arxiv.org/abs/2401.14114)].
- [46] G. Lutz. *Semiconductor Radiation Detectors*. Springer Berlin, 2007. ISBN: 9783540716785.
- [47] F. Hartmann. *Evolution of Silicon Sensor Technology in Particle Physics*. Springer International Publishing AG, 2017. ISBN: 9783319877945.
- [48] Brigit Kanngießer Norbert Langhoff et al. Burkhard Beckhof. *Particle X-Ray Fluorescence Analysis*. Springer Science+Business Media, 2006.
- [49] P. Lechner et al. “Silicon drift detectors for high count rate X-ray spectroscopy at room temperature”. In: *Nuclear Instruments and Methods in Physics Research Section A: Accelerators, Spectrometers, Detectors and Associated Equipment* 458 (Feb. 2001). DOI: [10.1016/S0168-9002\(00\)00872-X](https://doi.org/10.1016/S0168-9002(00)00872-X).
- [50] Oxford Instruments. The Business of Science., ed. *Silicon Drift Detectors Explained*. 2012. URL: https://www.exvil.lt/wp-content/uploads/2012/04/SDD_Explained.pdf.

- [51] G. F. Knoll. *Radiation Detection and Measurement*. Wiley, 2010. ISBN: 978-0-470-13148-0. URL: <https://www.wiley.com/en-us/Radiation+Detection+and+Measurement%2C+4th+Edition-p-9780470131480>.
- [52] C. Forstner. “Characterization of a TRISTAN Silicon Drift Detector Array with a Laser System”. Master’s Thesis. Technical University of Munich, 2023. URL: https://www.ph.nat.tum.de/fileadmin/w00bya/neutrinos/Thesis/Master/TRISTAN_Forstner_Christian_23.pdf.
- [53] R. C. Alig et al. “Scattering by ionization and phonon emission in semiconductors”. In: *Phys. Rev. B* 72 (Dec. 1980). DOI: [10.1103/PhysRevB.22.5565](https://doi.org/10.1103/PhysRevB.22.5565).
- [54] P. Lechner and L. Strüder. “Ionization statistics in silicon X-ray detectors — new experimental results”. In: *Nuclear Instruments and Methods in Physics Research Section A: Accelerators, Spectrometers, Detectors and Associated Equipment* 354 (Jan. 1995). DOI: [10.1016/0168-9002\(94\)01317-9](https://doi.org/10.1016/0168-9002(94)01317-9).
- [55] E. Pinotti et al. “The pn-CCD on-chip electronics”. In: *Nuclear Instruments and Methods in Physics Research Section A: Accelerators, Spectrometers, Detectors and Associated Equipment* 326 (Mar. 1993). DOI: [10.1016/0168-9002\(93\)90337-H](https://doi.org/10.1016/0168-9002(93)90337-H).
- [56] R. Müller. *Halbleiter-Elektronik: Rauschen. Halbleiter-Elektronik*. Springer Verlag Berlin Heidelberg GmbH, 1979. ISBN: 9783642615016.
- [57] H. Spieler. *Semiconductor Detector Systems. Semiconductor Science and Technology*. Clarendon Press Oxford, 2005. ISBN: 9780198527848.
- [58] P. Lechner. “Zur Ionisationsstatistik in Silicium”. PhD Thesis. Technical University of Munich, 1998.
- [59] M. Popp. “Untersuchung und analytische Modellierung der Systemantwort von pn-CCD Detektoren”. PhD Thesis. Ludwig-Maximilians-Universität München, 2000.
- [60] D. Greenwald. “Characterization of the proton source in the frictional cooling demonstration experiment”. Master’s thesis. Technical University of Munich, 2007.
- [61] F. Edzards et al. “Understanding and Characterization of Silicon Drift Detectors for Applications in Astroparticle Physics”. In: (May 2023).
- [62] M. Gugiatti. “»Development of a large-matrix SDD-based radiation detector for beta-decay spectroscopy in neutrino physics”. PhD Thesis. Politecnico di Milano, 2021.
- [63] *CAEN Digitizer*. URL: <https://www.caen.it/sections/digitizer-families/>.

- [64] P. Trigilio et al. “ETTORE: a 12-Channel Front-End ASIC for SDDs with Integrated JFET”. In: *IEEE Xplore* (Sept. 2019). DOI: [10.1109/NSSMIC.2018.8824675](https://doi.org/10.1109/NSSMIC.2018.8824675).
- [65] *Laser Components GmbH*. URL: https://www.lasercomponents.com/fileadmin/user_upload/home/Datasheets/arima/655nm/adl-65055tl.pdf.
- [66] *Data sheet Photodiode BPX 65*. URL: <https://docs.rs-online.com/32f9/0900766b817157ba.pdf>.
- [67] *Data sheet ADL-65055TL*. URL: <https://asset.conrad.com/media10/add/160267/c1/-/en/001782887DS01/datenblatt-1782887-laser-components-laserdiode-rot-650-nm-5-mw-adl-65055tl.pdf>.
- [68] *Data sheet CSL0701DT5*. URL: <https://www.mouser.de/datasheet/2/348/csl0701x-e-1874509.pdf>.
- [69] *Data sheet NSPB300B*. URL: <https://docs.rs-online.com/a5b6/0900766b8138550d.pdf>.
- [70] *Data sheet NSPR310S-RP-S-T*. URL: <https://docs.rs-online.com/8a90/0900766b8133ed8d.pdf>.
- [71] *Data sheet WP7113LSECK/J3*. URL: https://www.mouser.de/datasheet/2/216/WP7113LSECK_J3-535726.pdf.
- [72] *SM05PT Adapter*. URL: <https://www.thorlabs.com/thorproduct.cfm?partnumber=SM05PT>.

Acknowledgements

I want to thank everyone who supported me during my master's thesis, especially:

- **Prof. Dr. Susanne Mertens:** I am very grateful to Prof. Dr. Susanne Mertens for allowing me to do my master's thesis in your group, supporting my work, and being part of a great team.
- **Frank Edzards:** You are a great supervisor, always taking the time when I have questions or need help in the lab. Even if your feedback is sometimes a bit much, it was always worth it, and I learned a lot for the future. It was a lovely time with you, and I will never forget it. Thank you for everything.
- **Korbinian Urban:** I appreciate your support during my master's thesis as supervisor. Your endless knowledge and skills in the laboratory have always helped me. Still need to learn how one person can always have the answer to everything.
- **Christian Forstner:** Thanks for your help, especially for the [IGR](#) measurement. I need to catch up on certain things and have more time. I hope I used up only a little of your patience.
- **Daniel:** I enjoyed the time with you. You were always available to answer questions when no one else was there, and somehow, you created a lovely working atmosphere. Thank you.
- **Lucinda:** You always helped me when I asked. The music sessions in the lab were simply amazing. Even though your taste in music was a bit too heavy for me as a softie, we still created a great playlist. I always think of our lab time together when I listen to "The Chase."
- **Verena:** I can't imagine a better office colleague than you. You always helped me when I needed someone. Thanks for all our fun and helpful conversations, apart from the physics.
- **The E47 Team:** I would like to thank all the members of the E47 group for all the support and pleasant work environment.
- **My Family:** Thank you for giving me the possibility to be able to study in a pleasant environment.
- **Corinna:** Thank you for simply being there for me, for your words of encouragement when I needed them, and for all your support. I'm so glad I have you.